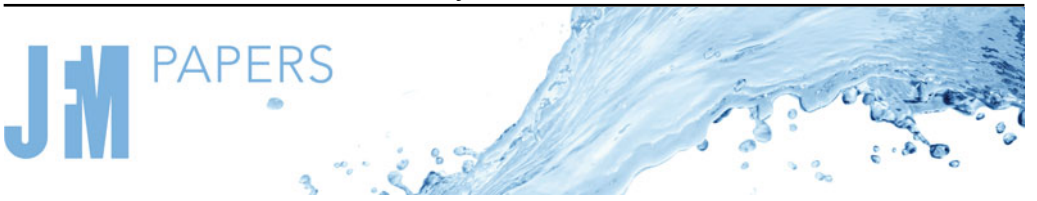
J. Fluid Mech. (2026), *vol.* 1043, A8, doi:10.1017/jfm.2026.12002



Transition in elastic Dean flow: the centre-mode versus hoop-stress pathways

P.S.D. Surya Phani Tej[1], **Ganesh Subramanian**[2] **and V. Shankar**[1]

[1]Department of Chemical Engineering, Indian Institute of Technology, Kanpur 208016, India

[2]Engineering Mechanics Unit, Jawaharlal Nehru Centre for Advanced Scientific Research, Bangalore 560064, India

Corresponding authors: V. Shankar, vshankar@iitk.ac.in; Ganesh Subramanian, sganesh@jncasr.ac.in

(Received 8 December 2025 UTC; revised 24 June 2026 UTC; accepted 5 August 2026 UTC)

We analyse the stability of viscoelastic Dean flow (flow of an elastic fluid through a curved two-dimensional channel, driven by an azimuthal pressure gradient) in the absence of fluid inertia. This configuration is well known to exhibit a hoop-stress-driven 'purely elastic' instability (referred to henceforth as the hoop-stress mode – 'HSM') on account of the base-flow streamline curvature. The objective of this study is to demonstrate the existence and importance of a distinct elastic instability in this flow configuration, which is not driven by hoop stresses, but instead is a continuation of a novel 'centre-mode' (CM) instability recently identified in rectilinear shear flows. On account of its origins, the CM instability in Dean flow is expected for two-dimensional (azimuthally varying) disturbances with no axial variation, but continues to exist for three-dimensional disturbances. In contrast, the HSM instability is expected primarily in the axisymmetric limit, and again continues to exist for three-dimensional disturbances. We use both the Oldroyd-B and FENE-P models to map out parameter regimes in the Wi–ϵ–β space where the aforementioned instabilities are present. Here, Wi is a suitably defined Weissenberg number that characterises fluid elasticity, β is the ratio of solvent to total solution viscosity and ϵ is the ratio of the gap (channel) width to the radius of curvature. While its origin in rectilinear shearing flows might lead one to expect the CM instability to only be present for small ϵ (the 'narrow-gap' limit), we show that it exists even for $O(1)$ values of ϵ, and over a larger range of Wi. Nevertheless, within the Oldroyd-B framework, the HSM determines the stability threshold for experimentally relevant gap-width ratios, corresponding to $0.1 \leqslant \epsilon \leqslant 1$, with the CM becoming the most unstable mode only for $\epsilon < 0.001$. For the more accurate FENE-P model, however, decreasing the finite extensibility parameter L has opposing effects on the HSM and CM instabilities – stabilising the former, but destabilising the latter. In the dilute solution regime ($\beta > 0.95$) and for realistic values of

https://doi.org/10.1017/jfm.2026.12002 Published online by Cambridge University Press

© The Author(s), 2026. Published by Cambridge University Press.

$L \sim O(100)$, corresponding to polymer molecular weights of $O(10^{5-6})$ g mol^{-1}, the CM remains the most unstable mode for $\epsilon \leqslant 0.25$, rendering it potentially relevant to the onset of elastic turbulence in the flow of such polymer solutions through curved channels.

Key words: viscoelasticity, shear-flow instability, rheology

1. Introduction

Viscoelastic fluids subject to a shearing flow often exhibit strikingly novel instabilities engendered by their elastic nature, which are absent in their Newtonian counterparts. For instance, it is well known, since the pioneering work of Larson *et al.* (1990), that Taylor–Couette flow of a viscoelastic fluid exhibits a linear instability even when fluid inertia is negligible. Analogous instabilities have been demonstrated for the flow of polymer solutions in other curvilinear geometries such as cone-and-plate flow (McKinley *et al.* 1991), torsional flow between parallel circular discs (Byars *et al.* 1994), and the Dean and Taylor–Dean flow configurations (Joo & Shaqfeh 1991, 1992, 1994). These instabilities, collectively referred to as 'purely elastic' instabilities (see Shaqfeh 1996), rely on two key ingredients in the base state – streamline curvature and a streamwise normal stress that has a tensile character (owing to stretched polymers). The latter results in a 'hoop stress' in the aforementioned curvilinear flows that then drives an instability even in the absence of inertial forces; the latter forces come into play even in a Newtonian fluid, leading to inertial instabilities beyond a threshold Reynolds number (Re) in the aforementioned configurations. The Pakdel–McKinley (PM) scaling arguments (McKinley *et al.* 1996; Pakdel & McKinley 1996) provide a unifying expression for the onset of hoop-stress-driven instabilities, given by

$$\frac{\lambda V}{\mathcal{R}} \frac{N_1}{|\tau|} \geqslant M_{crit}^2, \tag{1.1}$$

where λ is the (longest) relaxation time of the fluid, V is a characteristic velocity scale, $\mathcal{R}$ is the pertinent radius of curvature, N_1 is the first normal stress difference, τ is the total shear stress in the base-state and M_{crit} is an $O(1)$ number sensitive to the actual geometry.

The PM criterion cannot be satisfied for rectilinear shearing flows (with $\mathcal{R} \to \infty$), implying that hoop-stress-driven linear instabilities are absent in such flows. Hoop stresses in these flows can, however, become relevant at a nonlinear order, owing to curvature of the perturbed streamlines, as has been demonstrated within the framework of a weakly nonlinear stability analysis (Morozov & van Saarloos 2005*a*, 2007, 2019). The above-mentioned absence of a hoop-stress-driven linear instability had led to the viewpoint that purely elastic instabilities are restricted to curvilinear configurations, even if they are more complicated than the aforementioned canonical geometries (Haward *et al.* 2016), and that rectilinear viscoelastic shear flows are therefore linearly stable (Bertola *et al.* 2003; Pan *et al.* 2013).

In a significant departure from this paradigm, recent work by Khalid *et al.* (2021*b*) demonstrated that inertialess plane Poiseuille flow of an Oldroyd-B fluid is linearly unstable in the limit of high Weissenberg numbers ($Wi = \lambda V/H \sim 10^3$, V being the base-state maximum speed and H the channel half-width) and a near-unity solvent to solution viscosity ratio ($\beta > 0.99$); this corresponds to ultra-dilute highly elastic polymer solutions. The unstable mode has a phase speed close to the base-state maximum, belonging therefore to a class of 'centre modes', and the instability arises due to a critical-layer mechanism that does not rely on streamline curvature. Khalid *et al.* (2021*b*) further

https://doi.org/10.1017/jfm.2026.12002 Published online by Cambridge University Press

showed that, with increasing Re, the elastic centre-mode instability smoothly crosses over to the elastoinertial centre-mode instability, predicted in an earlier effort by Khalid *et al.* (2021*a*). Although a connection between the elastoinertial and elastic turbulent states was first speculated by Samanta *et al.* (2013) in their observations concerning the onset of elastoinertial turbulence in pipe flow of polymer solutions, the effort of Khalid *et al.* (2021*b*) for plane Poiseuille flow provided a rigorous demonstration of a connected linearly unstable region, across the elastoinertial range, and extending down to the inertialess limit. Kerswell & Page (2024) have recently carried out a matched asymptotic expansions analysis to capture this unstable centre mode. Further, Buza *et al.* (2022*b*) and subsequently Khalid *et al.* (2025) have shown using the FENE-P model, which accounts for finite extensibility of the polymer molecules, that the elastic centre-mode instability is present even for $Wi \sim O(100)$ and $\beta \approx 0.97$. Thus, use of the more realistic FENE-P model extends the unstable domain to experimentally accessible parts of the parameter space.

Recent efforts have identified an unstable centre mode in other rectilinear shearing flows as well. Yadav *et al.* (2024) have shown that the elastic centre-mode instability is present in the Couette–Poiseuille family (CPF), but only when the base-state velocity profile is non-monotonic, with a maximum within the flow domain; the instability being absent in plane Couette flow and, more generally, in shearing flows with monotonic velocity profiles. This intimate connection between the presence of a base-state maximum and the existence of a centre-mode instability is further corroborated by the presence of the latter in viscoelastic Kolmogorov flow (Kerswell & Page 2024; Lewy & Kerswell 2025); although the significance of this finding was not recognised in the original analysis of Boffetta *et al.* (2005). An analogue of the centre-mode instability was also shown to be present in viscoelastic film flow down an inclined plane (Priyadarshi *et al.* 2023), with a semi-parabolic base-state velocity profile.

Thus, there are two qualitatively different elastic instabilities that operate in viscoelastic shearing flows: (i) the hoop-stress mode ('HSM' henceforth), which requires the presence of streamline curvature, but exists even for monotonic velocity profiles (such as Taylor–Couette flow); and (ii) the elastic centre mode ('CM' henceforth), which does not rely on streamline curvature, but requires a non-monotonic base-state velocity profile. This raises the intriguing possibility that these modes might co-exist in flow configurations possessing both the aforementioned ingredients. That is to say, one has the potential for elastic instabilities of different physical origins in the same flow, a possibility that has not yet been explored in the literature. One such configuration is Dean flow – the flow in a curved channel driven by an azimuthal pressure gradient. In the Newtonian context, this configuration was first analysed by Dean & Chapman (1928), who showed the presence of a centrifugal instability. The threshold for this instability, in the narrow-gap limit, can be obtained from an inertial analogue of the above-mentioned PM criterion, with the Reynolds number Re replacing Wi; this was indeed pointed out by McKinley *et al.* (1996) while formulating their criterion for elastic instabilities. As alluded to already, Joo & Shaqfeh (1991, 1992, 1994) analysed the viscoelastic Dean flow problem, albeit in the inertialess limit ($Re = 0$), and showed the presence of an HSM instability in this configuration. One could also have a combination of an azimuthal pressure gradient and wall motion driving the flow, the resulting configuration being dubbed the 'Taylor–Dean' flow (Joo & Shaqfeh 1991) and being more easily realised in experiments.

We carry out a linear stability analysis of viscoelastic Dean flow to explore the relevance of both centre- and hoop-stress modes in a parameter space comprising Wi, β, and the gap-width ratio $\epsilon = d/\mathcal{R}$, d being the channel width. For the case where the curved channel is the gap between concentric rotating cylinders with R_2 and R_1 being the outer and inner

https://doi.org/10.1017/jfm.2026.12002 Published online by Cambridge University Press

cylinder radii, as is typically the case in experiments, $d = (R_2 - R_1)$ may be identified with the gap width, and the radius of curvature with R_1. We consider the inertialess regime in this effort and, therefore, set $Re = 0$. Traditionally, the HSM was first analysed in the narrow-gap limit (Larson *et al.* 1990; Joo & Shaqfeh 1991), corresponding to $\epsilon \ll 1$, with this assumption being relaxed in subsequent numerical investigations (Joo & Shaqfeh 1992, 1994). In the narrow-gap limit, for the hoop stress to remain relevant in the leading order radial momentum balance, one requires $\epsilon^{1/2} Wi \sim O(1)$. Here, $Wi = \lambda U_m/d$ is the Weissenberg number based on the gap width d and a velocity scale U_m associated with the Dean flow profile (defined later). Thus, in the narrow-gap limit, the critical Wi for the HSM instability must diverge as $\epsilon^{-1/2}$. In the same limit, the critical Wi for the CM instability is independent of ϵ and approaches that of plane Poiseuille flow (Khalid *et al.* 2021*a*). At a scaling level, therefore, as $\epsilon \to 0$, the critical Wi for HSM should eventually become larger than that for the CM. However, owing to the relatively large threshold, $Wi \sim O(10^3)$ for the CM (within the Oldroyd-B framework), it is necessary to carry out a stability analysis to determine the precise value of ϵ corresponding to this cross-over, and thereby assess its relevance to typical configurations used in experiments and applications. To this end, we present here a comprehensive account of the parameter regimes in which either of the aforementioned modes is the most unstable in viscoelastic Dean flow, by considering arbitrary gap-width ratios (ϵ), and by including both axisymmetric and non-axisymmetric disturbances.

Of particular relevance to the present effort is the recent preprint of Lu & Hof (2026) that reports experimental observations of instabilities in pressure-driven flow of polymer solutions through curved (helical) pipes; the curvature parameter here is d/R (ratio of pipe diameter to helical coil radius), and is the analogue of ϵ defined earlier. The authors find a CM instability in the limit $d/R \ll 1$, this being consistent with the earlier results of Choueiri *et al.* (2021) for straight pipes. The threshold Wi for the instability remains insensitive to increasing curvature until $d/R \approx 0.06$, beyond which there is a cross-over to an HSM, characterised by a threshold Wi that decreases with further increase in d/R. Interestingly, Lu & Hof (2026) show that the HSM continues to exist for $d/R < 0.06$, albeit as a secondary instability, occurring at a Wi higher than the CM threshold. In § 6, we show that the aforementioned picture is broadly consistent with our findings for the Dean flow configuration, and also expand on the nature of secondary transitions in both curved channel and pipe configurations.

While the existence of two types of elastic instabilities in the Dean flow configuration is of interest from the fundamental viewpoint, it is also significant from the applications perspective. Viscoelastic Dean flow is often used for hydrodynamic focusing of particles in curved (Nikdoost & Rezai 2020), spiral (Bai *et al.* 2023) and serpentine (Chen *et al.* 2024) microchannels. Although such experiments involve finite Reynolds numbers, the secondary flows emerging from the elastic instabilities reported in this study could certainly impact particle migration and, more generally, the efficiency of focussing protocols on microfluidic platforms. Polymer solutions are also used as displacing agents in enhanced oil recovery to remove capillary entrapments of oil in the pores. In this context, flow in serpentine microfluidic channels has been used to mimic the tortuous nature of the flow in porous media (Shakeri *et al.* 2021), wherein elastic instabilities are harnessed in triggering the breakup of large capillary entrapments and in the eventual removal of the same. Importantly, the elastic turbulence regime accessed in previous experiments involving serpentine microchannels (also regarded as an important means of achieving efficient mixing in microfluidic devices; see Groisman & Steinberg 2001, 2004) is either explicitly or implicitly understood as the eventual consequence of an initial

https://doi.org/10.1017/jfm.2026.12002 Published online by Cambridge University Press

hoop-stress-driven instability. Our findings suggest that there might exist two distinct pathways (*viz.*, an HSM-based route and a CM-based route, as suggested by the title) to the eventual turbulent regime and, perhaps, even two different kinds of turbulent states, depending on the wavelength of modulation of the serpentine channel.

We consider both the Oldroyd-B and FENE-P constitutive equations to model the viscoelastic fluid. The Oldroyd-B model has the necessary ingredients to capture both the HSM and CM, but owing to its prediction of a shear-rate-independent viscosity and first normal stress coefficient, it may be not accurate for fast shearing flows of polymer solutions (translating to a large threshold Wi for the CM in the present context) where shear thinning becomes important. This lacuna is due to the restrictive assumption of the polymer molecule being an infinitely extensible bead-spring dumbbell. The FENE-P model (Bird *et al.* 1980) overcomes this shortcoming by accounting for finite extensibility via the parameter L, the ratio of the fully extended length of the polymer (dumbbell) to its equilibrium size; the Oldroyd-B model being realised in the limit $L \to \infty$. The FENE-P model predicts shear thinning of both the viscosity and the first normal stress coefficient, and hence is a more realistic model at higher Wi. As will be shown later, consideration of finite extensibility is particularly important in the present scenario, on account of its contrasting effects on the HSM and CM instabilities. Well, why then should one consider the Oldroyd-B model at all? As noted by Shaqfeh & Khomami (2021), in their review article commemorating the birth centenary of James Oldroyd, the results obtained using the Oldroyd-B fluid have their own value in terms of providing a base reference, and (we quote) 'it is perilous. . .to ignore the analysis based on the Oldroyd-B model for any elastic flow problem'! We examine both axisymmetric and non-axisymmetric disturbances in the narrow-gap limit ($\epsilon \ll 1$), and for finite gap-width ratios ($\epsilon \sim O(1)$). The consideration of non-axisymmetric disturbances gains relevance because, while the HSM is present for axisymmetric disturbances, the CM is present even for two-dimensional disturbances. Even for the HSM, a non-zero azimuthal wavenumber can lead to a slight destabilisation in certain cases, as has been shown by Avgousti & Beris (1993) for viscoelastic Taylor–Couette flow.

The rest of this paper is organised as follows. The governing equations for both Oldroyd-B and FENE-P models are discussed in § 2.1. The base state velocity and stresses are discussed in § 2.2 for the Oldroyd-B model and in § 2.3 for the FENE-P model. The linearisation procedure is briefly introduced in § 2.4, with Appendices A and B providing the full system of linearised equations governing small amplitude disturbances in the respective cases. Since earlier efforts examining the Dean flow configuration have solely focused on the unstable modes, we begin here by discussing the nature of the complete elastic eigenspectrum for Dean flow of both Oldroyd-B and FENE-P fluids in § 3, with additional details of representative eigenspectra provided in Appendix C; §§ 3.1 and 3.2 discuss the eigenspectra for the axisymmetric and non-axisymmetric cases, respectively. We then discuss the CM instability in viscoelastic Dean flow in § 4. Herein, we first use the Oldroyd-B model in § 4.1 to map out the unstable parameter regimes for arbitrary ϵ, both for two- and three-dimensional perturbations, and then proceed to examine the role of finite extensibility (using the FENE-P model) in § 4.2. Section 5 begins with a brief recap of the key results for HSM within the Oldroyd-B framework, following which we examine the role of finite extensibility on the HSM for both axisymmetric (§ 5.1) and non-axisymmetric (§ 5.2) disturbances. Appendix D provides a brief compilation of eigenfunctions for the relevant unstable modes. Finally, § 6 provides a brief summary of the salient conclusions emerging from this effort, along with discussions on connection to experimental studies and on the various possible transition pathways in elastic Dean flow.

https://doi.org/10.1017/jfm.2026.12002 Published online by Cambridge University Press

Parameter	Dimensional variable	Scale	Dimensionless variable
Length	r^*	d (gap width)	r
Velocity	$\boldsymbol{v}^*$	U_m (average velocity)	$\boldsymbol{v}$
Time	t^*	$\dfrac{d}{U_m}$	t
Pressure	p^*	$\dfrac{\eta U_m}{d}$	p
Polymeric stress	$\boldsymbol{\tau}^*$	$\dfrac{\eta_p U_m}{d}$	$\boldsymbol{\tau}$
Disturbance frequency	ω^*	λ (relaxation time)	ω
Conformation tensor	$\boldsymbol{C}^*$	$k_B T/H_{sp}$	$\boldsymbol{C}$

Table 1. Non-dimensionalisation scheme adopted in this study. Most symbols are defined in the text. Here, H_{sp} is the equilibrium spring constant in the Oldroyd-B and FENE-P models, k_B is the Boltzmann constant, and T is the absolute temperature.

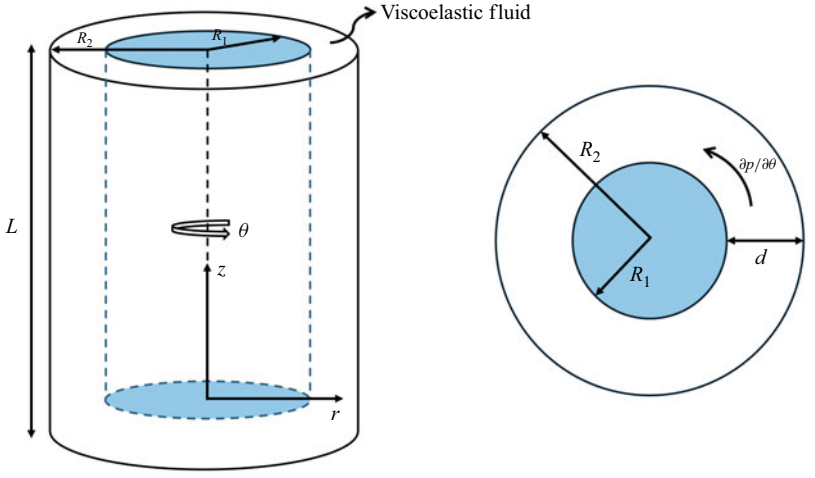


Figure 1. Schematic of the geometry and the coordinate system considered.

2. Problem formulation and numerical method

2.1. *Governing equations*

We consider steady, fully developed pressure-driven flow of a viscoelastic fluid between concentric cylindrical surfaces with radii R_1 and R_2 ($R_1 < R_2$), corresponding to a gap width $d = R_2 - R_1$; the gap-width ratio is defined as $\epsilon = d/R_1$. A cylindrical coordinate system with r, θ, z denoting the radial, azimuthal and axial coordinates, respectively, shown in figure 1, is used with the pressure gradient imposed along the azimuth. The scales used for rendering dimensionless the physical quantities, associated with both Oldroyd-B and FENE-P models, are summarised in table 1. The dimensionless continuity and inertialess Cauchy momentum equations take the form

$$\boldsymbol{\nabla}\cdot\boldsymbol{v} = 0, \tag{2.1}$$

$$0 = -\boldsymbol{\nabla}p + \beta\,\nabla^2\boldsymbol{v} + (1-\beta)\,\boldsymbol{\nabla}\cdot\boldsymbol{\tau}, \tag{2.2}$$

https://doi.org/10.1017/jfm.2026.12002 Published online by Cambridge University Press

with $\boldsymbol{v}$ and p being the velocity and pressure fields, and $\boldsymbol{\tau}$ the polymeric stress tensor. In (2.2), $\beta = \eta_s/\eta$ is the solvent to solution viscosity ratio, where $\eta = \eta_s + \eta_p$ is the total (zero-shear) solution viscosity with η_p and η_s being the zero-shear polymer and solvent viscosities, respectively.

In the Oldroyd-B model (Larson 1988), the polymer solution is modelled as a non-interacting suspension of Hookean dumbbells and the polymeric stress $\boldsymbol{\tau}$ is governed by

$$\boldsymbol{\tau} + Wi\left(\frac{\partial \boldsymbol{\tau}}{\partial t} + \boldsymbol{v}\cdot\nabla\boldsymbol{\tau} - \nabla\boldsymbol{v}^{\mathsf{T}}\cdot\boldsymbol{\tau} - \boldsymbol{\tau}\cdot\nabla\boldsymbol{v}\right) = \left(\nabla\boldsymbol{v} + \nabla\boldsymbol{v}^{\mathsf{T}}\right). \tag{2.3}$$

Here, $Wi = \lambda U_m/d$ is the Weissenberg number. In the FENE-P model, the dumbbells are finitely extensible and the polymeric contribution to the stress tensor is given by

$$\boldsymbol{\tau} = \frac{f\boldsymbol{C} - \boldsymbol{I}}{Wi}. \tag{2.4}$$

Here, $\boldsymbol{C}$ denotes the dimensionless conformation tensor, while $\boldsymbol{I}$ is the identity tensor representing the isotropic distribution of dumbbell conformations in the absence of an imposed flow. The Peterlin closure function f (Bird *et al.* 1980; Herrchen & Ottinger 1997) is defined as

$$f = \frac{L^2 - 3}{L^2 - tr(\boldsymbol{C})}, \tag{2.5}$$

where L represents the dimensionless extensibility parameter, de's maximum extension to its equilibrium root-mean-square value; the Oldroyd-B model being attained in the limit of infinite extensibility *viz.*, $L \to \infty$, when $f \to 1$. The conformation tensor is governed by the following evolution equation:

$$\frac{\partial \boldsymbol{C}}{\partial t} + \boldsymbol{v}\cdot\nabla\boldsymbol{C} - \nabla\boldsymbol{v}^{\mathsf{T}}\cdot\boldsymbol{C} - \boldsymbol{C}\cdot\nabla\boldsymbol{v} = -\boldsymbol{\tau}. \tag{2.6}$$

No-slip boundary conditions at the inner and outer cylinder walls apply to all velocity components. Since stress diffusion is neglected in the constitutive equations, no boundary conditions need be specified for either the polymeric stress or conformation tensors.

2.2. *Base state for the Oldroyd-B Model*

The base state velocity profile for Dean flow of an Oldroyd-B fluid is identical to its Newtonian counterpart (Diprima 1959; Joo & Shaqfeh 1992) and, therefore, independent of Wi. The non-dimensional velocity profile, after using the coordinate transformation $r^* = R_1(1+\epsilon y)$, is given by

$$\overline{\boldsymbol{v}} = \begin{bmatrix} \overline{v}_r \\ \overline{v}_\theta \\ \overline{v}_z \end{bmatrix} = \begin{bmatrix} 0 \\ U(y) \\ 0 \end{bmatrix}, \tag{2.7}$$

$$U(y) = \frac{-K\left[(1+\epsilon y) - \dfrac{1}{(1+\epsilon y)}\right] + \left[(1+\epsilon y)\ln(1+\epsilon y)\right]}{K\left[\dfrac{\ln(1+\epsilon)}{\epsilon}\right] - \dfrac{1}{4}(2+\epsilon)}, \tag{2.8}$$

where $K = (1+\epsilon)^2\ln(1+\epsilon)/(1+\epsilon)^2 - 1$ and the average velocity that has been used as the scale in (2.8) is given by $U_m = ((\partial p/\partial\theta)R_1/2\eta)(K[\ln(1+\epsilon)/\epsilon] - (1/4)(2+\epsilon))$. The

https://doi.org/10.1017/jfm.2026.12002 Published online by Cambridge University Press

polymer contribution to the base state stress tensor is given by

$$\overline{\boldsymbol{\tau}} = \begin{bmatrix} \overline{\tau}_{rr} & \overline{\tau}_{r\theta} & \overline{\tau}_{rz} \\ \overline{\tau}_{\theta r} & \overline{\tau}_{\theta\theta} & \overline{\tau}_{\theta z} \\ \overline{\tau}_{zr} & \overline{\tau}_{z\theta} & \overline{\tau}_{zz} \end{bmatrix} = \begin{bmatrix} 0 & U' - \dfrac{\epsilon}{1+\epsilon y}U & 0 \\ U' - \dfrac{\epsilon}{1+\epsilon y}U & 2Wi\left(U' - \dfrac{\epsilon}{1+\epsilon y}U\right)^2 & 0 \\ 0 & 0 & 0 \end{bmatrix}, \tag{2.9}$$

where $\zeta' \equiv D\zeta \equiv \mathrm{d}\zeta/\mathrm{d}y$.

2.3. *Base state for the FENE-P model*

The base state velocity field, conformation tensor and the polymer stress tensor in this case are given by

$$\overline{\boldsymbol{v}} = \begin{bmatrix} \overline{v}_r \\ \overline{v}_\theta \\ \overline{v}_z \end{bmatrix} = \begin{bmatrix} 0 \\ U(y) \\ 0 \end{bmatrix}, \tag{2.10}$$

$$\overline{\boldsymbol{C}} = \begin{bmatrix} \overline{C}_{rr} & \overline{C}_{r\theta} & \overline{C}_{rz} \\ \overline{C}_{\theta r} & \overline{C}_{\theta\theta} & \overline{C}_{\theta z} \\ \overline{C}_{zr} & \overline{C}_{z\theta} & \overline{C}_{zz} \end{bmatrix} = \begin{bmatrix} \dfrac{1}{\bar{f}} & \dfrac{Wi\,\overline{C}_{rr}\left(U' - \dfrac{U\epsilon}{1+\epsilon y}\right)}{\bar{f}} & 0 \\ \dfrac{Wi\,\overline{C}_{rr}\left(U' - \dfrac{U\epsilon}{1+\epsilon y}\right)}{\bar{f}} & \dfrac{1 + 2Wi\,\overline{C}_{r\theta}\left(U' - \dfrac{U\epsilon}{1+\epsilon y}\right)}{\bar{f}} & 0 \\ 0 & 0 & \dfrac{1}{\bar{f}} \end{bmatrix}, \tag{2.11}$$

$$\overline{\boldsymbol{\tau}} = \begin{bmatrix} \overline{\tau}_{rr} & \overline{\tau}_{r\theta} & \overline{\tau}_{rz} \\ \overline{\tau}_{\theta r} & \overline{\tau}_{\theta\theta} & \overline{\tau}_{\theta z} \\ \overline{\tau}_{zr} & \overline{\tau}_{z\theta} & \overline{\tau}_{zz} \end{bmatrix} = \begin{bmatrix} 0 & \overline{C}_{rr}\left(U' - \dfrac{U\epsilon}{1+\epsilon y}\right) & 0 \\ \overline{C}_{rr}\left(U' - \dfrac{U\epsilon}{1+\epsilon y}\right) & 2\overline{C}_{r\theta}\left(U' - \dfrac{U\epsilon}{1+\epsilon y}\right) & 0 \\ 0 & 0 & 0 \end{bmatrix}. \tag{2.12}$$

By combining (2.5) in the base state with $\overline{\tau}_{r\theta} = \overline{C}_{rr}(U' - (U\epsilon/1+\epsilon y)) = (U' - (U\epsilon/1+\epsilon y)/\bar{f})$ and eliminating $\bar{f}$, we obtain

$$\tau_{r\theta}^3 + \frac{L^2}{2Wi^2}\tau_{r\theta} - \frac{L^2}{2Wi^2}\left(U' - \frac{U\epsilon}{1+\epsilon y}\right) = 0. \tag{2.13}$$

This equation for $\tau_{r\theta}$ is coupled to $U(y)$ through the θ-component of (2.2), which provides a second relation between $\tau_{r\theta}$ and $U(y)$. The two equations are simultaneously solved, numerically, to obtain the base state fields; more details regarding the numerical procedure can be found from Tej *et al.* (2024). The base state velocity profile does depend on Wi and L, although only via the combination Wi/L for $L \gg 1$. Figure 2(*a*) illustrates the collapse of the profiles for different (Wi, L) pairs, with Wi/L fixed (and for $L \gg 1$). This collapse, first demonstrated by Yamani & McKinley (2023) for simple shear flow, was later generalised by Tej *et al.* (2024) to steady unidirectional rectilinear and curvilinear shear flows of a FENE-P fluid. Figure 2(*b*) shows velocity profiles for different Wi/L, for a fixed β. Interestingly, the maximum velocity, scaled by the average, is seen to exhibit

https://doi.org/10.1017/jfm.2026.12002 Published online by Cambridge University Press

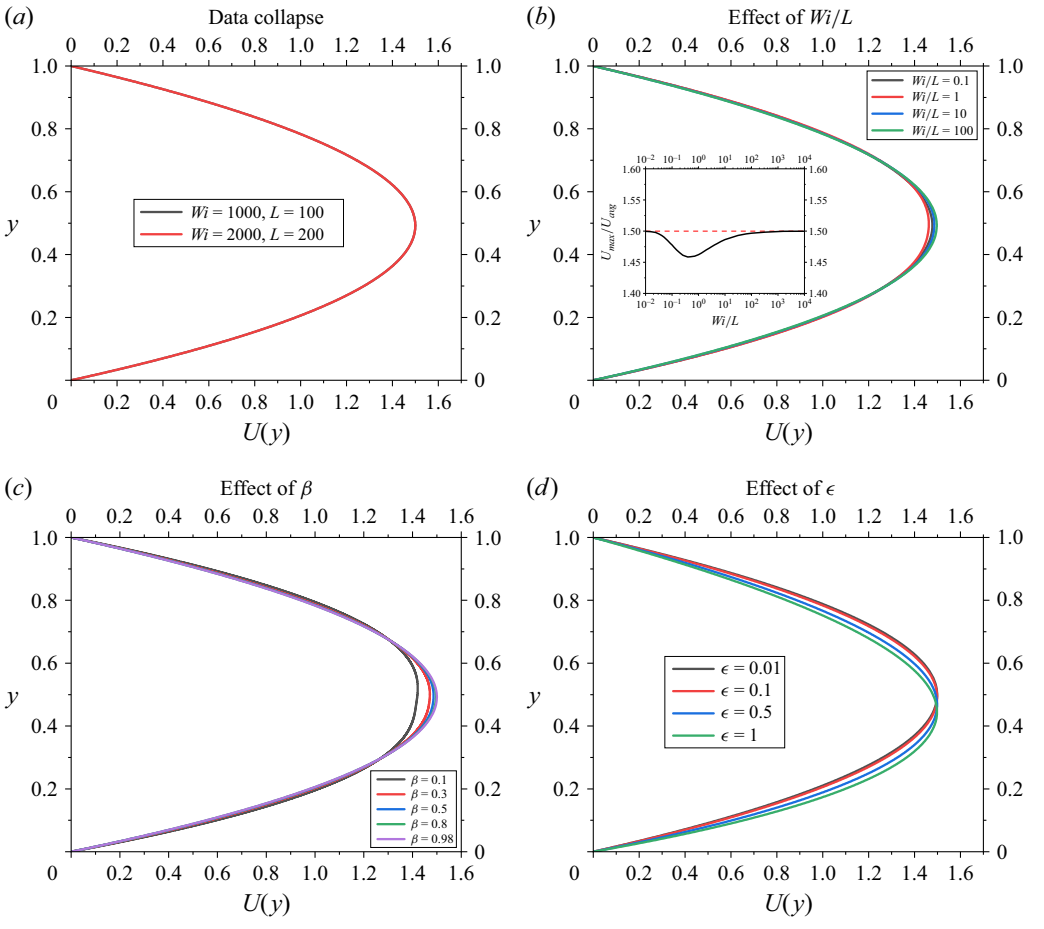


Figure 2. Dean flow velocity profiles for a FENE-P fluid: (*a*) $\beta = 0.98$ and $\epsilon = 0.1$ for two (Wi, L) pairs, with $Wi/L = 10$; (*b*) $\beta = 0.5$ and $\epsilon = 0.1$ with varying Wi/L. The inset shows the variation of the ratio of maximum to average velocities with Wi/L; (*c*) master curves for $Wi/L = 10$ and $\epsilon = 0.1$ for varying β; (*d*) master curves for $Wi/L = 10$ and $\beta = 0.9$ for varying ϵ.

a non-monotonic dependence on Wi/L (see inset of figure 2*b*). For small Wi/L, the profile expectedly assumes the Newtonian parabolic form and U_{max} equals $(3/2)\,U_{avg}$; for sufficiently large Wi/L, shear thinning ensures that the solvent contribution is dominant and U_{max} again approaches $(3/2)\,U_{avg}$. For intermediate Wi/L values, shear thinning leads to flatter profiles and a smaller β-dependent U_{max}. The aforementioned effect of changing β at a fixed Wi/L and ϵ is shown in figure 2(*c*), where shear thinning again leads to $U_{max}/U_{avg} < 1.5$, for the smaller β values; the profile reverts to the Newtonian form for $\beta \to 1$. Finally, the role of varying ϵ is shown in figure 2(*d*) where, for $\epsilon \ll 1$ (narrow-gap limit), the maximum velocity occurs at the centreline; this location shifting towards the inner cylinder for finite gap-width ratios.

2.4. *Linear stability analysis*

A temporal linear stability analysis is carried out wherein the aforementioned base states ((2.7)–(2.9) for the Oldroyd-B model and (2.10)–(2.12) for the FENE-P model)

https://doi.org/10.1017/jfm.2026.12002 Published online by Cambridge University Press

are subjected to small-amplitude perturbations. We consider both axisymmetric and non-axisymmetric disturbances in this study. The total velocity, pressure and stress are each expressed as the sum of a base-state contribution ($\overline{\chi}$) and an imposed perturbation ($\hat{\chi}$):

$$\chi = \overline{\chi} + \hat{\chi}, \tag{2.14}$$

where the variable χ represents any of the field variables. Next, the perturbation fields are assumed to be of the Fourier mode form:

$$\hat{\chi}(y, z, \theta, t) = \tilde{\chi}(y) \exp\left[\mathrm{i}\left(\alpha z + n\theta - \frac{\omega}{Wi}t\right)\right]. \tag{2.15}$$

Here, α and n are the axial and azimuthal wavenumbers, respectively, and $\omega = \omega_r + i\omega_i$ is the complex frequency. Since the frequency ω has been rendered dimensionless using the relaxation time and time t using the convective time scale d/U_m, then ω appears via the above-mentioned combination ω/Wi. Axisymmetric disturbances correspond to $n = 0$, while $\alpha = 0$ corresponds to two-dimensional perturbations varying in the r–θ plane; three-dimensional disturbances correspond to $\alpha \neq 0$ and $n \neq 0$. The flow is temporally unstable if $\omega_i > 0$. Substituting (2.15) in the linearised versions of (2.1), (2.2) and (2.3) leads to the set of governing equations, given in Appendices A and B for the Oldroyd-B and FENE-P models, respectively.

2.5. *Numerical methods*

We solved the linearised governing equations using a spectral method (Trefethen 2000; Weideman & Reddy 2000) and a shooting procedure. In the spectral method, we expand the dynamical variables as a finite sum of Chebyshev polynomials and substitute this expansion in the linearised governing equations – (A1)–(A10) for the Oldroyd-B model or (B1)–(B4) for the FENE-P model – to obtain a generalised eigenvalue problem as follows:

$$\boldsymbol{A}\boldsymbol{x} = \omega \boldsymbol{B}\boldsymbol{x}. \tag{2.16}$$

Here, $\boldsymbol{A}$ and $\boldsymbol{B}$ are coefficient matrices, with $\boldsymbol{x} = (\tilde{v}_r, \tilde{v}_\theta, \tilde{v}_z, \tilde{p}, \tilde{\tau}_{rr}, \tilde{\tau}_{r\theta}, \tilde{\tau}_{rz}, \tilde{\tau}_{\theta\theta}, \tilde{\tau}_{\theta z}, \tilde{\tau}_{zz})^T$ for the Oldroyd-B model and $\boldsymbol{x} = (\tilde{v}_r, \tilde{v}_\theta, \tilde{v}_z, \tilde{p}, \tilde{C}_{rr}, \tilde{C}_{r\theta}, \tilde{C}_{rz}, \tilde{C}_{\theta\theta}, \tilde{C}_{\theta z}, \tilde{C}_{zz})^T$ for the FENE-P model. The size of the $\boldsymbol{A}$ matrix is $10N \times 10N$, where N is the number of Gauss–Lobatto collocation points. The generalised eigenvalue problem is solved using the 'eig' solver of Matlab. Depending on the parameter regime, the number of collocation points N required to capture physically genuine eigenvalues differs. Convergence in this method is achieved by comparing the eigenspectra for two different values of N and filtering them using a prescribed tolerance. The shooting method is based on a Runge–Kutta integrator with a Gram–Schmidt orthonormalisation procedure (Ho & Denn 1977) and a Newton–Raphson iteration for the eigenvalue. This procedure is implemented only for the Oldroyd-B model. It is known that the spectral method can give unphysical (spurious) eigenvalues (Schmid & Henningson 2001), but the shooting method gives genuine eigenvalues, given a good initial guess. Thus, the genuineness of the eigenvalues, obtained from the spectral method, is confirmed by providing them as initial guesses for the shooting method. To benchmark the implementation of our numerical methodology in the narrow-gap limit, we compare (table 2 and figure 3) results from our procedure with those of Joo & Shaqfeh (1992), finding excellent agreement.

3. Nature of the elastic spectrum in Dean flow

Herein, we provide an overview of the elastic eigenspectrum for Dean flow, before proceeding to discuss the two classes of unstable modes (*viz.*, CM and HSM) in subsequent

https://doi.org/10.1017/jfm.2026.12002 Published online by Cambridge University Press

Dean flow	α_c	$\epsilon^{1/2}Wi_c$
Joo and Shaqfeh	6.6 ± 0.1	4.06 ± 0.02
Present	6.56	4.06

Table 2. Validation of UCM ($\beta = 0$) results with those of Joo & Shaqfeh (1992).

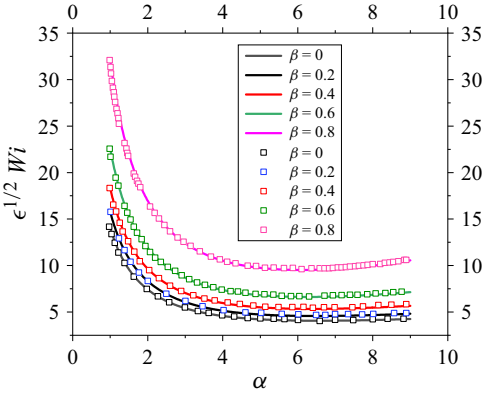


Figure 3. Benchmarking of neutral curves obtained from our numerical (spectral-cum-shooting) procedure (for $Re = 0$, $n = 0$) with those of Joo & Shaqfeh (1992) for Dean flow of an Oldroyd-B fluid, for different β. Continuous lines show results from the present work, while discrete points represent the data of Joo & Shaqfeh (1992).

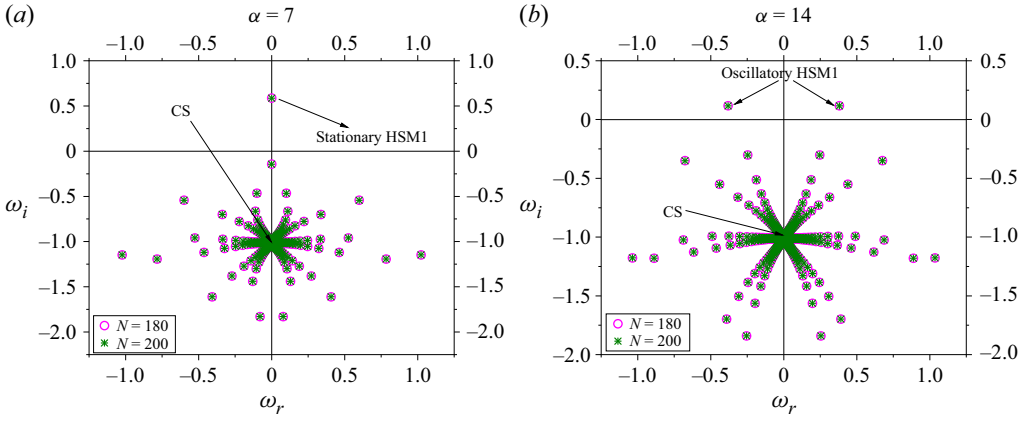


Figure 4. Eigenspectrum showing (a) stationary ($\alpha = 7$) and (b) propagating ($\alpha = 14$) modes of instability via the HSM1 mode in Dean flow of an Oldroyd-B fluid at $Re = 0$, $n = 0$, $\beta = 0.98$, $\epsilon = 0.1$ and $Wi = 25$.

sections. A clear understanding of the structure of the elastic spectrum is necessary to interpret the origin of different unstable modes and to also enable us to distinguish them from one another.

3.1. *Axisymmetric disturbances ($n = 0$)*

Figure 4 shows the axisymmetric elastic spectrum for Dean flow of an Oldroyd-B fluid at two different axial wavenumbers (α). For both α, there appear to be a large number

https://doi.org/10.1017/jfm.2026.12002 Published online by Cambridge University Press

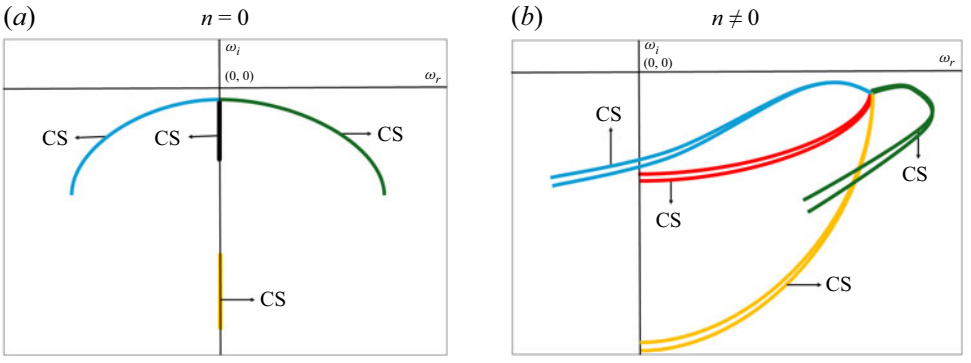


Figure 5. Schematic of the continuous spectra branches in Dean flow of a FENE-P fluid with $Wi/L \sim O(1)$ and $\beta \to 1$: (*a*) $n = 0$; (*b*) $n \neq 0$.

of discrete modes accumulating towards the point $(\omega_r, \omega_i) \equiv (0, -1)$ along multiple branches; the latter point is shown here to be a part of the continuous spectrum (CS) for $n = 0$. The numerical eigenvalues are likely a large but finite representation of infinite sequences, pertaining to the analytical eigenvalue problem, that converge to the aforementioned point CS. In this regard, we have verified that progressively more discrete eigenvalues are resolved in the neighbourhood of the CS, with no indication of the sequence terminating with increasing N. The spectra in figures 4(*a*) and 4(*b*) also include unstable modes – either stationary ($\omega_r = 0$; see figure 4*a*) or propagating ($\omega_r \neq 0$; see figure 4*b*) ones; in the latter case, they appear symmetrically on either side of the imaginary axis. For the stationary scenario, the least stable/most unstable of the discrete modes is the classical axisymmetric HSM, originally identified by Joo & Shaqfeh (1991, 1994), and is labelled 'HSM1' henceforth. A more detailed discussion of the parameter regimes in which HSM1 is stationary or propagating is provided in Appendix C. It will be seen therein that the stationary-to-propagating transition can happen with an increase in α for a fixed Wi or for a fixed α and with decreasing Wi.

Now, it is well known that the eigenspectra for viscoelastic flows also contain (stable) continuous spectra of eigenvalues (Wilson *et al.* 1999; Roy *et al.* 2022). These are obtained by setting the coefficient of the highest order derivative of the governing linearised equation for the wall-normal velocity perturbation to zero. For rectilinear flows such as plane Couette and Poiseuille flows of an Oldroyd-B fluid, this leads to two distinct CS with decay rates $\omega_i = -1$ and $\omega_i = -1/\beta$. In general, these CS are horizontal line segments in the ω_r–ω_i plane whose length is proportional to $k\Delta V$, with ΔV being the base range of velocities and k the streamwise wavenumber. Along similar lines, for Dean flow, the horizontal extent of the CS is proportional to $n\Delta V$. For Dean flow subjected to axisymmetric disturbances ($n = 0$) as in figure 4, the CS, within the Oldroyd-B framework, therefore degenerate to a pair of points on the imaginary axis with $\omega_i = -1$ and $-1/\beta$; the the two points approaching each other in the limit $\beta \to 1$ ($\beta = 0.98$ in figure 4).

We now turn to the effect of L on the spectra. As L is decreased, owing to shear thinning of rheological properties, the nature of CS for both rectilinear and curvilinear shearing flows, including Dean flow in particular, is significantly more complex compared with that for the above-mentioned Oldroyd-B fluid. In the interest of brevity, we provide here only the key features of the CS that are relevant to the present work; a detailed discussion can be found from Mohanty *et al.* (2026). A schematic of the CS for Dean flow, pertinent to the dilute-solution limit ($\beta \gtrsim 0.95$) and for $Wi/L \sim O(1)$ (so shear thinning effects remain significant), is shown in figure 5(*a*) for $n = 0$. As L is decreased from the Oldroyd-B limit,

https://doi.org/10.1017/jfm.2026.12002 Published online by Cambridge University Press

the 'point CS' on the imaginary axis, in the above-mentioned Oldroyd-B limit, turn into vertical line segments. The two line segments are shown to be distinct in the schematic, but may overlap depending on the particular choice of parameters. The reason underlying the extended CS, even for $n = 0$, is due to the variation of the base-state Peterlin function $\bar{f}$ as a function of the wall-normal coordinate, which leads to a range of relaxation times and, thence, decay rates. Concurrently, a pair of symmetrically placed 'wing'-like CS emerge on either side of the imaginary axis (Mohanty *et al.* 2026). The horizontal extent of the wings and the vertical line segments (belonging to the CS) increases with decreasing L. The computed numerical spectra illustrating these features are shown in figure 6 for different L at a fixed Wi.

Apart from the CS, the spectra in figure 6 also contain discrete modes, which are not depicted in the figure 5(*a*) schematic. In fact, figure 6(*a–h*) shows that decreasing L has a strong influence on the configuration of discrete modes. In contrast to the previous Oldroyd-B case, where there appeared to be multiple infinite sequences of discrete modes accumulating at the (point) CS, a decrease in L leads to a progressive reduction in the number of modes. When L is reduced to 398, the most unstable mode changes from a stationary one to a pair of propagating ones; this change is due to a coalescence of HSM1 and the next (least stable) mode, followed by a bifurcation. The propagating pair moves down towards the CS as L is decreased further; this shear-thinning-induced stabilisation is discussed further in § 5.1. Eventually, for $L = 100$, there are no discrete modes, either stable or unstable, and the spectrum comprises solely modes belonging to the CS for $Wi \gtrsim 16$ (see figure 6*h*).

3.2. *Non-axisymmetric disturbances ($n \neq 0$)*

The schematic of the CS for $n \neq 0$ is shown in figure 5(*b*) for FENE-P fluids with $Wi/L \sim O(1)$; again, the details of how these are obtained theoretically are discussed by Mohanty *et al.* (2026). There are four distinct CS (for $L \gtrsim 50$) in figure 5(*b*), with each of these comprising two branches. The branches arise due to the absence of a mid-plane symmetry in Dean flow and degenerate in the case of plane-Poiseuille flow. The actual numerical spectra for a non-zero n ($n = 1$) for both the Oldroyd-B and FENE-P cases, are shown in figures 7(*a*) and 7(*b*). In figure 7(*a*), we present the spectra for the same set of parameters as for the axisymmetric case ($n = 0$) in figure 6(*a*). For $n = 1$, the theoretical CS are no longer points even in the Oldroyd-B fluid, but are horizontal line segments located again at $\omega_i = -1$ and $-1/\beta$; these are only resolved as balloons in figure 7(*a*).

The constitution of the discrete modes in the spectra for $n = 1$ also differs qualitatively from those for $n = 0$. In particular, the discrete modes in figure 6(*a*) (for $n = 0$) with negative ω_r are virtually absent in the spectrum for $n = 1$ (see figure 7*a*). The absence is understandable since a negative ω_i implies a propagation in the direction opposite to the base state shear flow, which is an unlikely possibility in the absence of inertia. We have verified (data not shown) that as n is increased continuously from 0 to 1, there is also an overall reduction in the number of discrete modes; this reduction arising because many of these discrete modes disappear into the CS. In figure 7(*a*), the classical hoop-stress mode (HSM1) is the mode that dictates instability in the Oldroyd-B limit. This mode could be stationary or propagating for axisymmetric disturbances, but is propagating for non-axisymmetric disturbances.

Amidst the collection of other discrete modes, we also identify another mode (labelled 'HSM2'), which remains stable at the Wi chosen in figure 7(*a*). One reason behind singling out HSM2, amongst other discrete modes, maybe seen in figure 7(*b*), where it is unstable with a growth rate that is nearly equal to that of HSM1, for $L = 200$, albeit at a higher

https://doi.org/10.1017/jfm.2026.12002 Published online by Cambridge University Press

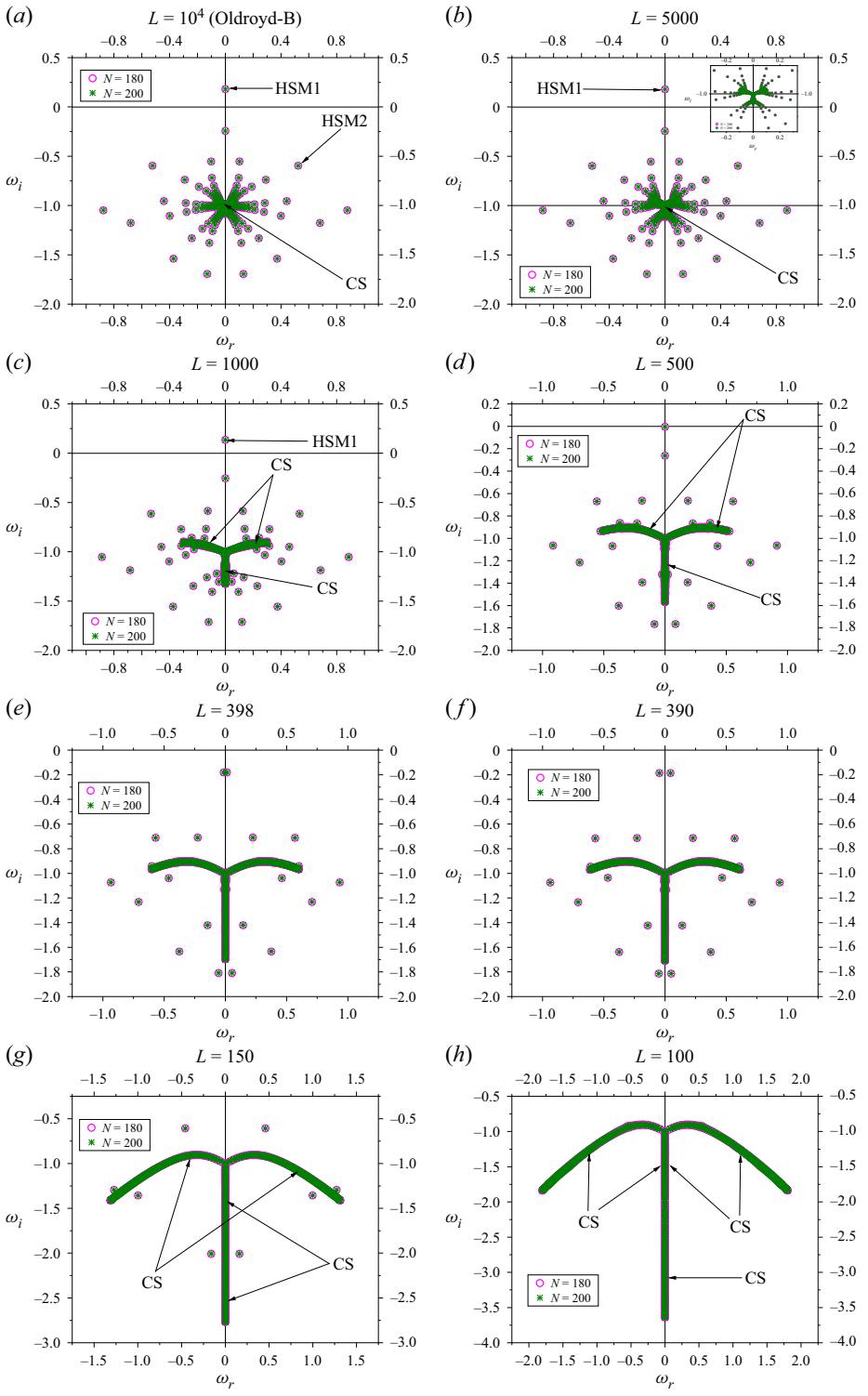


Figure 6. Eigenspectra for Dean flow of FENE-P fluids at different L; data for $n = 0$, $\epsilon = 0.1$, $\alpha = 7$, $\beta = 0.98$, $Wi = 20$ and $Re = 0$: (*a*) $L = 10^4$ (Oldroyd-B); (*b*) $L = 5000$; (*c*) $L = 1000$. (*d*) $L = 500$; (*e*) $L = 398$; (*f*) $L = 390$; (*g*) $L = 150$ and (*h*) $L = 100$.

https://doi.org/10.1017/jfm.2026.12002 Published online by Cambridge University Press

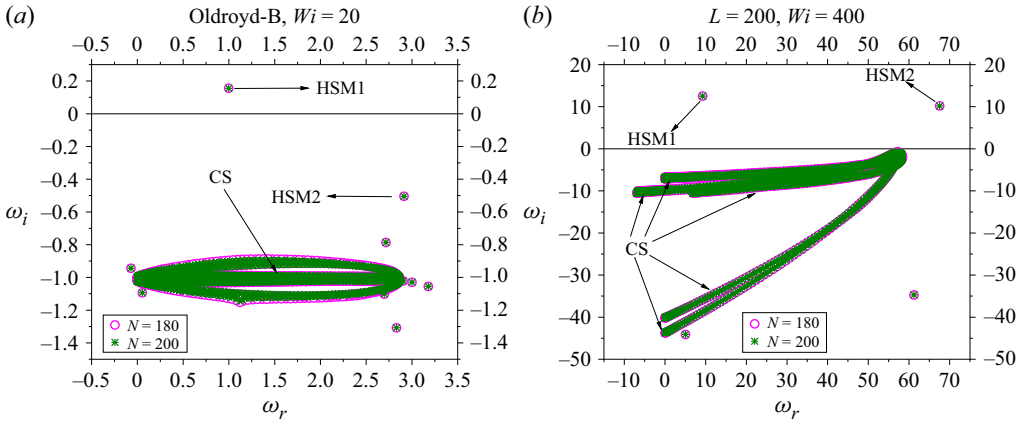


Figure 7. Eigenspectrum for non-axisymmetric ($n = 1$) disturbances showing both HSM1 and HSM2 in Dean flow of Oldroyd-B ($Wi = 20$) and FENE-P ($L = 200$, $Wi = 400$) fluids. Data for $\alpha = 7$, $\beta = 0.98$ and $\epsilon = 0.1$.

$Wi = 400$. Figure 8(*a–d*) shows the complete spectra for the Oldroyd-B fluid at different Wi, with both HSM1 and HSM2 identified, while figure 9 tracks the loci of HSM1 and HSM2 in the complex-ω plane with increasing Wi. The inset in this figure shows the variation of the growth rate with Wi for both modes. While an increase in Wi has a monotonic destabilising influence on HSM1, it has a non-monotonic effect on HSM2, with this mode being unstable only over an intermediate range of Wi, and eventually stabilising at sufficiently high Wi; the growth rates of HSM2 are much smaller compared with those of HSM1.

Returning to figure 7(*b*), the spectrum (for $L = 200$) also demonstrates the presence of multiple non-trivial CS branches, for $n \neq 0$, which nevertheless conform to the schematic shown in figure 5(*b*). While figure 7(*b*) is for $L = 200$, HSM2 is further destabilised with decreasing L, leading to it becoming the critical mode for sufficiently small L, in certain regions of the parameter space. This is in contrast to the Oldroyd-B limit, where HSM1 is always the critical mode. The detailed behaviour of HSM1 and HSM2 growth rates, for the FENE-P case, is discussed in § 5.2. It is nevertheless worth a brief mention here, since the unexpected destabilising effect of finite elasticity first seen for the CM by Buza *et al.* (2022*b*), is also present for HSM2.

We end our discussion with figure 10, which presents the elastic spectrum for $\beta = 0.994$ and $\epsilon = 0.1$; the spectrum now includes an unstable CM. The contrast in the choice of parameters, relative to the spectra in figures 4 and 6, is on account of the restricted nature of the unstable region in parameter space, in the limit of $\epsilon \to 0$, corresponding to plane Poiseuille flow – the centre-mode instability only exists for $\beta > 0.99052$ in this limit and for $Wi \sim O(300)$ (within the Oldroyd-B model; see Khalid *et al.* 2021*b*). It is pertinent to note here that the Weissenberg number used in the present study and the one used in the earlier effort of Khalid *et al.* (2021*b*) are related by a factor of three, as we elaborate in § 4.1. The role of decreasing L on the CM is discussed subsequently in § 4.2.

4. Elastic centre-mode instability in Dean flow

Having described the overall structure of the spectrum in the regions of parameter space relevant to the two elastic instabilities, we first focus on the results for the CM instability, using the Oldroyd-B model, both in the narrow- and finite-gap regimes. We then proceed to explore the role of finite extensibility. Owing to the difficulty in the experimental

https://doi.org/10.1017/jfm.2026.12002 Published online by Cambridge University Press

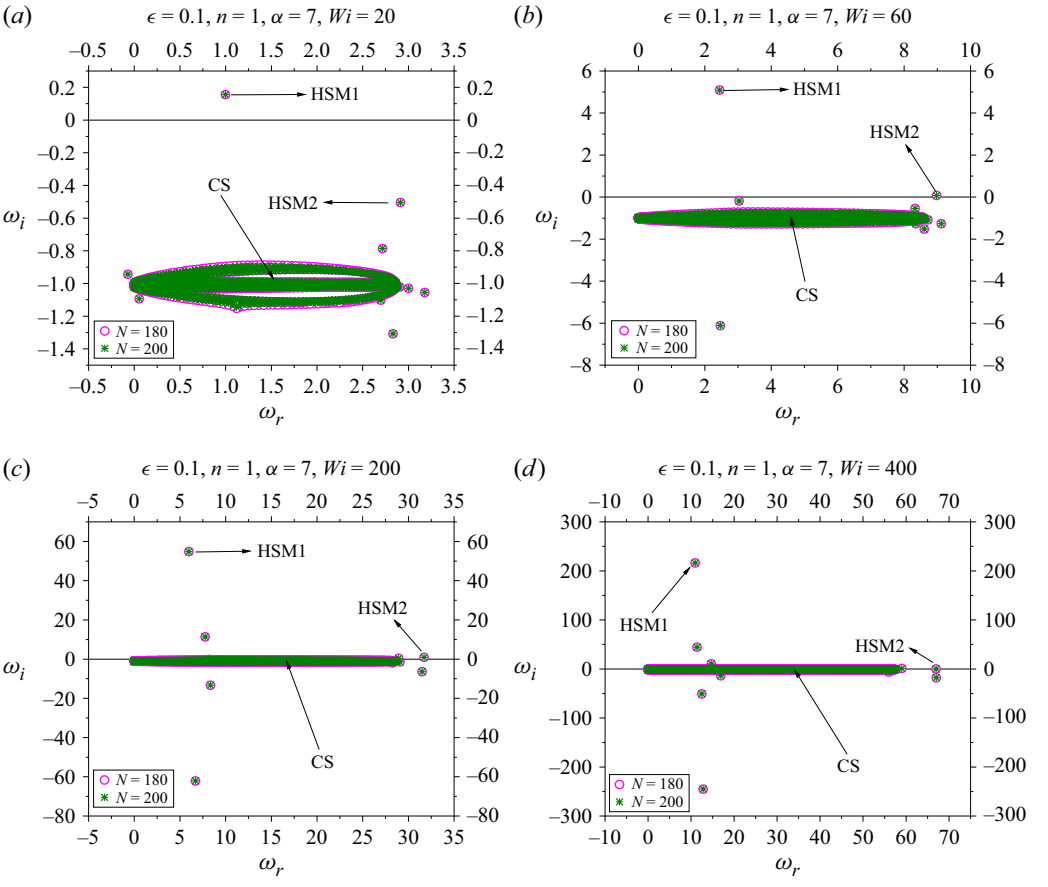


Figure 8. Eigenspectra showing HSM1 and HSM2 in Dean flow of an Oldroyd-B fluid at $Re = 0$, $\alpha = 7$, $\beta = 0.98$, $\epsilon = 0.1$, $n = 1$ for different Wi: (*a*) $Wi = 20$; (*b*) $Wi = 60$; (*c*) $Wi = 200$; (*d*) $Wi = 400$.

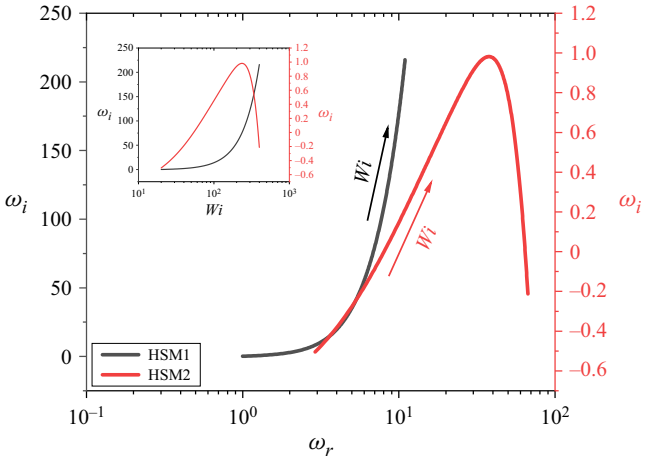


Figure 9. Variation of HSM1 and HSM2 growth rates with increasing Wi. Note the difference in scales of the left and right y-axes (for HSM1 and HSM2, respectively) on account of the vast difference in the growth rate magnitudes. The arrows indicate the direction of increasing Wi. The inset shows the variation of ω_i with Wi for both the modes. Data for $Re = 0$, $\alpha = 7$, $\beta = 0.98$, $\epsilon = 0.1$, $n = 1$.

https://doi.org/10.1017/jfm.2026.12002 Published online by Cambridge University Press

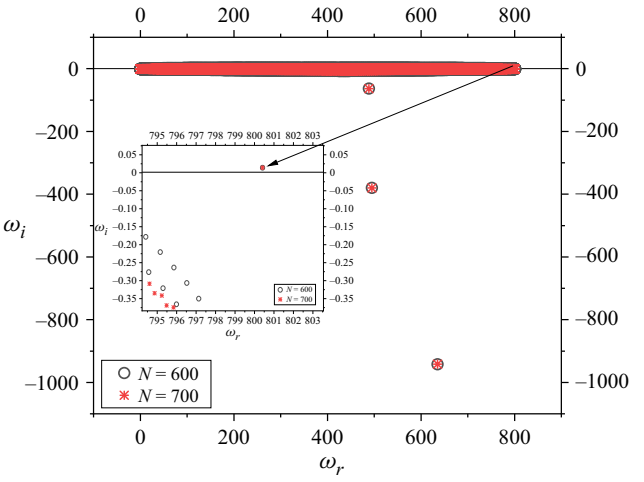


Figure 10. Eigenspectrum showing the presence of the centre mode in Dean flow of an Oldroyd-B fluid (with $n = 16$, $\epsilon = 0.1$, $\alpha = 0$, $\beta = 0.994$ and $Wi = 350$). The inset shows zoomed-in view highlighting the region near the unstable centre mode; the discrete eigenvalues obtained for $N = 600$ and $N = 700$ show good convergence.

realisation of pure Dean flow, the existing observations (by Joo & Shaqfeh 1994) are for a subset of the Taylor–Dean family with zero azimuthal flow rate. As noted in § 1, the latter was realised in the gap between concentric cylinders, with the flow driven by rotation of either cylinder, and with the (adverse) pressure gradient arising from a vertical obstruction in the gap at a particular azimuthal location. For this set-up, the unidirectional approximation for the base state velocity profile is strictly valid only for $\epsilon \ll 1$, when 'end effects' due to the azimuthal obstruction are negligible. For $\epsilon \sim O(1)$, the gap width is comparable to the radius of the inner cylinder and the velocity profile given by (2.8) will no longer be representative of the actual flow (which deviates from uni-directionality in a region whose size becomes comparable to R_1). Therefore, keeping in mind relevance to experiments, we restrict our results here to $\epsilon \leqslant 1$.

Before taking up the Dean flow stability characteristics in detail, it is instructive to recapitulate the known features of the CM instability in the channel flow geometry. As mentioned in § 1, channel flow of an Oldroyd-B fluid is susceptible to the CM instability in the highly elastic ultra-dilute limit. Khalid *et al.* (2021*b*) showed that the unstable mode has a phase speed close to the base-state maximum at the channel centreline (thence, the 'centre mode' terminology), with the critical Wi being $O(10^3)$. Furthermore, the most unstable mode is two-dimensional with no spanwise variation, owing to the existence of Squire's theorem for rectilinear shearing flows of an Oldroyd-B fluid (Bistagnino *et al.* 2007). However, at such high Wi, one expects shear thinning to become important (Khalid *et al.* 2025), potentially rendering the Oldroyd-B-based predictions less accurate. It is then appropriate to use the FENE-P model which accounts for shear thinning of both the viscosity and first normal stress coefficient. The general expectation is that shear thinning of the latter will weaken the elastic stresses, leading to a stabilising influence.

In contrast to the above-mentioned expectation, Buza *et al.* (2022*b*) showed that the critical Wi decreased to $O(100)$ upon using the FENE-P model with $L \sim 100$. Khalid *et al.* (2025) have built on this finding and presented a more comprehensive picture of the parameter regimes in which the elastic CM instability is present in channel flow of a FENE-P fluid. The authors showed that, while finite extensibility has the expected stabilising influence at lower elasticity numbers, the influence is a destabilising one at

https://doi.org/10.1017/jfm.2026.12002 Published online by Cambridge University Press

higher E, for $L \sim O(100)$. We show in § 6.1 that such L correspond to polyacrylamide solutions with molecular weights of $O(10^5)$, used in earlier experimental studies (Choueiri *et al.* 2021). As indicated previously, the most unstable CM in plane Poiseuille flow has a non-zero streamwise wavenumber and zero spanwise wavenumber, which translates, in the Dean flow context, to two-dimensional perturbations varying in the azimuthal direction with no axial variations. In other words, in contrast to the HSM, the CM instability can arise even in the two-dimensional limit with axially invariant perturbations. Nevertheless, the absence of Squire's theorem for any non-zero ϵ motivates us to also consider three-dimensional perturbations in the following, to arrive at the critical Wi as a function of ϵ. In light of Yadav *et al.* (2024)'s demonstration of the existence of the CM instability for members of the Couette–Poiseuille family with non-monotonic velocity profiles, the present Dean flow results should be relevant to the Taylor–Dean configuration as well, and thence, amenable to experiments (Joo & Shaqfeh 1994).

4.1. *Centre-mode instability within the Oldroyd-B framework*

In the narrow-gap limit, $\epsilon \ll 1$, the base state Dean profile approaches plane Poiseuille flow and we therefore begin with a validation of our numerical procedure by recovering the expected results (Khalid *et al.* 2021*b*) in this limit. To establish the connection between the two flows, note that the angular displacement θ in the Dean (cylindrical) geometry is the ratio of the arc length x^* to the radial distance r^*, that is, $\theta = x^*/r^*$. In the narrow-gap limit, $r^* = R_1(1+\epsilon y) \approx R_1$, and the previous relation reduces to $\theta = x^*/R_1$, leading to $n\theta = nx^*/R_1$. Thus, n/R_1 in cylindrical coordinates, for Dean flow, corresponds to the dimensional streamwise wavenumber k^* for plane Poiseuille flow; using $k^* = 2k/d$ gives $n = 2k/\epsilon$. Now, Khalid *et al.* (2021*b*) report the minimum critical Weissenberg number ($Wi_c = 973.8$) and critical wavenumber ($k_c = 0.783$) for $\beta = 0.994$, for the elastic CM in plane Poiseuille flow, with these values arising from use of the maximum speed (U_{max}) and half-gap width ($d/2$) as the characteristic velocity and length scales; the Weissenberg number and non-dimensional wavenumber being defined as $Wi_K = \lambda U_{max}/(d/2)$ and $k = k^* d/2$, respectively. In the present study, the Weissenberg number is defined as $Wi = \lambda U_m/d$. Noting that the ratio of maximum to mean speed is $3/2$ for plane Poiseuille flow, yields the following relation between the critical parameters: $Wi/Wi_K = 1/3$, $n_c = 2k_c/\epsilon$, in turn leading to $Wi_c = 324.6$ and $n_c = 1566$ in the narrow-gap limit; such high n do not necessitate an increased number of collocation points, for the spectral results shown in the following, since both the radial (ϵd) and azimuthal ($1/n \sim \epsilon$) scales decrease in direct proportion to ϵ.

Figure 11 shows the neutral curves in the Wi–n plane for ϵ ranging from 0.001 to 1. Also shown are the neutral curves obtained by Khalid *et al.* (2021*b*), highlighting the excellent agreement (for $\epsilon = 0.001$) between the Dean and channel flow cases. Although it was found convenient to vary n continuously, when tracking the neutral points in the Wi–n plane using the shooting procedure, it is worth keeping in mind that the discreteness of n implies that the critical Wi corresponds to the integer n closest to the minimum of the tongues in figure 11. There is a leftward movement of the neutral curves with increasing ϵ, as is expected from the $n \sim \epsilon^{-1}$ scaling for $\epsilon \ll 1$; although this movement slows down for finite ϵ. There is, in addition, an overall lowering of the unstable tongue, resulting in a decrease in the critical Weissenberg number Wi_c with an increase in ϵ. Figure 12 shows CM eigenfunction contours in the y–θ plane, over one azimuthal wavelength and for different ϵ. The plots for $\epsilon = 0.01$ and 0.1 clearly reveal the 'arrowhead' structure identified in earlier theoretical and computational efforts for the channel flow (Page *et al.* 2020; Khalid *et al.* 2021*a*), and observed experimentally in flow through straight pipes

https://doi.org/10.1017/jfm.2026.12002 Published online by Cambridge University Press

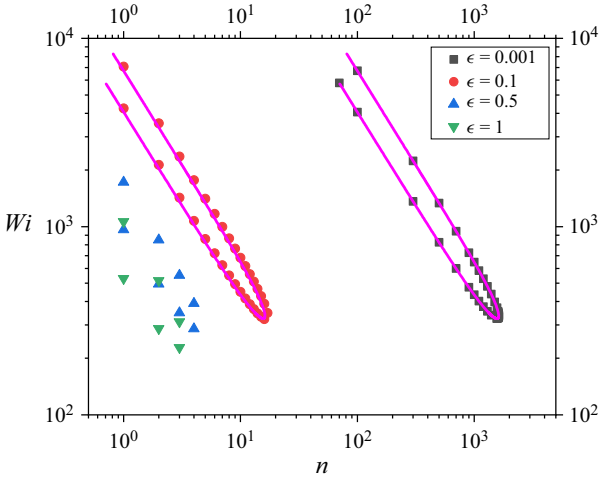


Figure 11. Centre-mode instability in Dean flow of an Oldroyd-B fluid at $Re = 0$, with $\alpha = 0$: Neutral curves in the Wi–n plane at different ϵ for $\beta = 0.994$. For $\epsilon = 0.001$ and 0.1, we also plot the neutral curve (continuous lines) obtained for pressure-driven flow in a rectilinear channel (Khalid *et al.* 2021*b*); incipient departure from the $n \sim \epsilon^{-1}$ scaling is evident in the comparison for $\epsilon = 0.1$.

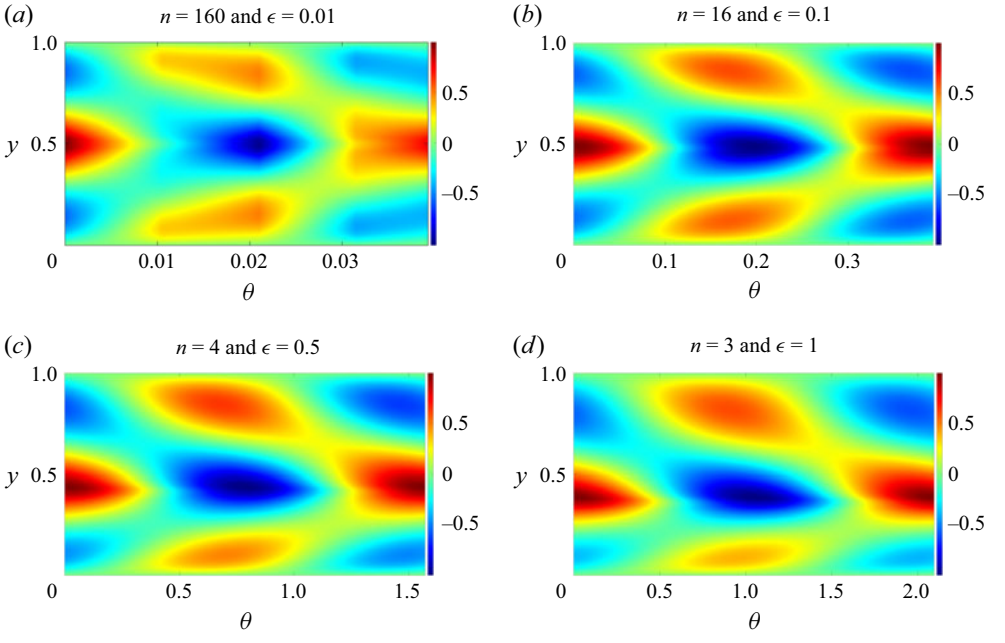


Figure 12. Structure of the CM eigenfunctions in the y–θ plane for Dean flow of an Oldroyd-B fluid with $\beta = 0.994$ and $\alpha = 0$; coloured contours represent the magnitude of the velocity perturbation $|\tilde{v}_\theta|$. Panels (*a*)–(*c*) show the progression of the modal structure with increasing curvature, at a constant Weissenberg number ($Wi = 350$); panel (*d*) shows the modal structure at $\epsilon = 1$ for $Wi = 230$.

by Choueiri *et al.* (2021), and through curved (helical) pipes by Lu & Hof (2026). The arrowhead is centred around the base-state maximum and tilted in a sense commensurate with the shear of the plane Poiseuille profile. For $\epsilon = 0.5$ and 1, curvature effects cause the structures near the inner wall to be significantly diminished in both scale and amplitude.

https://doi.org/10.1017/jfm.2026.12002 Published online by Cambridge University Press

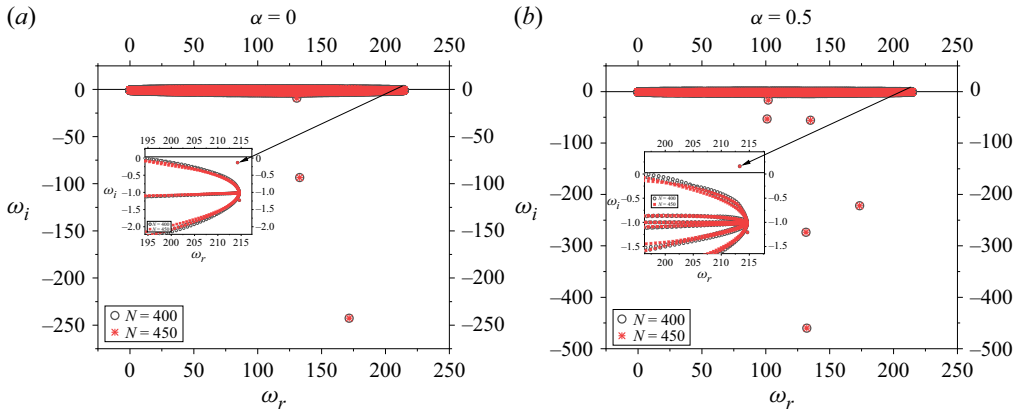


Figure 13. Eigenspectra showing the destabilising role of axially varying perturbations on the centre mode in Dean flow of an Oldroyd-B fluid. Data for $n = 1$, $\epsilon = 0.1$, $\beta = 0.98$ and $Wi = 1500$. The insets show the enlarged region of the spectra near the centre mode. (*a*) $\alpha = 0$; (*b*) $\alpha = 0.5$.

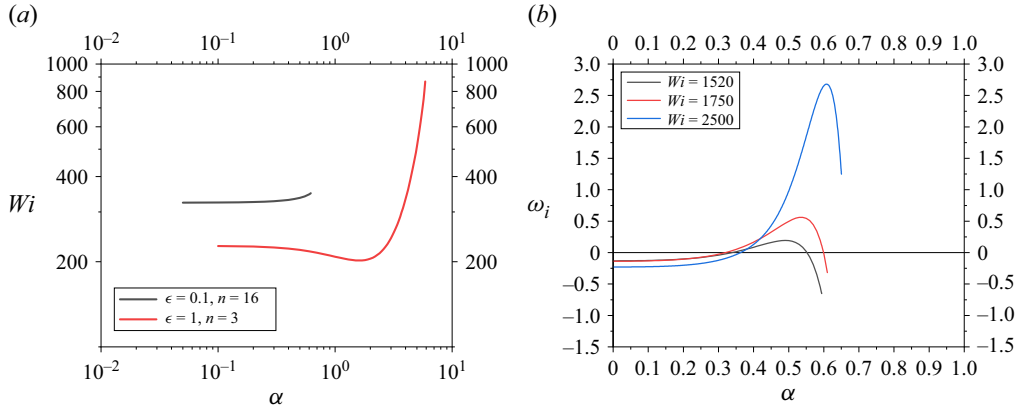


Figure 14. (*a*) Neutral curves in the Wi–α plane for two (ϵ, n) pairs for $\beta = 0.994$. (*b*) Variation of ω_i with α showing the destabilisation of the centre mode in Dean flow for non-zero α. Data for the Oldroyd-B fluid with $n = 1$, $\epsilon = 0.1$ and $\beta = 0.98$.

Next, figure 13 examines the role of axial variation ($\alpha \neq 0$) of perturbations. In figure 13(*a*), for the chosen parameter values, the CM is stable for two-dimensional disturbances ($n \neq 0$ and $\alpha = 0$). However, when three-dimensional disturbances are introduced (both $n \neq 0$ and $\alpha \neq 0$), surprisingly, the CM becomes unstable (figure 13*b*) – the introduction of an axial variation destabilises the centre mode. However, a further increase in α was found to lead to eventual stabilisation. This implies that to obtain the critical Wi, it is in principle necessary to minimise over both n and α. To this end, in figure 14(*a*), we show the neutral curves in the Wi–α plane for a fixed n, with the latter taken to be the critical value for $\alpha \to 0$. The monotonic increase in Wi_c with increasing α, for $\epsilon = 0.1$, appears to be consistent with the existence of Squire's theorem in the limit of $\epsilon \to 0$ (that is, for rectilinear shearing flows; see Bistagnino *et al.* 2007). That this is not the case is shown in figure 14(*b*), where we plot the variation of growth rate as a function of α for Wi significantly larger than the threshold for neutral stability, but for a β ($= 0.98$) that lies below the rectilinear channel-flow threshold for the chosen ϵ. Even for the relatively low value, $\epsilon = 0.1$, an increase in α is seen to lead to an unstable CM, where no such

https://doi.org/10.1017/jfm.2026.12002 Published online by Cambridge University Press

ϵ	n_c	Wi_c
0.001	1566	324.61
0.1	16	323.38
1	3	227.76

Table 3. Variation of critical Weissenberg number (Wi_c) with ϵ at $\beta = 0.994$ and $Re = 0$ for the centre mode in Dean flow of an Oldroyd-B fluid.

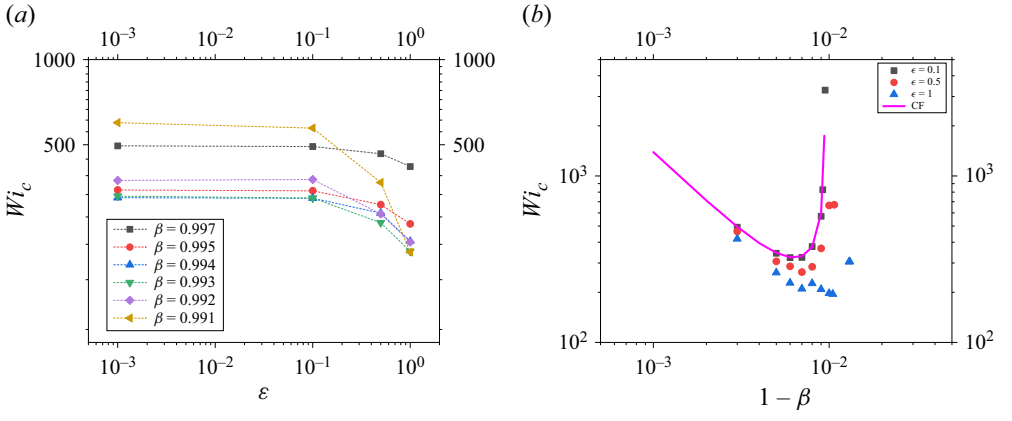


Figure 15. Centre-mode instability in Dean flow of an Oldroyd-B fluid at $Re = 0$, $\alpha = 0$: (*a*) variation of critical Weissenberg number (Wi_c) with ϵ at different β; (*b*) variation of Wi_c with $(1-\beta)$ at different ϵ. Here 'CF' represents the results for plane Poiseuille flow (Khalid *et al.* 2021*b*).

instability existed for $\alpha = 0$. The initial increase in growth rate is, however, followed by stabilisation for sufficiently large α. Returning to figure 14(*a*), the Wi–α neutral curve for $\epsilon = 1$ shows that, while there is an initial destabilisation (a decrease in Wi up until $\alpha \approx 2$, in contrast to $\epsilon = 0.1$), this is followed by a stabilising effect at sufficiently large α. On the whole, both the growth rates and the critical Wi exhibit a non-monotonic dependence on α. Thus, there exist three-dimensional perturbations that are more unstable than two-dimensional ones, this nevertheless being consistent with the absence of Squire's theorem for curvilinear geometries. The extent of decrease in Wi_c for $\epsilon = 1$ (from 227.76 for $\alpha = 0$ to 202.03 for $\alpha = 1.3$) is, however, not substantial and Wi_c for $\alpha = 0$ serves as a reasonably accurate estimate for the true threshold (obtained by minimising over both n and α). Thus, for the CM instability, in the ensuing discussion, we present the critical Wi_c obtained for two-dimensional disturbances.

Figure 15(*a*) shows the reduction in Wi_c with increasing ϵ for different β; representative data, corresponding to this figure, is given in table 3 for completeness. Figure 15(*b*) shows the variation of the critical Weissenberg number Wi_c with $(1-\beta)$ for different ϵ. The CM instability is seen to be restricted to $\beta \geqslant 0.99$ for $\epsilon \leqslant 0.1$, consistent with the β-threshold of 0.9905 for plane Poiseuille flow (Khalid *et al.* 2021*b*). The instability must clearly be absent for $\beta = 1$ and we indeed find that Wi_c diverges as $(1-\beta)^{-1}$ for $\beta \to 1$. Further, the unstable interval of β increases with increasing ϵ, implying that the instability is present over a larger range of polymer concentrations as domain curvature becomes important. Interestingly, the crossing of the different curves in figure 15(*a*) shows that, in addition to the increase in the unstable β-interval, it is the smallest β that become the most unstable

https://doi.org/10.1017/jfm.2026.12002 Published online by Cambridge University Press

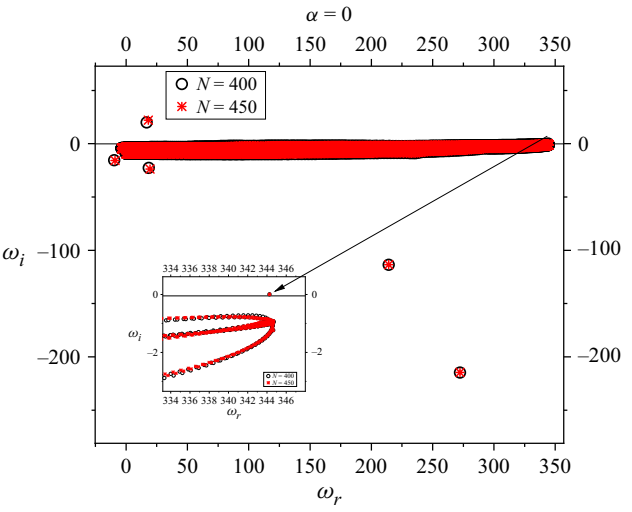


Figure 16. Eigenspectrum showing the presence of unstable centre mode in Dean flow of a FENE-P fluid (with $n = 40$, $\epsilon = 0.1$, $\alpha = 0$, $\beta = 0.98$, $L = 100$ and $Wi = 60$). The inset shows the zoomed-in view highlighting the region near the unstable centre mode; the discrete eigenvalues obtained for $N = 400$ and $N = 450$ show good convergence.

with increasing ϵ, in terms of having the smallest Wi-thresholds – this is consistent with both the widening and lowering of the unstable region in figure 15(b).

4.2. *Role of finite extensibility on CM in Dean flow*

To begin with, in figure 16, we present the elastic spectrum for the FENE-P fluid with $L = 100$ and $\beta = 0.98$, focusing on two-dimensional disturbances. Interestingly, the CM is unstable here, even at the relatively modest $Wi = 60$. The effect of decreasing L on the CM has been shown to be quite subtle in the case of channel flow (Khalid *et al.* 2025), in that it could be uniformly stabilising or destabilising, or even non-monotonic; we find a similar trend for Dean flow in the following. The effect of introducing axial variation was also investigated for $L = 100$ and we again found (data not shown) a slight destabilisation as α is increased up to approximately 1; a further increase in α leads to stabilisation, similar to the Oldroyd-B case discussed previously (figure 14a).

Khalid *et al.* (2025) first showed, for plane Poiseuille flow, that the neutral curves, for the FENE-P model, form closed loops in the Wi–k plane, as opposed to the open unstable tongues seen earlier in figure 11 for the Oldroyd-B case. The closing out of the tongues, leading to loops, is a manifestation of the expected stabilising role of shear thinning, which results in a weakening of elastic effects at sufficiently high Wi. As shown in figure 17(a), for Dean flow too, the neutral curves are closed loops in the Wi–n plane. Importantly, the destabilising effect of curvature (i.e. increasing ϵ) persists for the FENE-P model as well, as evident from the neutral loops in figure 17(a) shifting downward when ϵ is increased to $O(1)$ values. We also find very good agreement between the loop for $\epsilon = 0.01$ with the one obtained by Khalid *et al.* (2025) for channel flow. Furthermore, as shown in figure 17(b), the destabilising effect of L on the CM, originally predicted for channel flow (Page *et al.* 2020; Khalid *et al.* 2025), persists even for Dean flow at finite ϵ. Indeed, an obvious signature of the finite-extensibility-induced destabilisation is the fact that we continue to get unstable islands even for $\beta = 0.98$ in figure 17(a); the flow is stable for the Oldroyd-B model for this β.

https://doi.org/10.1017/jfm.2026.12002 Published online by Cambridge University Press

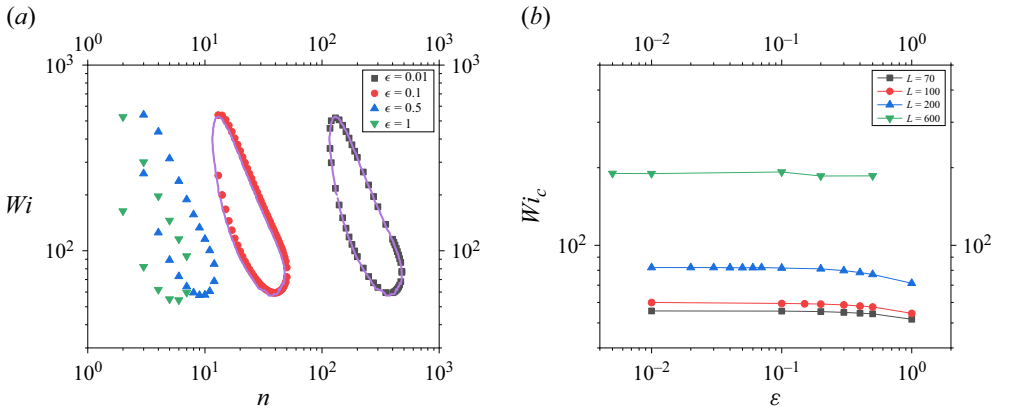


Figure 17. Centre-mode instability in Dean flow of a FENE-P fluid: (*a*) neutral curves at different ϵ for $L = 100$. For $\epsilon = 0.01$ and 0.1, we also plot the neutral curve (continuous lines) obtained for pressure-driven flow in a rectilinear channel (Khalid *et al.* 2025); (*b*) variation of Wi_c with ϵ at different L. Data for both panels correspond to $Re = 0$, $\alpha = 0$ and $\beta = 0.98$.

In Appendix C, we demonstrate that the CM instability is not governed solely by the ratio Wi/L (for different (Wi, L) pairs), although the base state profiles are, as was demonstrated in § 2.3. The eigenfunctions for various field variables, associated with the CM in Dean flow (for $L = 100$ and $\epsilon = 0.1$), are shown in Appendix D by way of comparison with those for the HSM. While key features of the CM eigenfunctions are rather robust to changes in ϵ and L, they remain qualitatively different from the corresponding HSM eigenfunctions.

5. Elastic hoop-stress instability in Dean flow

We first recall key results from the existing literature concerning the HSM in Dean flow; we do not review here the significant progress made in understanding the HSM in Taylor–Couette flow since its discovery by Larson *et al.* (1990). Despite sharing some similarities, there are many differences *vis-à-vis* the two HSM instabilities and the reader is referred to recent reviews (Shaqfeh & Khomami 2021; Castillo Sánchez *et al.* 2022; Datta *et al.* 2022) for the latest developments in this area. Suffice it to say that viscoelastic Taylor–Couette flow still commands significant interest among researchers, as can be seen from the recent experiments of Zhang *et al.* (2025), who showed that there is a continuous transition between the elastic and elastoinertial turbulent states in this flow, by probing elasticity numbers ($E = Wi/Re$) ranging over two orders of magnitude.

Following the identification of a purely elastic instability in the Taylor–Couette set-up by Larson *et al.* (1990), Joo & Shaqfeh (1991, 1994) first demonstrated, using the Oldroyd-B model, the presence of an inertialess HSM instability in the Dean as well as Taylor–Dean configurations. The authors assumed axisymmetric disturbances to begin with, and used the narrow-gap limit to show the emergence of an HSM for $Wi \gtrsim \epsilon^{-1/2}$; subsequently, the authors explored finite ϵ and non-axisymmetric disturbances. As mentioned in § 4, the authors also carried out experiments in a zero-flow-rate Taylor–Dean configuration, finding qualitative (but not quantitative) agreement between experimental and theoretical thresholds. In contrast to the Taylor–Couette configuration (Avgousti & Beris 1993; Joo & Shaqfeh 1994), the unstable mode in Dean flow is stationary and axisymmetric. Later, Ramanan *et al.* (1999) demonstrated the stabilising effect of an imposed axial flow on the Dean flow HSM, again focusing on stationary, axisymmetric modes.

https://doi.org/10.1017/jfm.2026.12002 Published online by Cambridge University Press

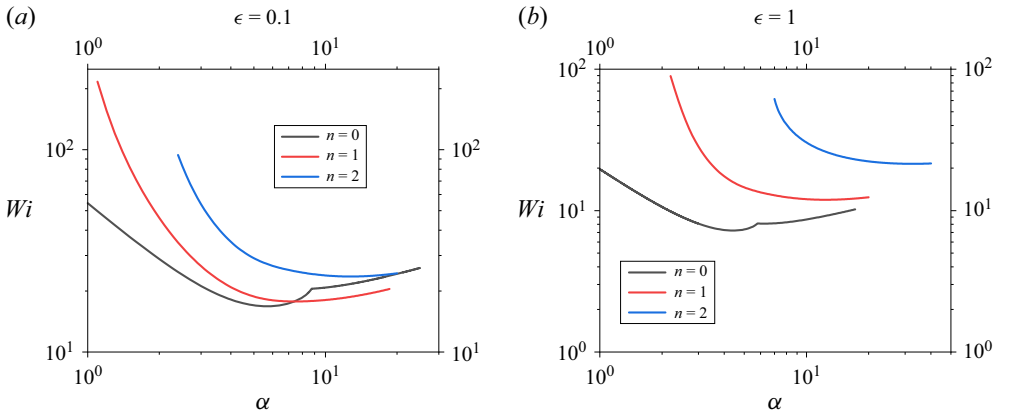


Figure 18. HSM1 neutral curves for both axisymmetric and non-axisymmetric disturbances at different ϵ: (*a*) $\epsilon = 0.1$ (*b*) $\epsilon = 1$. Data for the Oldroyd-B model ($Re = 0$ and $\beta = 0.98$).

The previous conclusions were arrived at within the Oldroyd-B framework. With the narrow-gap limit in mind, it is natural to enquire as to how these conclusions are modified at higher Wi, using more accurate nonlinear constitutive models. Over the past decade, several experiments (Dutcher & Muller 2013; Schaefer *et al.* 2018; Lacassagne *et al.* 2021; Steinberg 2021; More *et al.* 2024) have explored elastic instabilities in various curvilinear geometries, in regimes where shear thinning is important, making the case for nonlinear constitutive models even more compelling. In some of the aforementioned efforts, the polymer concentration is high enough for the polymers to be entangled, necessitating the use of models that account for reptation, such as the Rolie–Poly model (Likhtman & Graham 2003). Our focus is on shear thinning in relatively dilute solutions and, in this regard, we mention the efforts of Byars *et al.* (1994) and McKinley *et al.* (1995), which used the FENE-CR model to demonstrate the stabilising role of finite extensibility in torsional flows and in the cone-and-plate configuration. While this finite-extensibility-induced stabilisation can been made more precise (Castillo Sánchez *et al.* 2022) by accounting for shear thinning of the first normal stress coefficient within the Pakdel–McKinley framework, rather surprisingly, we are not aware of the Dean flow HSM being analysed quantitatively using either the FENE-P or FENE-CR models.

As a first step, we use here the FENE-P model to examine the Dean flow HSM. As evident from figures 4 and 7 of § 3, the Oldroyd-B model predicts both axisymmetric (stationary or propagating, depending on α) and non-axisymmetric (propagating) modes to turn unstable. The neutral curves in the former case were already shown in figure 3, in the narrow-gap limit, in the context of the validation exercise. The comparison between the axisymmetric and non-axisymmetric thresholds is shown in figures 18(*a*) and 18(*b*), which plot the neutral curves for $\epsilon = 0.1$ and 1, respectively. For both ϵ, the axisymmetric mode is the most critical, consistent with the earlier efforts of Joo & Shaqfeh (1991, 1994). A distinct kink is observed in the associated neutral stability curves (at both ϵ shown), owing to the bifurcation from stationary to propagating modes (Appendix C).

Recall from the discussion in § 1 that, for $\epsilon \ll 1$, Wi_c diverges as $\epsilon^{-1/2}$ for the axisymmetric HSM. Accordingly, in figure 19(*a*), $\epsilon^{1/2} Wi_c$ is almost independent of ϵ until $\epsilon \approx 0.1$, followed by a mild increase as ϵ is increased from 0.1 to 1. Unlike the CM instability, which is present only for $\beta > 0.99$ in plane Poiseuille flow within the Oldroyd-B framework, the hoop-stress mode (HSM1) is present even in the absence of solvent ($\beta = 0$), as was already evident from figure 3 (an exception is the CM instability

https://doi.org/10.1017/jfm.2026.12002 Published online by Cambridge University Press

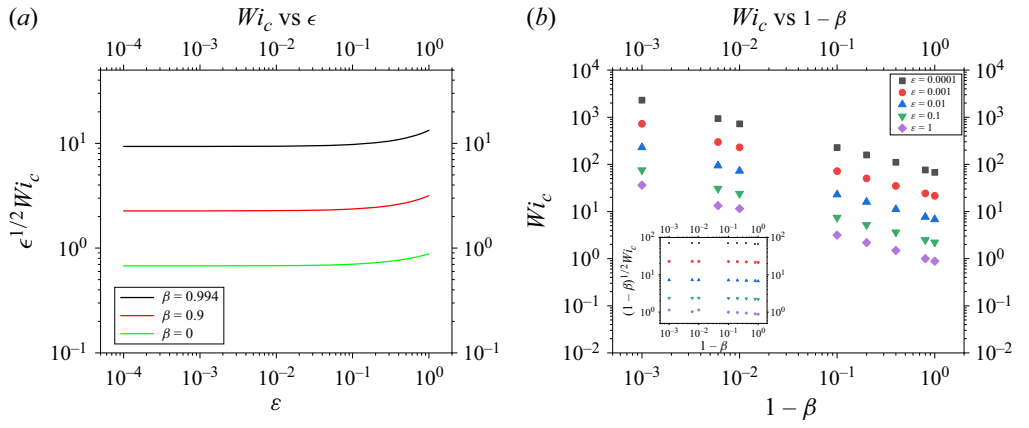


Figure 19. Critical Weissenberg number (Wi_c) for HSM1 in Dean flow of an Oldroyd-B fluid at $Re = 0$ and $n = 0$: (*a*) $\epsilon^{1/2}Wi_c$ as a function of ϵ for various values of β; (*b*) Wi_c as a function of $1-\beta$ for different gap width ratios ϵ; the inset shows $(1-\beta)^{1/2}Wi_c$ remains approximately a constant as β is varied.

in Kolmogorov flow which has been shown to exist even for $\beta \to 0$, by Lewy & Kerswell 2025). Both instabilities must cease to exist for $\beta \to 1$, with the critical Wi_c for the HSM diverging as $(1-\beta)^{-1/2}$ in this limit – figure 19(*b*) shows that this scaling continues to hold for any $\beta \in [0, 1)$. The scaling can be anticipated from the Pakdel–McKinley argument – using $\mathcal{R} = R_1$, $N_1 \propto \lambda\eta_p(U_m/d)^2$ and the total shear stress $|\tau| \propto \eta U_m/d$ in (1.1), we obtain

$$\frac{\lambda U_m}{R_1}\frac{\lambda\eta_p(U_m/d)^2}{\eta U_m/d} \geqslant O(1). \tag{5.1}$$

Upon using $\epsilon = d/R_1$ and $\eta_p/\eta = (1-\beta)$, (5.1) becomes

$$\left(\frac{\lambda U_m}{d}\right)^2 \epsilon(1-\beta) \geqslant O(1), \tag{5.2}$$

which yields $Wi_c \geqslant (\epsilon(1-\beta))^{-1/2}$; the divergence exponent $-1/2$ applies to both ϵ and $(1-\beta)$. In contrast, Wi_c for the CM is ϵ-independent in the narrow-gap limit, while scaling as $(1-\beta)^{-1}$ for $\beta \to 1$ (figure 15*b*); this scaling regime being followed by a rapid increase and divergence at a (slightly lower) threshold $\beta \approx 0.99$.

5.1. *Role of finite extensibility on axisymmetric modes*

In figure 20, we show the neutral curves for HSM1 (the most critical mode in the Oldroyd-B model) in the Wi–α plane for L ranging from the Oldroyd-B limit down to 100. The eigenspectra corresponding to these neutral curves were presented in figure 6. Owing to the stabilising role of finite extensiblity at large Wi, the neutral stability curves for finite L are again closed loops in the Wi–α plane for the entire range of gap width ratios examined, analogous to the neutral loops for the CM in figure 17(*a*). Similar closing out of the neutral curves due to shear-thinning-induced weakening of the first normal stress difference has been demonstrated using the Giesekus (Oztekin *et al.* 1994) and FENE-CR (McKinley *et al.* 1995) models for the HSM in the cone-and-plate geometry. Unlike the Oldroyd-B model, which exhibits a kink due to a transition from stationary to propagating modes, for the L shown in figure 20, the transition to instability occurs via propagating modes for all ϵ shown.

https://doi.org/10.1017/jfm.2026.12002 Published online by Cambridge University Press

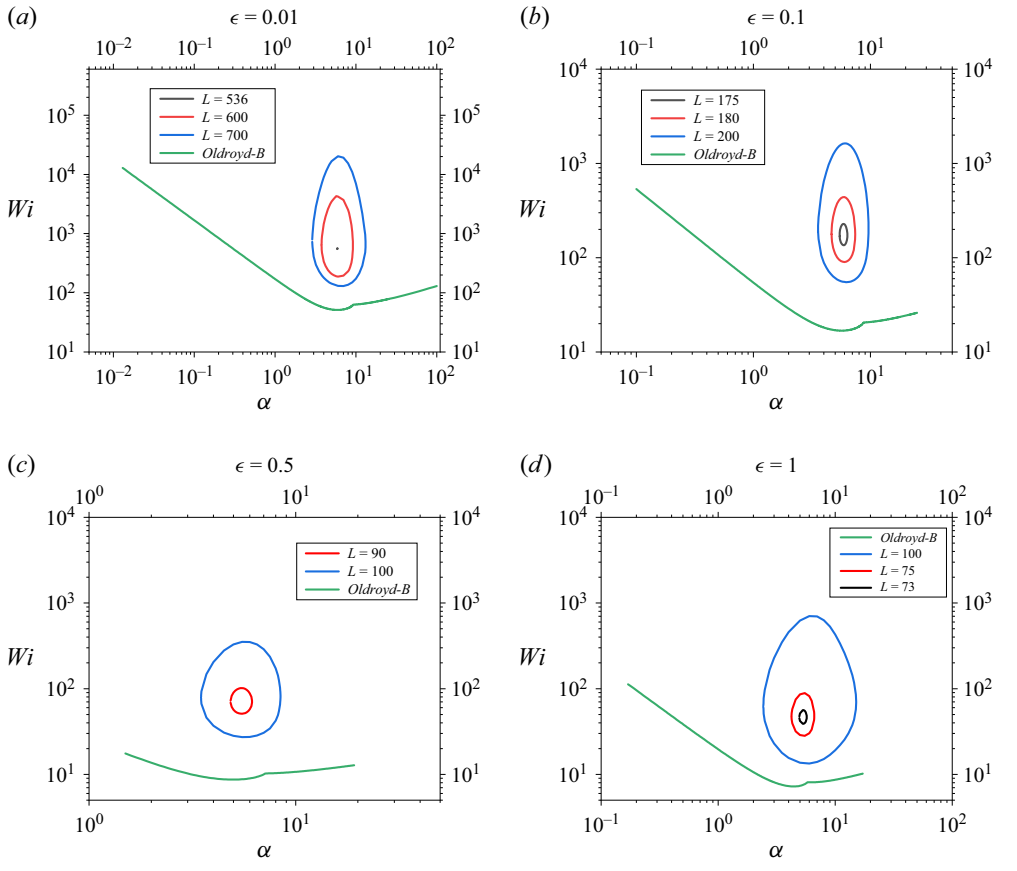


Figure 20. Neutral curves for HSM1 in the Wi–α plane for Dean flow of a FENE-P fluid at $Re = 0$, $\beta = 0.98$, $n = 0$: (*a*) $\epsilon = 0.01$; (*b*) $\epsilon = 0.1$; (*c*) $\epsilon = 0.5$ and (*d*) $\epsilon = 1$.

For the Dean flow examined here, shear-thinning-induced stabilisation, as expected, is strongest for the smallest ϵ ($= 0.01$), owing to the high Wi – the unstable loop in figure 20(*a*) already is vanishingly small at $L = 536$. In contrast, for $\epsilon = 0.1$, the loop remains finite in extent, even for $L = 175$. This sensitivity to ϵ is further highlighted in figure 21, where we show neutral stability loops in the Wi–α plane for $L = 100$, over a range of ϵ. The size of the unstable region decreases with decreasing ϵ for the said L, with the HSM being absent for $\epsilon \lesssim 0.36$. For smaller ϵ, it is necessary to further examine modes with $n \neq 0$ to ascertain the presence of an HSM instability, which we do in the next subsection.

5.2. *Role of finite extensibility on non-axisymmetric modes*

To begin with, we recall the discussion in § 3.2 which had identified HSM2, a second discrete mode in the elastic spectrum, other than the dominant one (HSM1) that governed the transition for the Oldroyd-B case. Herein, we examine HSM1 and HSM2 for the FENE-P case in more detail. Thus, while figure 7(*b*) was for $L = 200$, figure 22 examines the non-axisymmetric spectra (again for $n = 1$) for L decreasing from 10^6 (the Oldroyd-B limit for all practical purposes) down to 100. Decreasing L has a stabilising effect on HSM1, as one might anticipate from the role of shear thinning on the hoop-stress instability in our earlier discussion – HSM1 is, in fact, a stable mode in figure 22(*c*) for $L = 100$.

https://doi.org/10.1017/jfm.2026.12002 Published online by Cambridge University Press

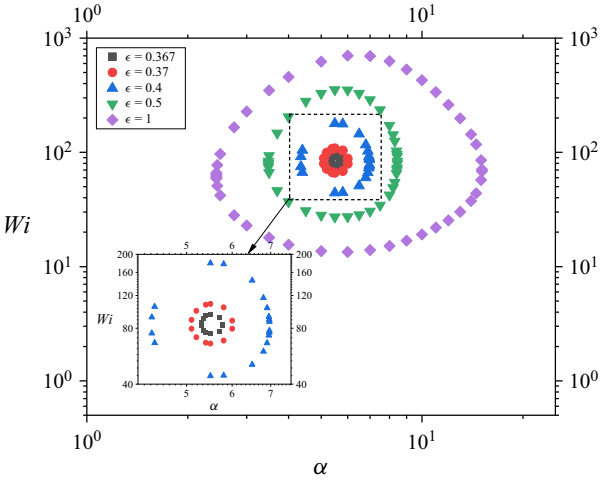


Figure 21. Neutral curves for HSM1 at different ϵ showing the absence of HSM1 for $\epsilon \lesssim 0.36$. Data for $Re = 0$, $n = 0$, $\beta = 0.98$ and $L = 100$. The inset shows an enlarged view of the region $40 < Wi < 200$.

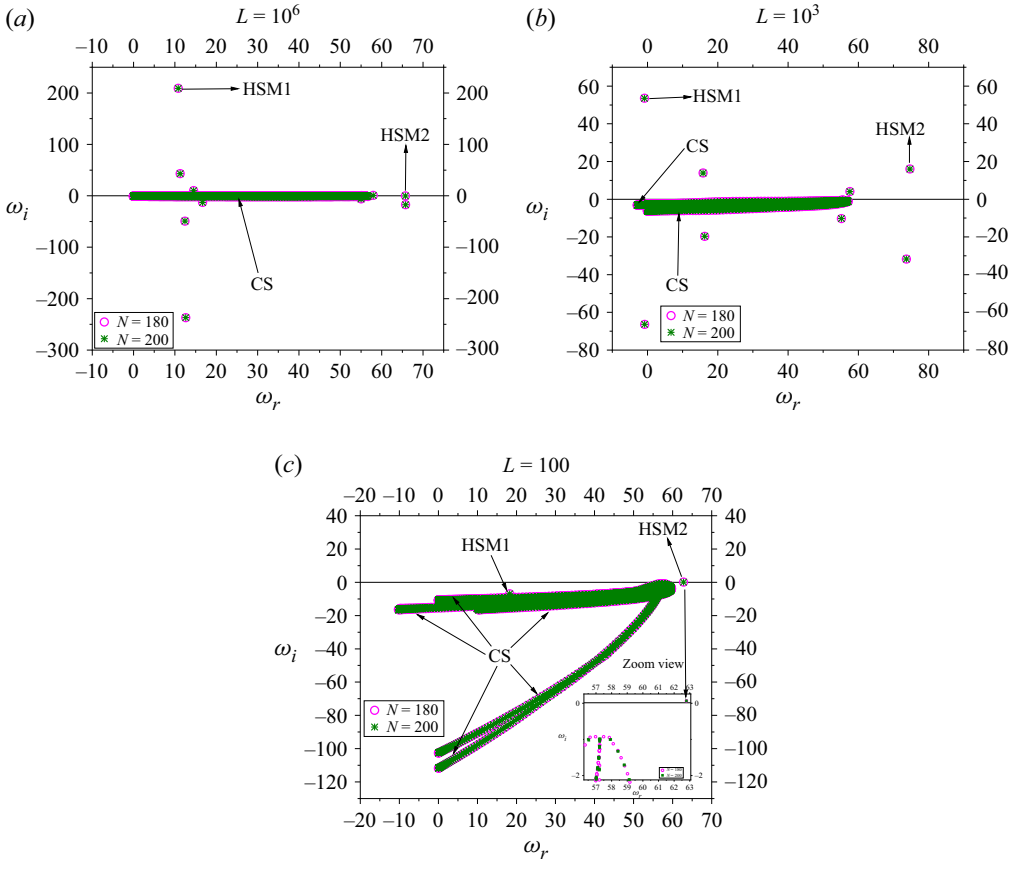


Figure 22. Eigenspectra showing HSM1 and 2 in Dean flow of a FENE-P fluid at $Re = 0$, $\alpha = 7$, $\beta = 0.98$, $\epsilon = 0.1$, $n = 1$, $Wi = 400$ at different L: (*a*) $L = 10^6$; (*b*) $L = 10^3$ and (*c*) $L = 100$. The continuous spectra are indicated as 'CS'.

https://doi.org/10.1017/jfm.2026.12002 Published online by Cambridge University Press

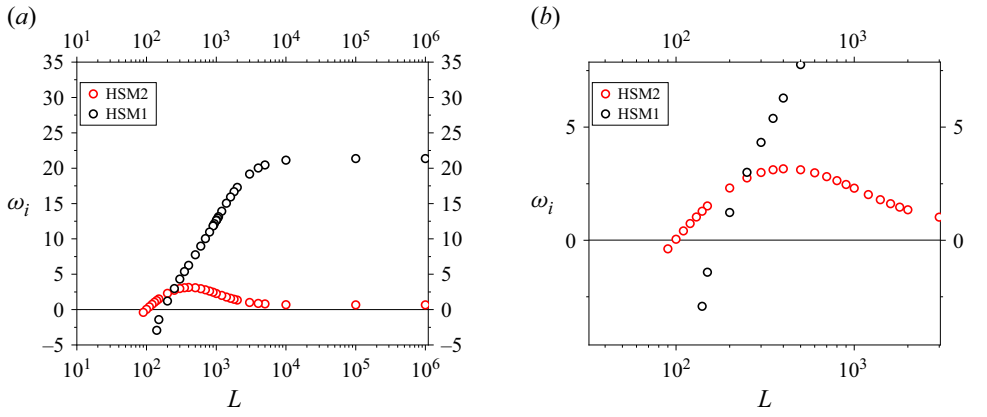


Figure 23. Variation of ω_i with L for the hoop-stress modes (HSM1 and HSM2) in Dean flow of a FENE-P fluid for $\epsilon = 0.1$, $\alpha = 7$, $n = 2$, $Re = 0$, $Wi = 130$ and $\beta = 0.98$: (*a*) for $10 < L < 10^6$ and (*b*) zoomed-in view of panel (*a*) highlighting the cross-over from HSM1 to HSM2.

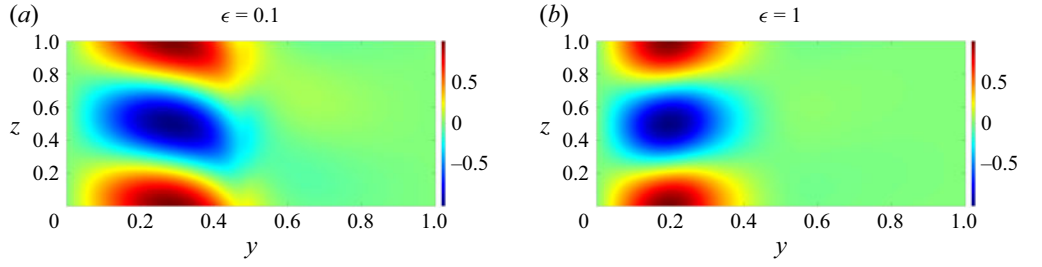


Figure 24. Structure of the Dean flow hoop-stress mode (HSM2) for a FENE-P fluid, characterised via contours of the azimuthal velocity perturbation, $|\tilde{v}_\theta|$, in the $r-z$ plane; $\beta = 0.98$, $L = 100$, $Wi = 400$, $n = 1$, $\alpha = 7$. In contrast to the centre-mode eigenfunction, which is localised near the velocity maximum, the HSM2 mode is localised near the inner wall.

Rather intriguingly, decreasing L has an initial destabilising effect on HSM2, although an ultimately stabilising one. This is evident from figure 23, which shows the growth rate (ω_i) variation with L for both HSM1 and HSM2 (for $n = 2$), with figure 23(*b*) presenting a magnified view of the interval $50 < L < 10^3$. The non-monotonic variation for HSM2 leads to HSM1 being the critical mode for $L > 200$ and HSM2 being critical for $L < 200$; for $L = 100$, HSM2 is the only unstable mode in the spectrum. An identical scenario prevails for $n = 1$ (not shown).

The aforementioned destabilising influence of finite extensibility on HSM2 is reminiscent of its effect on the centre mode in channel flow (Buza *et al.* 2022*b*; Khalid *et al.* 2025), and in Dean flow (as discussed in § 4.2). However, HSM2 is not a centre mode and has more in common with HSM1, as evident from the $r-z$ plane eigenfunction contours depicted in figures 24 and 25, and that are based on the amplitude of the azimuthal velocity perturbation; the choice of plane is on account of the primarily axisymmetric character of the HSMs. The only difference between the two HSMs is the region of localisation – the HSM2 (HSM1) eigenfunctions are localised near the inner (outer) radius. It is worth contrasting the structures in figures 24 and 25 with the CM arrowhead structures

https://doi.org/10.1017/jfm.2026.12002 Published online by Cambridge University Press

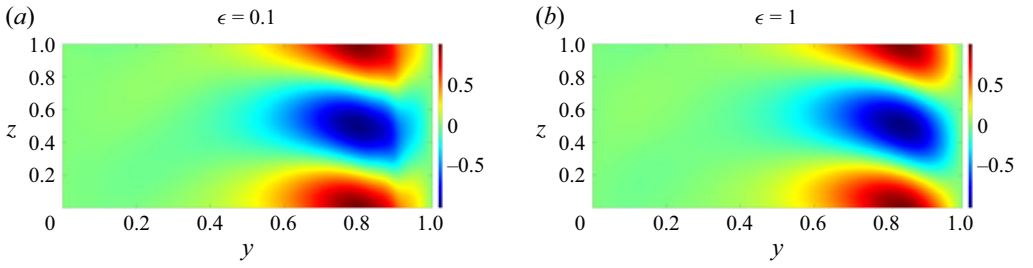


Figure 25. Structure of the Dean flow hoop-stress mode (HSM1) for a FENE-P fluid, characterised via contours of the azimuthal velocity perturbation, $|\tilde{v}_\theta|$, in the $r-z$ plane. In contrast to the centre-mode eigenfunction, which is localised near the velocity maximum, the HSM1 mode is localised near the outer wall.

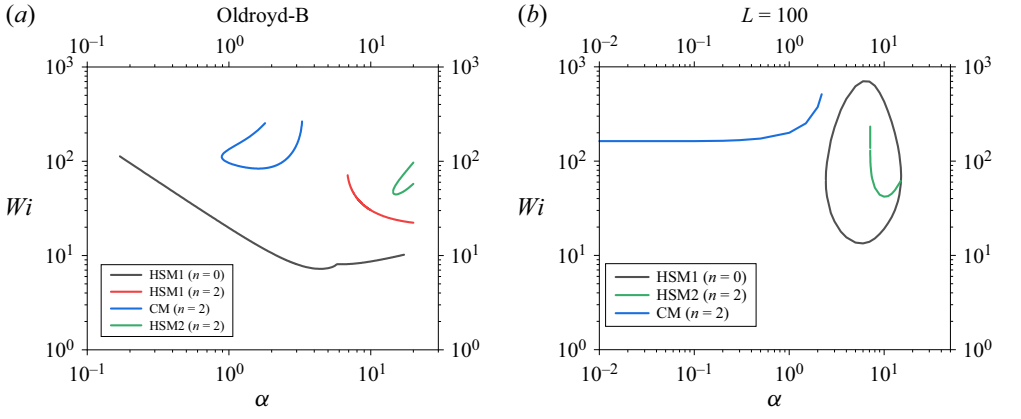


Figure 26. Neutral curves for CM and non-axisymmetric HSM2 for the (*a*) Oldroyd-B and (*b*) FENE-P ($L = 100$) models. Data for $n = 2$, $Re = 0$, $\epsilon = 1$, $\beta = 0.98$. The results for axisymmetric HSM1 are shown for reference.

shown earlier in figure 12. This contrast is further demonstrated in Appendix D, which compares eigenfunctions of the different field variables for HSM1, HSM2 and CM.

For the FENE-P case, the destabilising influence of finite extensibility on both CM and HSM2 might lead one to anticipate that these two modes might be connected in some regions of the parameter space. Figure 26 shows that this is not the case. This figure shows the neutral curves for HSM2 and CM, in the Wi–α plane, for both Oldroyd-B and FENE-P ($L = 100$) fluids, for $\epsilon = 1$. For the Oldroyd-B fluid, while the CM is stable for $\alpha = 0$ (when $\beta = 0.98$), it is destabilised by a non-zero α. In addition, there are neutral curves related to HSM1 and HSM2 (the HSM1 neutral curve for $n = 2$ is not shown). The critical Wi for the $n = 2$ mode in the FENE-P ($L = 100$) model is significantly higher than that for the Oldroyd-B case, due to the stabilising influence of finite extensibility. The unstable region for HSM2 (with $n = 2$) is completely disconnected from the CM, both for Oldroyd-B and FENE-P fluids. As α is increased for a fixed Wi (in figure 26), we find that the CM becomes stable and eventually merges into the CS, a trend that is reminiscent of the CM in rectilinear channel and pipe flows (Chaudhary *et al.* 2021; Khalid *et al.* 2021*a*). Similarly, when we tracked HSM2 for a Wi from the unstable region, the ω_r for this mode is such that it is beyond the CS range and, hence, this mode circumvents the CS and eventually ends up below it, without crossing the same. This shows that the two modes (HSM2 and

https://doi.org/10.1017/jfm.2026.12002 Published online by Cambridge University Press

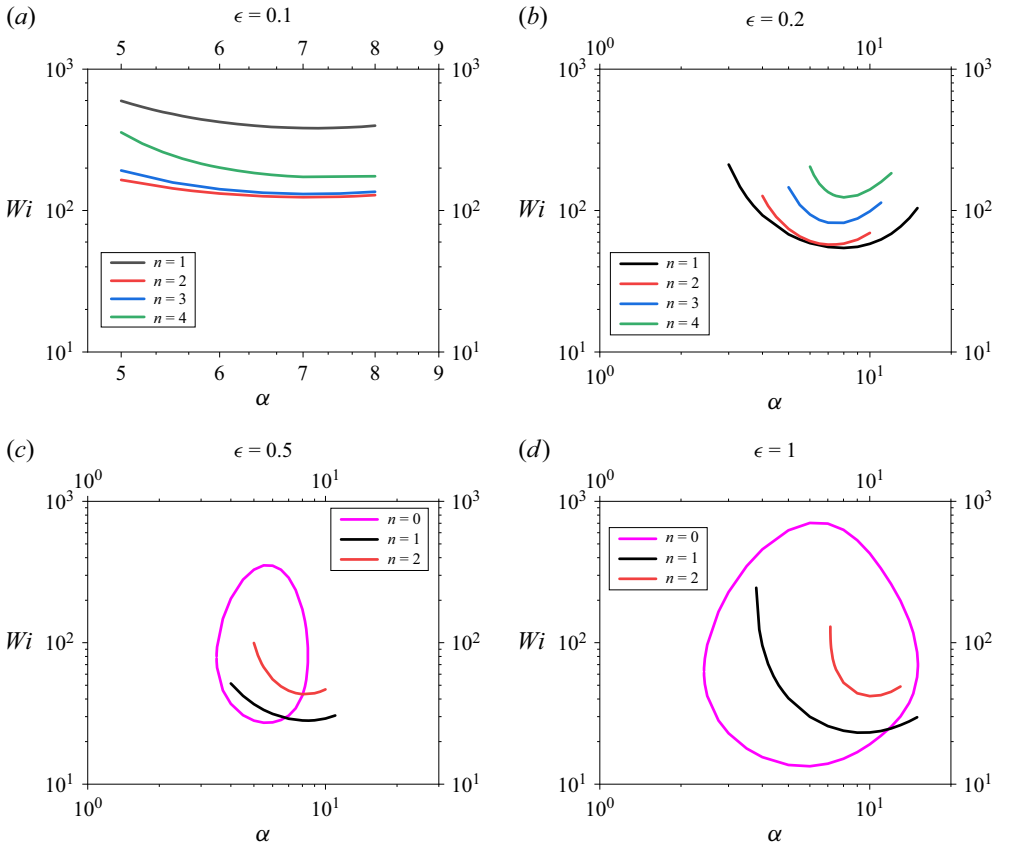


Figure 27. Neutral curves for HSM (1 and 2) at $Re = 0$, $\beta = 0.98$ and $L = 100$: (*a*) $\epsilon = 0.1$; (*b*) $\epsilon = 0.2$; (*c*) $\epsilon = 0.5$ and (*d*) $\epsilon = 1$. While the $n \neq 0$ modes (HSM2) are the most unstable for $\epsilon = 0.1$ and 0.2, and remain unstable even for $\epsilon = 0.5$ and 1, the $n = 0$ mode (HSM1) becomes critical at $\epsilon = 0.5$ and 1.

CM) do not continue to each other, as α is varied for a fixed Wi. While the discussion here pertains to HSM2 and CM, it is relevant to emphasise that for the larger gap-width ratio of $\epsilon = 1$, HSM1 (with $n = 0$) is the most critical for both Oldroyd-B and FENE-P models.

As seen in figure18, for the Oldroyd-B case, the axisymmetric HSM1 is the most unstable for any ϵ. However, the trend is very different for the FENE-P case, being sensitive to the choice of ϵ and L. For $L \sim 100$, the nature of the most unstable mode (*viz.*, axisymmetric versus non-axisymmetric HSM2) depends on ϵ, as shown in figure 27. In the narrow-gap regime ($\epsilon = 0.01-0.2$), the axisymmetric modes (both HSM1 and HSM2) remain stable for $L = 100$, while a non-axisymmetric HSM2 becomes critical. Specifically, at $\epsilon = 0.1$, $n = 2$ is the critical mode (HSM2), whereas at $\epsilon = 0.2$, $n = 1$ emerges as the critical mode (HSM2). In contrast, for the larger values $\epsilon = 0.5$ and 1, the axisymmetric mode (HSM1) becomes critical. Notably, the range of ϵ between 0.1 and 0.3 corresponds to gap widths used in the Taylor–Dean experiments of Joo & Shaqfeh (1994), although the serpentine channel experiments of Groisman & Steinberg (2001, 2004) used a higher ϵ (= 1); we return to the issue of the dominant mode in experiments in § 6.

For the Oldroyd-B model, Wi_c was seen to scale as $\epsilon^{-1/2}$ for $\epsilon \ll 1$. In contrast, and as already demonstrated in figure 20 and also in figure 27, one expects the HSM instability to be fully suppressed in the limit $\epsilon \to 0$ for any finite L. This is illustrated in figure 28(*a*),

https://doi.org/10.1017/jfm.2026.12002 Published online by Cambridge University Press

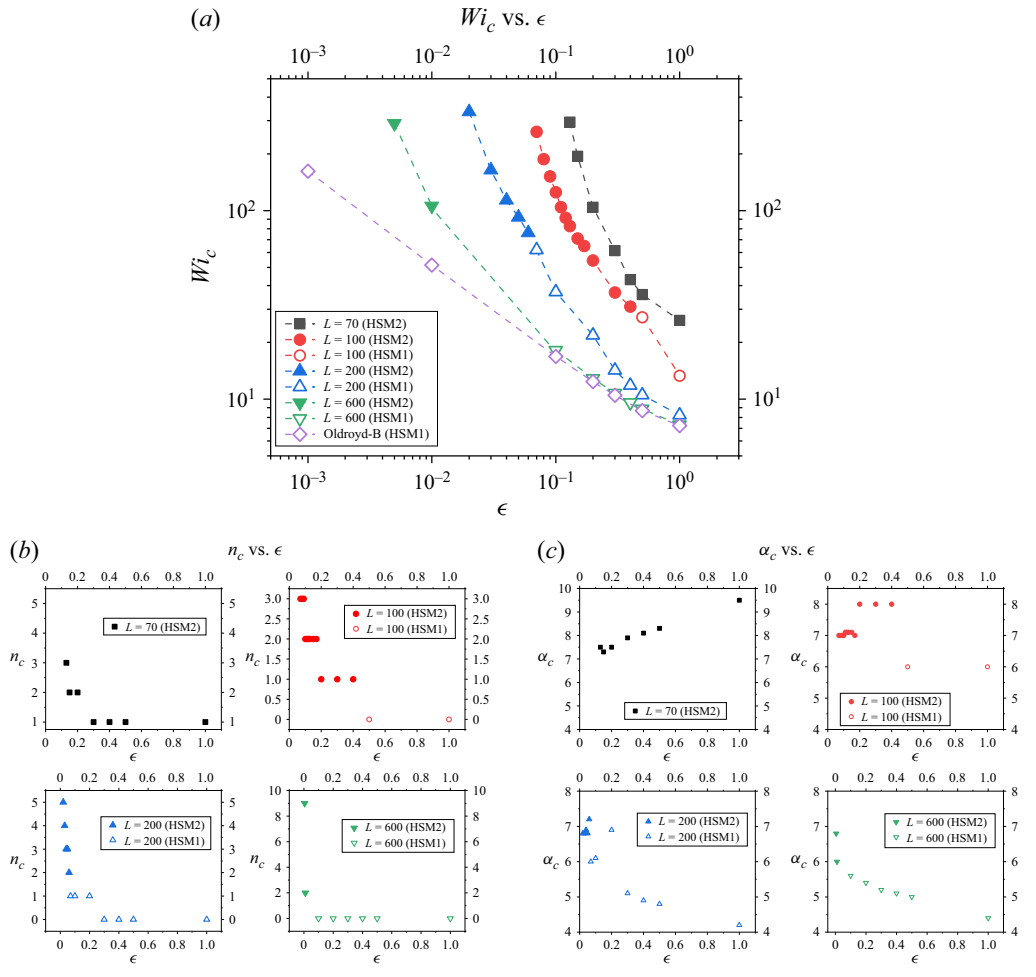


Figure 28. (*a*) Wi_c versus ϵ for HSM (1 and 2) in Dean flow at different L illustrating the stabilising influence of finite extensibility. Here, filled symbols of a given shape denote HSM2 and the corresponding open ones denote HSM1; different symbol shapes corresponds to different L. Corresponding (*b*) n_c versus ϵ and (*c*) n_c versus α_c. Data for $Re = 0$ and $\beta = 0.98$.

where Wi_c is seen to diverge faster than $\epsilon^{-1/2}$ for all finite L. The data points in figure 28(*a*) for Wi_c (at different ϵ or L) could correspond to either HSM1 ($n = 0$) or HSM1 ($n \neq 0$) or HSM2 ($n \neq 0$). Importantly, as L is decreased to realistic values of $O(100)$, HSM1 is fully suppressed, with a suggestion of the threshold diverging at a finite ϵ. This is in qualitative agreement with what one obtains at a scaling level by incorporating shear thinning in the Pakdel–McKinley criterion (see figure 15 of Castillo Sánchez *et al.* 2022). Figure 28(*b*) shows the critical azimuthal wavenumber n_c as a function of ϵ for different L; the notation used is similar to figure 28(*a*), in that open symbols pertain to HSM1, while filled symbols to HSM2. While in the Oldroyd-B limit, $n = 0$ remains critical for all ϵ, the critical azimuthal wavenumber for finite L changes with ϵ and there does not appear to be a simple trend. Figure 28(*c*) shows the corresponding critical axial wavenumber α_c. The abrupt variation of α_c with ϵ in this figure is on account of the transition from HSM1 to HSM2, and also due to changes in n_c.

https://doi.org/10.1017/jfm.2026.12002 Published online by Cambridge University Press

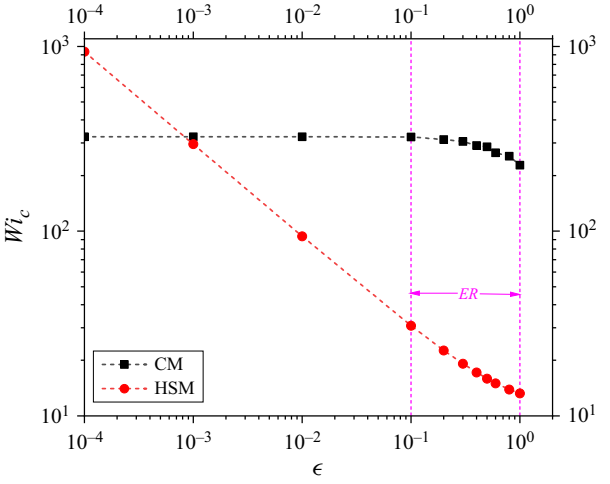


Figure 29. For the Oldroyd-B fluid, the CM becomes the critical mode only for $\epsilon < 10^{-3}$; for $\epsilon > 10^{-3}$, HSM is more unstable. Data showing the variation of Wi_c with ϵ for $Re = 0$ and $\beta = 0.994$. The range indicated by 'ER' denotes the ϵ typically used in experiments involving Taylor–Couette and Taylor–Dean configurations.

6. Discussion and conclusions

Elastic instabilities in the absence of fluid inertia have traditionally been associated with curvilinear shear flows (Pakdel & McKinley 1996), driven by hoop stresses induced by streamline curvature. Recently, Khalid *et al.* (2021*b*) identified a novel centre-mode (CM) elastic instability in rectilinear viscoelastic channel flow, driven by a mechanism that is not reliant on streamline curvature, and analogues of which have subsequently been found in other rectilinear shearing flows (Priyadarshi *et al.* 2023; Yadav *et al.* 2024; Lewy & Kerswell 2025). In this study, for the first time, we have shown the presence of both hoop-stress- (HSM) and centre-mode (CM) instabilities in the same shearing flow, the Dean flow configuration, using both Oldroyd-B and FENE-P models. While Dean flow approaches plane Poiseuille flow in the narrow-gap limit (with $\epsilon \to 0$), thence guaranteeing the presence of a CM instability in this limit, as argued later, the CM turns out to be the most unstable mode for realistic values of $L \sim 100$ in the FENE-P model even for experimentally relevant ϵ ($\approx 0.1 - 0.3$). Thus, the present study demonstrates the importance of two qualitatively distinct elastic instabilities in the same curvilinear flow configuration, and thence, the possibility of two different routes to an eventual (elastic) turbulent regime.

It is useful to compare the critical Wi_c for the previous two modes to determine which one is more critical, and how the criticality is influenced by ϵ and L. Owing to the CM instability existing only in the dilute limit, in the inertialess regime, the ensuing discussion applies for $\beta > 0.95$; although, as discussed later, nonlinear stability considerations will likely render the CM significant over a wider range of β (Buza *et al.* 2022*a*). Figure 29 shows that, within the Oldroyd-B framework ($L \to \infty$), the axisymmetric HSM is the more unstable mode across all experimentally reasonable gap width ratios, *viz.*, $\epsilon \geqslant 0.1$. As a result, although the range of β over which the CM is unstable is slightly larger than that for pressure-driven channel flow, this is of little consequence within the Oldroyd-B framework. However, as we discuss in the following subsection, the scenario is reversed for $L \simeq 100$ in the FENE-P model, with the CM being the more unstable mode for experimentally relevant ϵ.

https://doi.org/10.1017/jfm.2026.12002 Published online by Cambridge University Press

Reference	Polymer	Molecular weight ($g\,mol^{-1}$)	Characteristic ratio	$L=\sqrt{N_K}$
McKinley *et al.* (1991)	Polyisobutylene	2×10^6	7	72
White & Muller (2000)	Polyisobutylene	5×10^6	7	113
Joo & Shaqfeh (1994)	Polyisobutylene	6×10^6	7	120
Choueiri *et al.* (2021)	Polyacrylamide	5×10^6	8.5	91
Neelamegam *et al.* (2013)	—	—	—	—
Varshney & Steinberg (2018)	Polyacrylamide	18×10^6	8.5	172
Lu & Hof (2026)	—	—	—	—
Chandra *et al.* (2018)	Polyethylene oxide	5×10^6	4.3	162
Rothstein & McKinley (2001)	Polystyrene	6.5×10^6	10	80
Rothstein & McKinley (2001)	Polystyrene	20×10^6	10	140

Table 4. Polymers used in prior experimental studies probing elastic and elastoinertial instabilities in both rectilinear and curvilinear geometries, along with the corresponding FENE-P extensibility parameter L.

6.1. *Connection to experiments*

We first estimate the extensibility parameter L for polymers commonly used to observe purely elastic instabilities in curvilinear flows and elastoinertial instabilities in pipe flow. To this end, it is useful to model a polymer molecule as an effectively freely jointed chain of N_K Kuhn segments each of length l_K (the Kuhn length). The extensibility parameter L is defined as the ratio of the fully extended length of the polymer to its root mean square length at equilibrium, yielding $L=(l_K N_K)/(l_K\sqrt{N_K})=\sqrt{N_K}$. If N_p be the degree of polymerisation (i.e. the number of monomer repeat units in the polymer), $N_K=N_p/C_\infty$, where the characteristic ratio C_∞ is the number of monomers per Kuhn segment; the latter has been documented for synthetic polymers (Rubinstein & Colby 2014) and depends on the monomer flexibility.

Table 4 shows that $L\approx70-170$ for the polymers is usually used in experiments on elastic instabilities. Now, our results for Dean flow show that finite extensibility completely suppresses the hoop-stress instability below a critical, β-dependent, L_{min}. For the very dilute case of $\beta=0.97$ (shown in figure 20), $L_{min}\approx175$ (for $\epsilon=0.1$), while for $\beta=0.8$, $L_{min}\approx50$ (data not shown). In light of these estimates, it appears that the experiments carried out thus far do not allow us to definitively infer signatures of finite extensibility on the HSM. For the Taylor–Dean experiments of Joo & Shaqfeh (1994), for instance, the polymer is polyisobutylene ($M_w=4$–$6\times10^6\,g\,mol^{-1}$) dissolved in a viscous Newtonian solvent (oligomeric polybutene), yielding $L\approx100-120$ with $\beta=0.8$ – for these parameters, our FENE-P predictions (for the Dean flow configuration) show that the threshold Wi is only 33 % more than that obtained using the Oldroyd-B model. There is, however, a rapid stabilisation as L is decreased from 100 to 50, with the instability being fully suppressed for $L<50$. Since L is proportional to the square root of the polymer molecular weight, this translates to stabilisation for molecular weights $\lesssim10^6\,g\,mol^{-1}$. Alternatively, if the Joo & Shaqfeh (1994) experiments were repeated for much more dilute solutions, with $\beta\approx0.97$, the instability would be suppressed even for the higher molecular weight polymers (with $L\sim100-120$) originally used. To summarise, the experiments carried out thus far in curvilinear geometries do not allow us to definitively infer signatures of finite extensibility on the HSM.

Turning our attention next to the centre mode, figure 30 shows the HSM and CM thresholds as a function of ϵ, for different L, at $\beta=0.98$. To a good approximation, Wi_c

https://doi.org/10.1017/jfm.2026.12002 Published online by Cambridge University Press

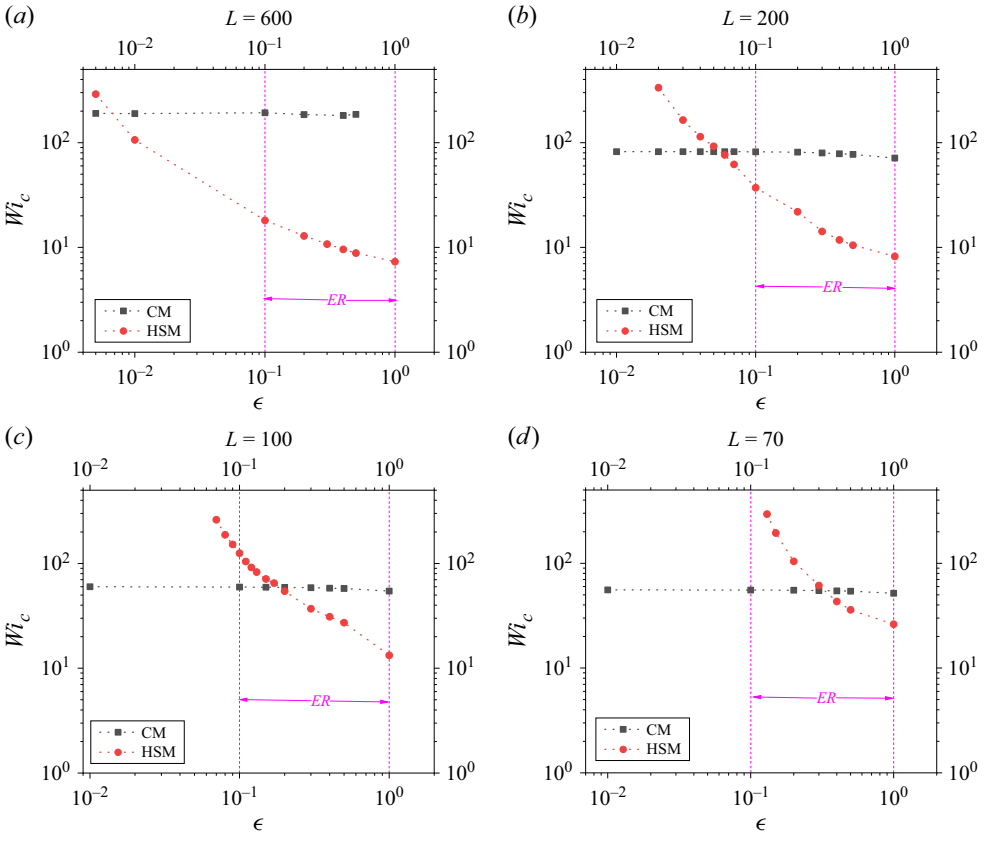


Figure 30. For Dean flow of FENE-P fluids, as L is decreased, the CM remains more critical compared with HSM at increasingly higher ϵ. Data showing Wi_c versus ϵ at $\beta = 0.98$, $Re = 0$. The range indicated by 'ER' denotes the ϵ typically used in experiments. (*a*) $L = 600$; (*b*) $L = 200$; (*c*) $L = 100$ and (*d*) $L = 70$.

for the CM is obtained by setting $\alpha = 0$, implying that the critical mode in such cases is nearly two-dimensional. Figure 30(*a*) suggests that the CM instability is not relevant for $L = 600$; for the polyacrylamide solutions routinely used in experiments, $L \sim 600$ would imply a molecular weight of $\gtrsim 10^8\,\mathrm{g\,mol^{-1}}$. However, as evident from table 4, the highest molecular weight used hitherto in experiments probing elastic instabilities is $1.8 \times 10^7\,\mathrm{g\,mol^{-1}}$ (e.g. see Neelamegam *et al.* 2013). The CM starts to become relevant for $L = 200$, and is certainly the only one present for $\epsilon \leqslant 0.1$ and $L < 100$ (as appropriate for the polyacrylamide solutions used by Choueiri *et al.* 2021, with a molecular weight of $5 \times 10^6\,\mathrm{g\,mol^{-1}}$). For the latter range of L, as shown in figure 30(*c*), the CM is the most critical mode for $\epsilon = 0.1$–0.3 corresponding to the Taylor–Dean experiments of Joo & Shaqfeh (1994) mentioned earlier; although the HSM will likely be dominant in the serpentine channel experiments of Groisman & Steinberg (2004) with $\epsilon = 1$. It is worth adding that, although the focus of this work has been on Dean flow, most of the results are expected to carry over to the Taylor–Dean geometry, in light of the demonstration of the continued existence of a CM in Couette–Poiseuille flows (the rectilinear analogues of the Taylor–Dean family; see Yadav *et al.* 2024). Thus, in experiments involving the Dean or Taylor–Dean configurations, for realistic values of ϵ and L, the CM instability will be relevant for sufficiently dilute solutions such that $\beta > 0.95$, while the HSM is expected to be the dominant mode for $\beta < 0.95$; at least within a linear stability framework. Crucially,

https://doi.org/10.1017/jfm.2026.12002 Published online by Cambridge University Press

the demonstration by Buza *et al.* (2022*a*), of finite-amplitude travelling waves borne out of the elastic CM instability in channel flow being strongly subcritical, and existing at $Wi \lesssim 50$ and for β down to 0.7, suggests that the CM could be relevant even in parameter regimes where it is linearly stable in Dean flow.

6.2. *Transition scenarios in elastic Dean flow*

In light of the recent experiments of Lu & Hof (2026) briefly alluded to in § 1 that have identified a secondary hoop-stress-mediated transition in weakly curved pipes, it is tempting to speculate on subsequent transitions in regimes where the CM is the primary instability. For sufficiently small ϵ, when this is the case, one expects the growing CM eigenfunction to augment base-state streamline curvature and the resulting perturbed flow to therefore be susceptible to a secondary instability, driven by a hoop-stress mechanism involving spanwise perturbations, likely culminating in an eventual state of elastic turbulence. Such a scenario has indeed been conjectured by Lu & Hof (2026). The authors find a CM instability in the limit of small curvature, consistent with the observations of Choueiri *et al.* (2021) for straight pipes. The amplitude of velocity fluctuations at onset, as measured by particle image velocimetry, peaks close to the pipe centreline, and the fluctuation field exhibits the 'arrowhead' structure characteristic of the centre mode. The threshold Wi remains insensitive to increasing curvature until $d/R \approx 0.06$, beyond which there is a cross-over to a hoop-stress-driven mode, characterised by a threshold Wi that decreases with further increase in curvature; the decrease being consistent with the Pakdel–McKinley criterion as argued in § 5. The hoop-stress-driven transition is characterised by stronger velocity fluctuations, with an amplitude profile that peaks close to the walls; the latter resembles the HSM(1,2) velocity eigenfunctions (figures 24 and 25) which are localised near the boundaries. The overall picture of the primary transition is thus consistent with the CM-HSM cross-over in figure 30, albeit with a possible difference in the viscosity ratio.

The above-mentioned secondary instability mechanism points to a novel nonlinear pathway to the elastic turbulent state, one that differs from what had been proposed earlier by Bertola *et al.* (2003), Meulenbroek *et al.* (2003), Morozov & van Saarloos (2005*b*), Morozov & Saarloos (2007), Pan *et al.* (2013) and Morozov & van Saarloos (2019). Although this latter mechanism has also been attributed to the curvature of perturbed streamlines, it operates in the absence of a linear instability (the aforementioned references were mostly prior to the discovery of the CM instability for pipe and plane Poiseuille flows) and entails the nonlinear interaction of a weakly stable streamwise varying mode with itself, the self-interaction leading to a 'bifurcation from infinity' scenario, which has been analysed within a Stuart–Landau framework by the authors. Thus, there is no direct connection of this earlier route with the hoop-stress-based mechanism known to trigger the growth of spanwise varying perturbations in the canonical curvilinear shearing flow configurations. Although the effort of Morozov & van Saarloos (2005*b*) did account for spanwise variations, the Weissenberg number corresponding to the saddle-node bifurcation was the lowest for the two-dimensional (2-D) case devoid of spanwise variations.

The larger amplitude near-wall structures, associated with the onset of the secondary hoop-stress-driven instability in the aforementioned experiments, eventually manifest as the near-wall sheet-like structures (with strongly stretched polymers) of elastoinertial or elastic turbulence (Lu & Hof 2026). Such a centre-to-wall-mode transition was, in fact, first seen in the straight-pipe experiments of Choueiri *et al.* (2021). At the time, the wall mode was interpreted in terms of nonlinear viscoelastic Tollmien–Schlichting (TS)

https://doi.org/10.1017/jfm.2026.12002 Published online by Cambridge University Press

waves whose existence and relevance (in terms of constituting an invariant skeleton for the phase space dynamics), in the pertinent range of parameters, has been argued for by Shekar *et al.* (2019, 2020, 2021); also see Datta *et al.* (2022). What is interesting about the recent experiments of Lu & Hof (2026) is the demonstration of the secondary hoop-stress mode continuing down to zero curvature. In other words, a secondary transition occurs beyond a threshold Wi even in straight pipes (this Wi, of course, being greater than that corresponding to the primary CM), a result that links the aforementioned wall mode to the zero-curvature limiting form of a hoop-stress mode, rather than a viscoelastic TS wave. The above-mentioned continuation is somewhat reminiscent of the continuation of the secondary wavy-vortex mode in the Taylor–Couette geometry to the plane Couette flow limit, by Nagata (1990), which served as one of the earliest demonstrations of non-trivial 3-D flow fields satisfying the Navier–Stokes equations. Such solutions, now termed the exact coherent structures, are known to form the scaffold for transitional dynamics in the Newtonian case.

It must, however, be added that there are non-trivial differences between the experimental curved-pipe configuration and the Dean flow configuration examined here; differences that potentially complicate the above interpretation. To appreciate this, it is instructive to think of the curved pipe (circular cross-section with unit aspect ratio), and the curved channel (infinite aspect ratio), as limiting members of a family of curved pipes with elliptical cross-sections, parametrized by the ellipse aspect ratio. While the transition from the primary azimuthal flow to a three-dimensional flow field does occur as an instability (a perfect pitchfork bifurcation from the base-state unidirectional shear flow) in the limit of infinite aspect ratio, this is no longer true for finite-aspect-ratio cross-sections. In the context of Newtonian fluids, this was shown first by Benjamin (1978) for the Taylor–Couette geometry wherein an inter-cylinder gap with a finite aspect ratio leads to secondary circulations at any finite Taylor number; the analogous existence of inertial Dean vortices has also been demonstrated (Berger *et al.* 1983). Accordingly, for the previous curved-pipe in the experiments of Lu & Hof (2026), one expects a secondary circulation to exist at any finite Wi (Bowen *et al.* 1991; Fan *et al.* 2001; Poole *et al.* 2013); this, as opposed to onset via a hoop-stress-driven bifurcation at a threshold Wi. The absence of a sensible threshold is especially because the circular cross-section represents a finite departure (when measured in terms of the parameter that characterises the aforementioned elliptic-pipe family) from the curved-channel configuration. Thus, the transition scenario proposed appears more appropriate for the curved channel geometry examined here than for the curved pipe used in the experiments. Notwithstanding this caveat, however, the experiments of Lu & Hof (2026) are broadly consistent with our predictions of a CM–HSM cross-over with increasing ϵ.

Finally, there is a third instability mechanism, referred to as the polymer diffusive instability ('PDI'; see Beneitez *et al.* 2023; Couchman *et al.* 2024; Lewy & Kerswell 2024), which is present even in rectilinear shearing flows, but arises only when the constitutive equation is augmented with a diffusion term. The instability is in the form of wall-localised travelling waves, with the wavelength of the most unstable mode being independent of the channel width, scaling as the boundary layer thickness $\sqrt{D\lambda}$; D here being the translational diffusivity of the polymer molecule and λ being the relaxation time. For dilute solutions, the polymer diffusivity scales as $D \sim R_g^2/\lambda$, implying that the unstable wavelength is comparable to the polymer radius of gyration R_g, thereby raising questions on the feasibility of observing these structures in experiments with real polymer solutions. Indeed, the PDI has been shown to be sensitive to details of the constitutive model used – in the Giesekus model, for instance, the PDI is rapidly suppressed even for very small values of the parameter characterising anisotropic drag

https://doi.org/10.1017/jfm.2026.12002 Published online by Cambridge University Press

(Pandey & Shankar 2025). For FENE-P fluids, the PDI is likely present as a numerical instability in DNS studies that employ artificially high diffusivities (resulting in the wavelength of the unstable mode becoming comparable to channel width) and structures arising from the PDI are of relevance in such studies, as shown by Beneitez *et al.* (2025) for 2-D Taylor–Couette flow.

Declaration of interests. The authors report no conflict of interest.

Author contributions. V.S and G.S proposed and designed the research. P.S.D.S.P.T and V.S derived the equations and developed the code. P.S.D.S.P.T carried out the simulations. All authors contributed equally to analysing data, reaching conclusions and writing the paper.

Appendix A. Linearised stability equations for the Oldroyd-B model

The linearised continuity, momentum and constitutive equations for the Oldroyd-B model are given in this appendix. Here, and in what follows, $D \equiv \mathrm{d}/\mathrm{d}y$. Continuity equation:

$$\frac{\mathrm{d}\tilde{v}_r}{\mathrm{d}y} + \frac{\epsilon}{1+\epsilon y}\tilde{v}_r + \frac{in\epsilon}{1+\epsilon y}\tilde{v}_\theta + i\alpha\tilde{v}_z = 0, \tag{A1}$$

r-momentum equation:

$$G\tilde{v}_r + G_1\tilde{v}_\theta = -D\tilde{p} + \beta M\tilde{v}_r + M_1\tilde{\tau}_{rr} + M_2\tilde{\tau}_{r\theta} + i\alpha\tilde{\tau}_{rz} - \left(\frac{\epsilon}{1+\epsilon y}\right)\tilde{\tau}_{\theta\theta}, \tag{A2}$$

θ-momentum equation:

$$G\tilde{v}_\theta + G_2\tilde{v}_r = -M_2\tilde{p} + \beta M\tilde{v}_\theta + \left(M_1 + \frac{\epsilon}{1+\epsilon y}\right)\tilde{\tau}_{r\theta} + M_2\tilde{\tau}_{\theta\theta} + i\alpha\tilde{\tau}_{\theta z}, \tag{A3}$$

z-momentum equation:

$$G\tilde{v}_z = -i\alpha\tilde{p} + \beta M\tilde{v}_z + M_1\tilde{\tau}_{rz} + M_2\tilde{\tau}_{\theta z} + i\alpha\tilde{\tau}_{zz}, \tag{A4}$$

τ_{rr} equation:

$$\zeta\tilde{\tau}_{rr} = 2(1-\beta)\frac{\mathrm{d}\tilde{v}_r}{\mathrm{d}y} + 2WiM_2\tilde{v}_r, \tag{A5}$$

$\tau_{r\theta}$ equation:

$$\zeta\tilde{\tau}_{r\theta} = Wi\left(U' - \frac{\epsilon}{1+\epsilon y}U\right)\tilde{\tau}_{rr} + Pv_r + \left[(1-\beta)\left(D - \frac{\epsilon}{1+\epsilon y}\right) + M_2\overline{\tau}_{r\theta}\right]\tilde{v}_\theta, \tag{A6}$$

τ_{rz} equation:

$$\zeta\tilde{\tau}_{rz} = \left[(1-\beta)D + WiM_2\overline{\tau}_{r\theta}\right]\tilde{v}_z + (1-\beta)i\alpha\tilde{v}_r, \tag{A7}$$

$\tau_{\theta\theta}$ equation:

$$\zeta\tilde{\tau}_{\theta\theta} = 2Wi\left(U' - \frac{\epsilon}{1+\epsilon y}U\right)\tilde{\tau}_{r\theta} + \left[2(1-\beta)\frac{\epsilon}{1+\epsilon y} - Wi\left(\overline{\tau}'_{\theta\theta} - \frac{2\epsilon}{1+\epsilon y}\overline{\tau}_{\theta\theta}\right)\right]\tilde{v}_r + F\tilde{v}_\theta, \tag{A8}$$

$\tau_{\theta z}$ equation:

$$\zeta\tilde{\tau}_{\theta z} = Wi\left(U' - \frac{\epsilon}{1+\epsilon y}U\right)\tilde{\tau}_{rz} + E\tilde{v}_z + (1-\beta)i\alpha\tilde{v}_\theta, \tag{A9}$$

https://doi.org/10.1017/jfm.2026.12002 Published online by Cambridge University Press

τ_{zz} equation:

$$\zeta\tilde{\tau}_{zz} = 2(1-\beta)i\alpha\tilde{v}_z, \tag{A10}$$

where $\zeta = [1 - i\omega + Wi(in\epsilon/1+\epsilon y)U]$

$$\begin{aligned}
G &= Re((in\epsilon/1+\epsilon y)U - (i\omega/Wi)) \\
M &= (D^2 + (\epsilon/1+\epsilon y)D - (\epsilon^2/(1+\epsilon y)^2) - (n^2\epsilon^2/(1+\epsilon y)^2) - \alpha^2) \\
M_1 &= (D + (\epsilon/1+\epsilon y)),\ M_2 = (in\epsilon/1+\epsilon y), \\
G_1 &= -2Re(\epsilon/1+\epsilon y) + \beta(2in\epsilon^2/(1+\epsilon y)^2) \\
G_2 &= Re(\epsilon/1+\epsilon y) - \beta(2in\epsilon^2/(1+\epsilon y)^2) + ReU' \\
E &= [Wi(\overline{\tau}_{r\theta}D + M_2\overline{\tau}_{\theta\theta}) + (1-\beta)M_2], \\
F &= [2Wi(\overline{\tau}_{r\theta}D + M_2\overline{\tau}_{\theta\theta} - (\epsilon/1+\epsilon y)\overline{\tau}_{r\theta}) + 2(1-\beta)M_2] \\
P &= [Wi(\overline{\tau}_{r\theta}D + M_2\overline{\tau}_{\theta\theta} + (\epsilon/1+\epsilon y)\overline{\tau}_{r\theta} - \overline{\tau}'_{r\theta}) + (1-\beta)M_2],
\end{aligned} \tag{A11}$$

Appendix B. Linearised stability equations for the FENE-P model

The linearised continuity, momentum, and constitutive equations for the FENE-P model are given in this appendix.

Continuity equation:

$$\left(D + \frac{\epsilon}{1+\epsilon y}\right)\tilde{v}_r + \frac{in\epsilon}{1+\epsilon y}\tilde{v}_\theta + i\alpha\tilde{v}_z = 0, \tag{B1}$$

r-momentum equation:

$$\begin{aligned}
Re\left(-\frac{i\omega}{Wi} + \frac{\overline{v}_\theta in\epsilon}{1+\epsilon y}\right)\tilde{v}_r - \frac{2Re\epsilon\overline{v}_\theta}{1+\epsilon y}\tilde{v}_\theta = &-\frac{\partial\tilde{p}}{\partial y} + \beta\left(\left(\frac{\partial^2}{\partial y^2} - \frac{\epsilon^2}{(1+\epsilon y)^2} + \frac{\epsilon}{1+\epsilon y}\frac{\partial}{\partial y}\right.\right. \\
&\left.\left. - \frac{n^2\epsilon^2}{(1+\epsilon y)^2} - \alpha^2\right)\tilde{v}_r - \frac{2\epsilon^2 in}{(1+\epsilon y)^2}\tilde{v}_\theta\right) \\
&+ (1-\beta)\left(\frac{\partial\tilde{\tau}_{rr}}{\partial y} + \frac{\epsilon}{1+\epsilon y}\tilde{\tau}_{rr} + \frac{in\epsilon}{1+\epsilon y}\tilde{\tau}_{\theta r}\right. \\
&\left. + i\alpha\tilde{\tau}_{zr} - \frac{\epsilon}{1+\epsilon y}\tilde{\tau}_{\theta\theta}\right),
\end{aligned} \tag{B2}$$

θ-momentum equation:

$$\begin{aligned}
Re\left(\frac{\partial\overline{v}_\theta}{\partial y} + \frac{\overline{v}_\theta\epsilon}{1+\epsilon y}\right)\tilde{v}_r + Re\left(\frac{\overline{v}_\theta in\epsilon}{1+\epsilon y} - \frac{i\omega}{Wi}\right)\tilde{v}_\theta = &-\frac{in\epsilon}{1+\epsilon y}\tilde{p} \\
&+ \beta\left(\left(\frac{\partial^2}{\partial y^2} - \frac{\epsilon^2}{(1+\epsilon y)^2} + \frac{\epsilon}{1+\epsilon y}\frac{\partial}{\partial y}\right.\right. \\
&\left.\left. - \frac{n^2\epsilon^2}{(1+\epsilon y)^2} - \alpha^2\right)\tilde{v}_\theta + \frac{2\epsilon^2 in}{(1+\epsilon y)^2}\tilde{v}_r\right) \\
&+ (1-\beta)\left(\frac{\partial\tilde{\tau}_{\theta r}}{\partial y} + \frac{\epsilon}{1+\epsilon y}\tilde{\tau}_{\theta r}\right. \\
&\left. + \frac{in\epsilon}{1+\epsilon y}\tilde{\tau}_{\theta\theta} + i\alpha\tilde{\tau}_{z\theta}\right),
\end{aligned} \tag{B3}$$

https://doi.org/10.1017/jfm.2026.12002 Published online by Cambridge University Press

z-momentum equation:

$$Re\left(-\frac{i\omega}{Wi}+\frac{\overline{v}_\theta in\epsilon}{1+\epsilon y}\right)\tilde{v}_z=-i\alpha\tilde{p}+\beta\left(\frac{\partial^2\tilde{v}_z}{\partial y^2}-\frac{\epsilon^2}{(1+\epsilon y)^2}\tilde{v}_z+\frac{\epsilon}{1+\epsilon y}\frac{\partial\tilde{v}_z}{\partial y}-\frac{n^2\epsilon^2}{(1+\epsilon y)^2}\tilde{v}_z-\alpha^2\tilde{v}_z\right)+(1-\beta)\left(\frac{\partial\tilde{\tau}_{rz}}{\partial y}+\frac{\epsilon}{1+\epsilon y}\tilde{\tau}_{rz}+\frac{in\epsilon}{1+\epsilon y}\tilde{\tau}_{\theta z}+i\alpha\tilde{\tau}_{zz}\right), \tag{B4}$$

C_{rr} equation:

$$\left(\overline{C}'_{rr}-2\overline{C}_{rr}D-\frac{2\overline{C}_{r\theta}in\epsilon}{1+\epsilon y}\right)\tilde{v}_r+\left(\frac{\overline{v}_\theta in\epsilon}{1+\epsilon y}-\frac{i\omega}{Wi}\right)\tilde{C}_{rr}=-\tilde{\tau}_{rr}, \tag{B5}$$

$C_{r\theta}$ equation:

$$\left(\overline{C}'_{r\theta}-\frac{in\epsilon}{1+\epsilon y}\overline{C}_{\theta\theta}\right)\tilde{v}_r+\left(\frac{\epsilon\overline{C}_{rr}}{1+\epsilon y}-\overline{C}_{rr}\frac{\partial}{\partial y}\right)\tilde{v}_\theta+i\alpha\overline{C}_{r\theta}\tilde{v}_z+\left(\frac{\overline{v}_\theta\epsilon}{1+\epsilon y}-\overline{v}'_\theta\right)\tilde{C}_{rr}+\left(\frac{\overline{v}_\theta\epsilon in}{1+\epsilon y}-\frac{i\omega}{Wi}\right)\tilde{C}_{r\theta}=-\tilde{\tau}_{r\theta}, \tag{B6}$$

C_{rz} equation:

$$-i\alpha\overline{C}_{zz}\tilde{v}_r-\left(\overline{C}_{rr}\frac{\partial}{\partial y}+\frac{\overline{C}_{r\theta}in\epsilon}{1+\epsilon y}\right)\tilde{v}_z+\left(\frac{\overline{v}_\theta in\epsilon}{1+\epsilon y}-\frac{i\omega}{Wi}\right)\tilde{C}_{rz}=-\tilde{\tau}_{rz}, \tag{B7}$$

$C_{\theta\theta}$ equation:

$$\left(\overline{C}'_{\theta\theta}-\frac{2\epsilon}{1+\epsilon y}\overline{C}_{\theta\theta}\right)\tilde{v}_r+\left(\frac{2\epsilon}{1+\epsilon y}\overline{C}_{r\theta}-\frac{2in\epsilon}{1+\epsilon y}\overline{C}_{\theta\theta}-2\overline{C}_{r\theta}\frac{\partial}{\partial y}\right)\tilde{v}_\theta+2\left(\frac{\epsilon}{1+\epsilon y}\overline{v}_\theta-\overline{v}'_\theta\right)\tilde{C}_{r\theta}+\left(\frac{\overline{v}_\theta in\epsilon}{1+\epsilon y}-\frac{i\omega}{Wi}\right)\tilde{C}_{\theta\theta}=-\tilde{\tau}_{\theta\theta}, \tag{B8}$$

$C_{\theta z}$ equation:

$$-i\alpha\overline{C}_{zz}\tilde{v}_\theta-\left(\overline{C}_{\theta r}\frac{\partial}{\partial y}+\frac{in\epsilon}{1+\epsilon y}\overline{C}_{\theta\theta}\right)\tilde{v}_z+\left(\frac{\epsilon}{1+\epsilon y}\overline{v}_\theta-\frac{\partial\overline{v}_\theta}{\partial y}\right)\tilde{C}_{rz}+\left(\frac{in\epsilon}{1+\epsilon y}\overline{v}_\theta-\frac{i\omega}{Wi}\right)\tilde{C}_{\theta z}=-\tilde{\tau}_{\theta z}, \tag{B9}$$

C_{zz} equation:

$$\frac{\partial\overline{C}_{zz}}{\partial y}\tilde{v}_r-2i\alpha\overline{C}_{zz}\tilde{v}_z+\left(\frac{in\epsilon}{1+\epsilon y}\overline{v}_\theta-\frac{i\omega}{Wi}\right)\tilde{C}_{zz}=-\tilde{\tau}_{zz}. \tag{B10}$$

Appendix C. Eigenspectra for viscoelastic Dean flow

In figure 31, we present the axisymmetric eigenspectra for the Oldroyd-B fluid at different axial wavenumbers α for a fixed Wi. As mentioned in § 3.1, for $\beta=0.98$, the two point CS are nearly overlapping (with $\omega_i=-1$) in this figure. Twelve branches of discrete modes are seen to spread out from the (point) CS and $\omega_r\neq0$ for these modes. At lower α, we also find two least stable modes which are stationary (i.e. $\omega_r=0$), with the mode having the higher growth rate turning unstable for $\alpha=7$. As α is increased further, the aforementioned stationary modes coalesce in a bifurcation, giving rise to symmetrically

https://doi.org/10.1017/jfm.2026.12002 Published online by Cambridge University Press

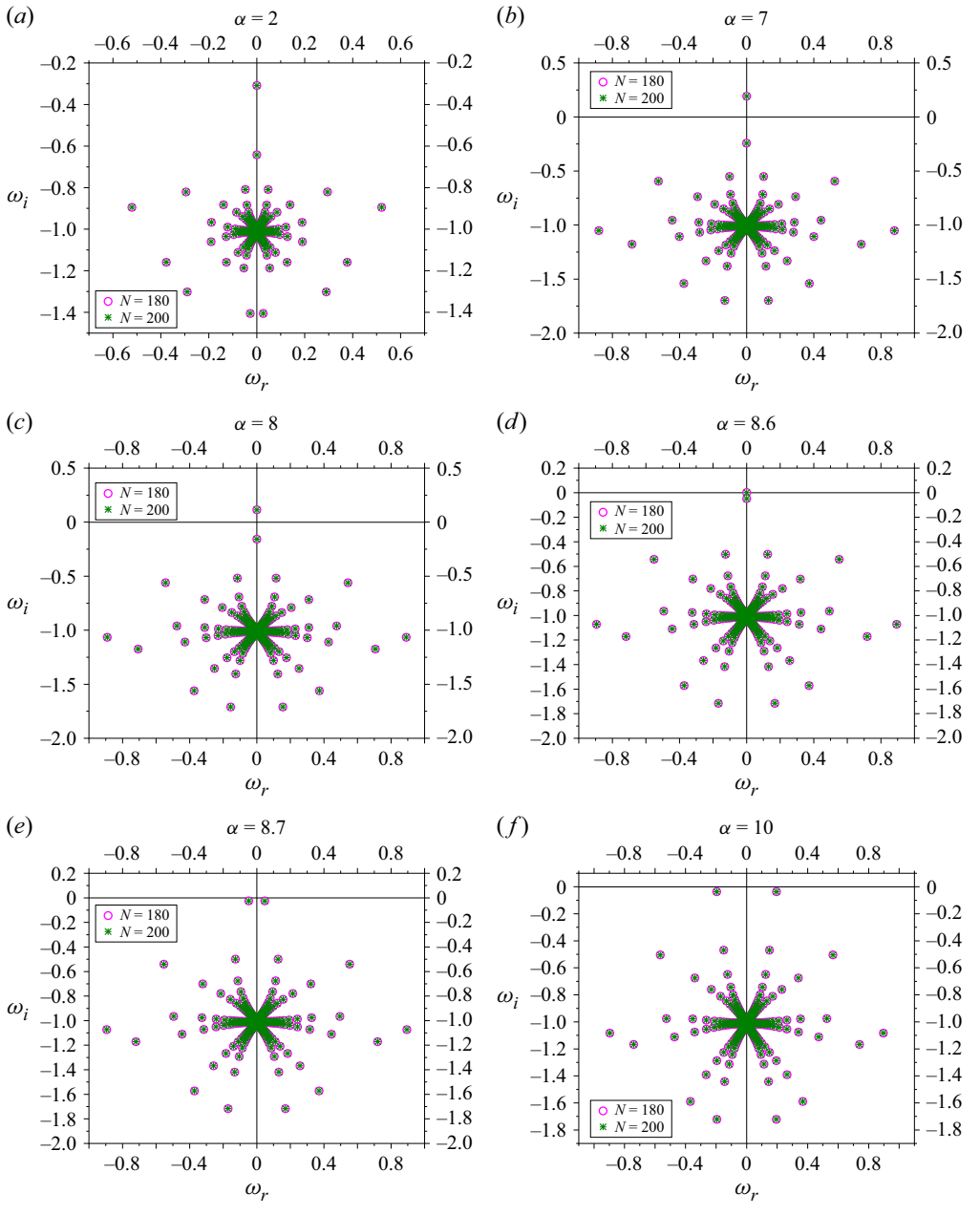


Figure 31. Axisymmetric ($n = 0$) eigenspectra for different α at $Wi = 20$, $\epsilon = 0.1$, $\beta = 0.98$ for Dean flow of an Oldroyd-B fluid demonstrating the bifurcation of stationary HSM into two propagating modes: (*a*) $\alpha = 2$; (*b*) $\alpha = 7$; (*c*) $\alpha = 8$; (*d*) $\alpha = 8.6$; (*e*) $\alpha = 8.7$ and (*f*) $\alpha = 10$.

placed propagating modes (of the form $\pm\omega_r + \omega_i$), with no stationary discrete modes present in the spectrum.

This bifurcation can happen either in the stable ($\omega_i < 0$) or unstable ($\omega_i > 0$) regions of the parameter space; for the Wi chosen in figure 31, the bifurcation occurs prior to the instability. For the scaled equations obtained in the narrow-gap limit ($\epsilon \to 0$, $\epsilon^{1/2} Wi \sim O(1)$), the most unstable mode appears to always remain stationary. Figure 32

https://doi.org/10.1017/jfm.2026.12002 Published online by Cambridge University Press

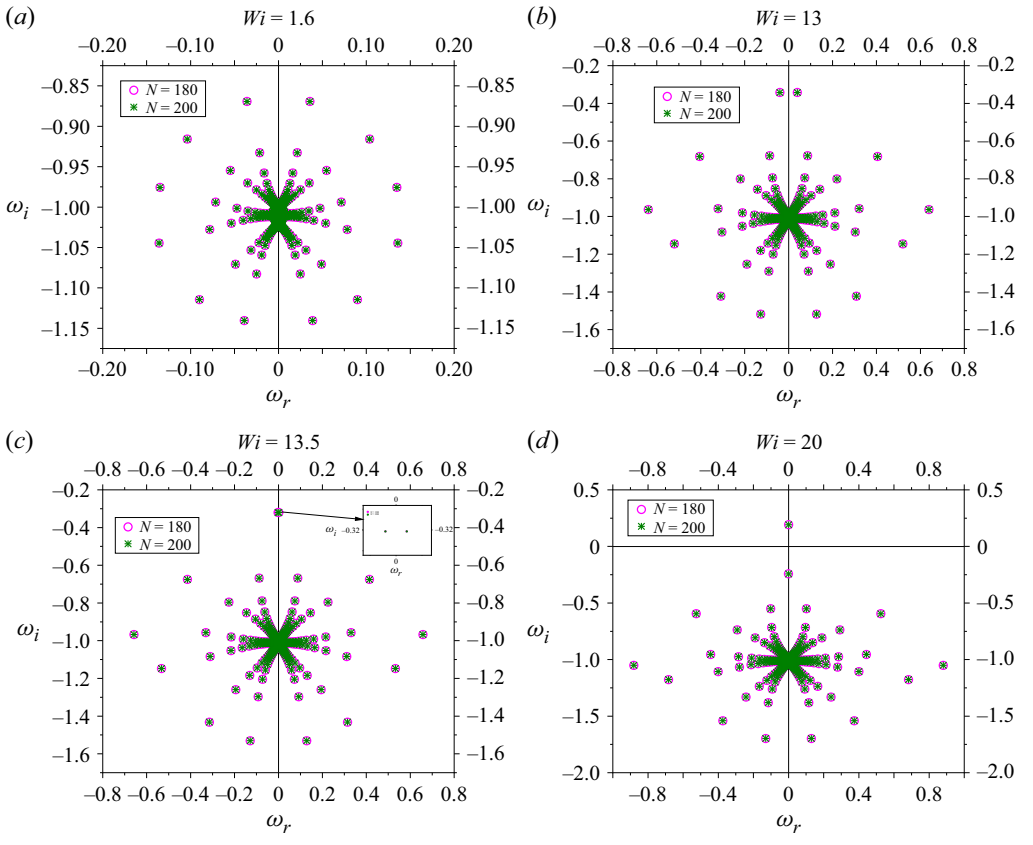


Figure 32. Axisymmetric ($n = 0$) eigenspectra for $\epsilon = 0.1$, $\alpha = 7$, $\beta = 0.98$ at different Wi for Dean flow of an Oldroyd-B: (*a*) $Wi = 1.6$; (*b*) $Wi = 13$; (*c*) $Wi = 13.5$ and (*d*) $Wi = 20$.

depicts the structure of the spectrum for varying Wi and for α fixed at 7. In this case, the spectrum evolves in the opposite direction (relative to figure 31) as Wi is increased from 1.6 to 13; in that, we start off with the pair of least stable modes being propagating ones, which move towards each other with increasing Wi, coalescing at $Wi \approx 13.52$. As Wi is increased further, two stationary modes bifurcate out of the coalescence point, with one of the modes becoming unstable, while the other becomes more stable, *viz*., they travel in the opposite directions along the $\omega_r = 0$ axis. Although not shown here, we have verified that for $\epsilon = 0.1$ and $\beta = 0.98$, the least stable modes are stationary at all Wi for $\alpha < \alpha_{critical} \approx 4$. In contrast, for $\alpha > \alpha_{critical} = 4$, the least stable modes are propagating at lower Wi (e.g. $Wi = 1.6$), but eventually become stationary at higher Wi.

The effect of increasing Wi/L on the spectra is shown in figure 33; this may be achieved by increasing Wi for a fixed L (as in the figure) or by decreasing L for a fixed Wi. Here, the two symmetrically placed wing-like structures as well as the vertical line-like segments on the imaginary axis (as discussed in § 3) are numerical approximations of the CS in Dean flow (Mohanty *et al.* 2026). The spectrum approaches a purely continuous one as Wi is increased from figure 33(*a–f*), with the wings in particular assuming their full form for the largest Wi/L.

Figures 34(*a*) and 34(*c*) depict the spectra for the same Wi/L, albeit at different choices of Wi and L; figures 34(*b*) and 34(*d*) show their corresponding magnified views. A data collapse of the base-state velocity profiles was demonstrated for different pairs of (Wi, L)

https://doi.org/10.1017/jfm.2026.12002 Published online by Cambridge University Press

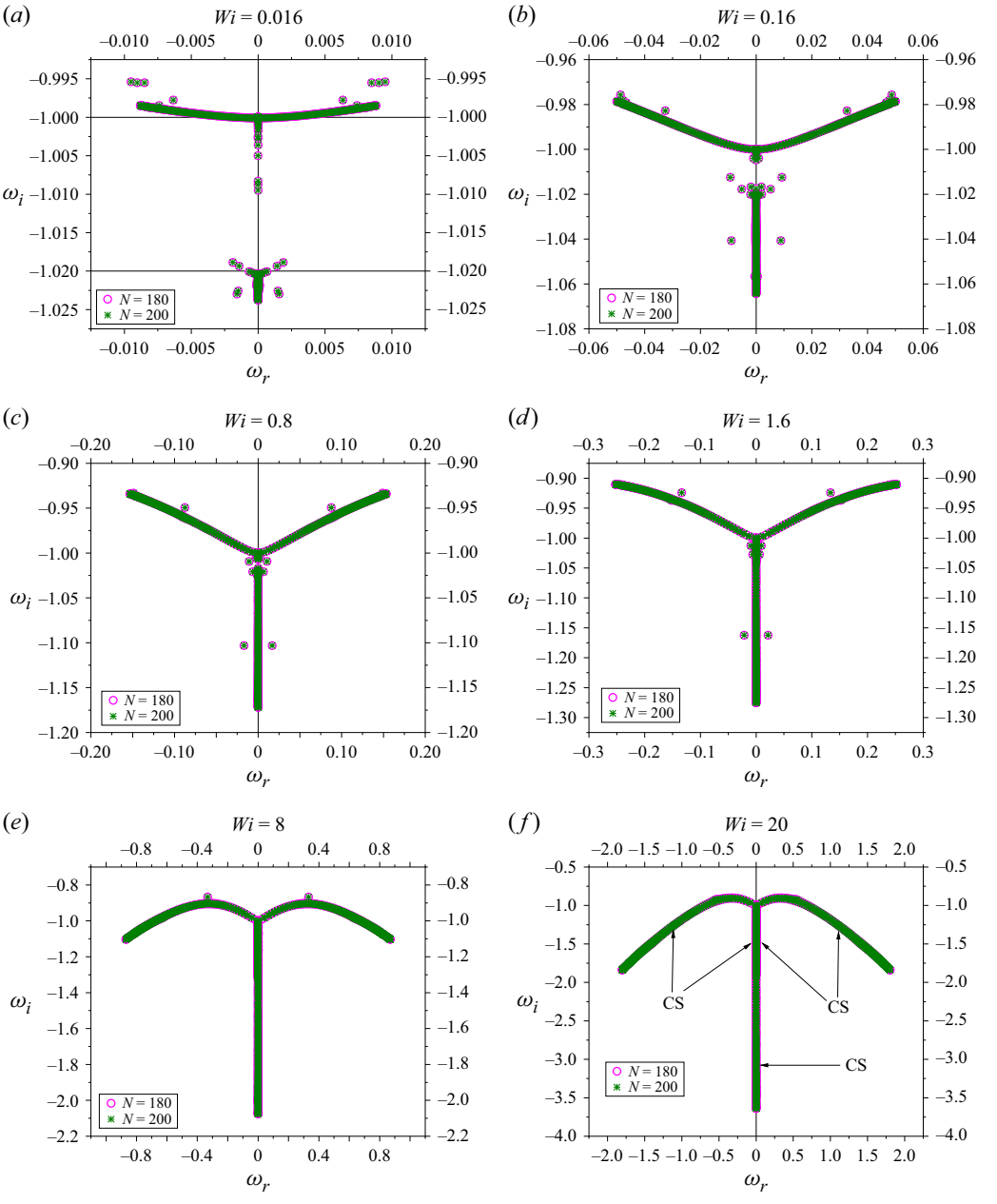


Figure 33. Axisymmetric ($n = 0$) eigenspectra at different Wi for Dean flow. Data for $\epsilon = 0.1$, $\alpha = 7$, $\beta = 0.98$, $L = 100$: (*a*) $Wi = 0.016$; (*b*) $Wi = 0.16$; (*c*) $Wi = 0.8$; (*d*) $Wi = 1.6$; (*e*) $Wi = 8$ and (*f*) $Wi = 20$.

for a fixed Wi/L ratio for Dean flow for fixed ϵ and β (see figure 2). However, figure 34 shows that the eigenspectrum is independently influenced by Wi and L, and not just by the Wi/L alone. This can be attributed to the two- or three-dimensional nature of the disturbance flow field; the original data collapse of Yamani & McKinley (2023) and Tej *et al.* (2024) is expected to hold only for viscometric flows.

https://doi.org/10.1017/jfm.2026.12002 Published online by Cambridge University Press

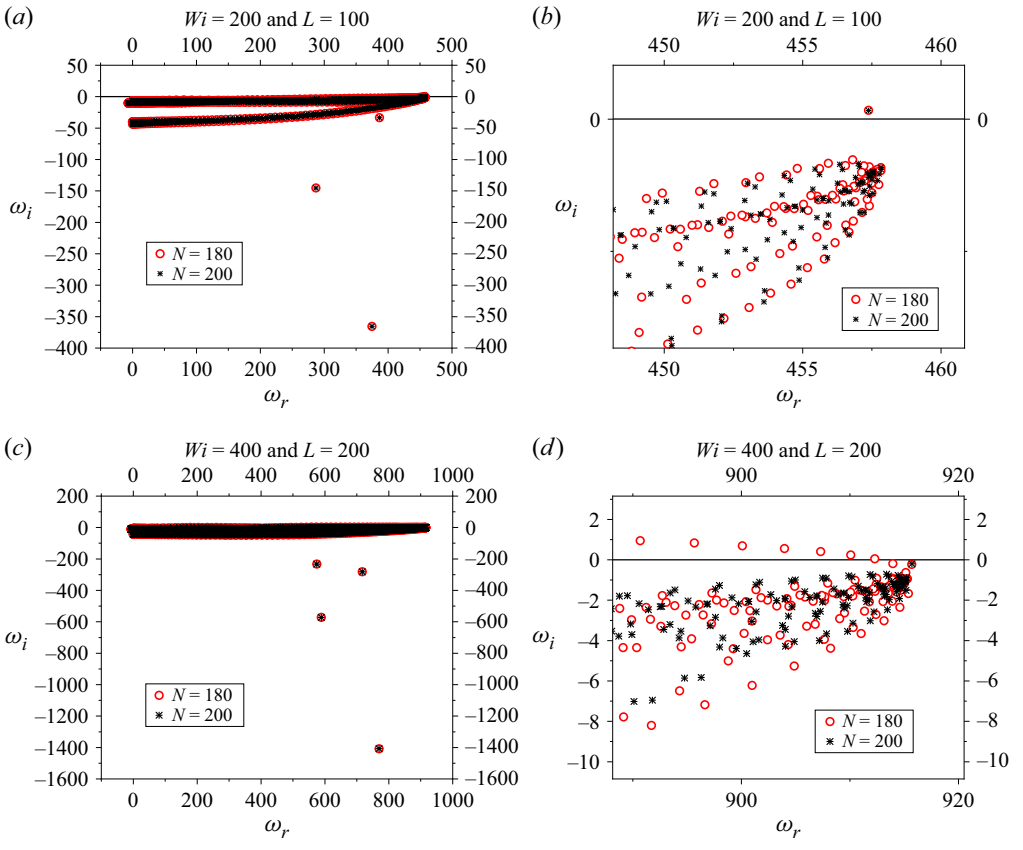


Figure 34. Eigenspectra demonstrating the centre mode in Dean flow of a FENE-P fluid at $Re = 0$, $\alpha = 0.1$, $\beta = 0.98$, $\epsilon = 0.1$ and $n = 16$ for $Wi/L = 2$, but for two $(Wi,\ L)$ pairs. (*a*) Full eigenspectrum for the given parameters and (*b*) zoomed-in view of panel (*a*). (*c*) Full eigenspectrum for another set of Wi and L, and (*d*) zoomed-in view of panel (*c*). The eigenspectra obtained for $N = 180$ and 200 show good convergence. (*a*) $Wi = 200$ and $L = 100$; (*b*) $Wi = 200$ and $L = 100$; (*c*) $Wi = 400$ and $L = 200$; and (*d*)$Wi = 400$ and $L = 200$.

Appendix D. Eigenfunctions for viscoelastic Dean flow

In this appendix, we present the eigenfunctions for the centre mode (CM) and hoop-stress modes (HSM1 and HSM2). As discussed earlier, for the eigenspectrum in figure 16, the CM instability observed in our work for Dean flow is analogous to the instability reported by Khalid *et al.* (2025) for channel flow. The eigenfunctions for the CM (figure 35) show strong peaks in $\tilde{\tau}_{\theta\theta}$ and $\tilde{\tau}_{zz}$ near the location of the base-state maximum, a signature that is prominent even in rectilinear channel flow. The eigenfunctions of HSM1 and HSM2, presented in figures 36 and 37, in contrast, are qualitatively different from those for CM. In fact, the eigenfunctions for HSM2 are qualitatively similar to those for HSM1, with HSM2 (HSM1) being localised near the inner (outer) boundaries, thereby also reinforcing that HSM2 is not a continuation of CM.

https://doi.org/10.1017/jfm.2026.12002 Published online by Cambridge University Press

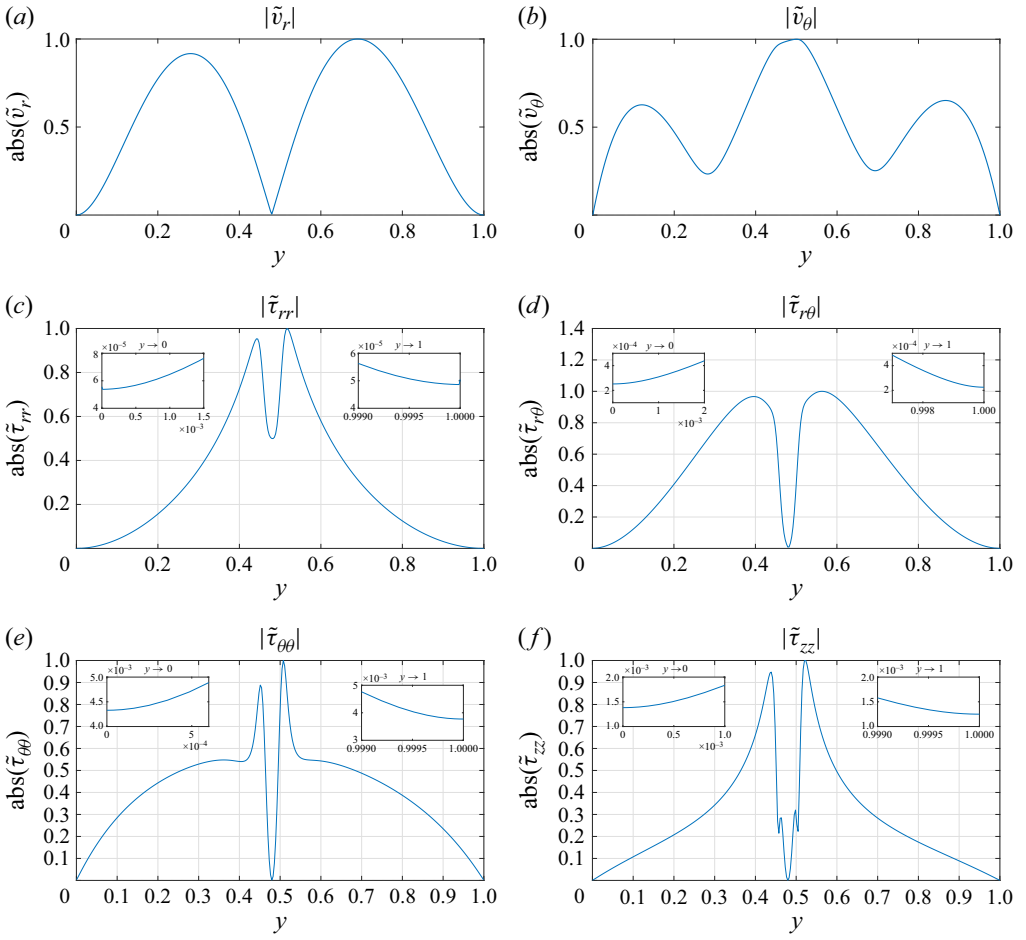


Figure 35. Amplitude of the centre-mode eigenfunctions in the r–θ plane for Dean flow of a FENE-P fluid; $\epsilon = 0.1$, $\beta = 0.98$, $L = 100$, $Wi = 60$, $n = 40$, $\alpha = 0$. All eigenfunctions are normalised by their respective maximum values. Both perturbation components vanish at the walls due to no-slip, no-penetration, while the stress perturbations (which are not subject to boundary conditions) take small but non-zero values.

https://doi.org/10.1017/jfm.2026.12002 Published online by Cambridge University Press

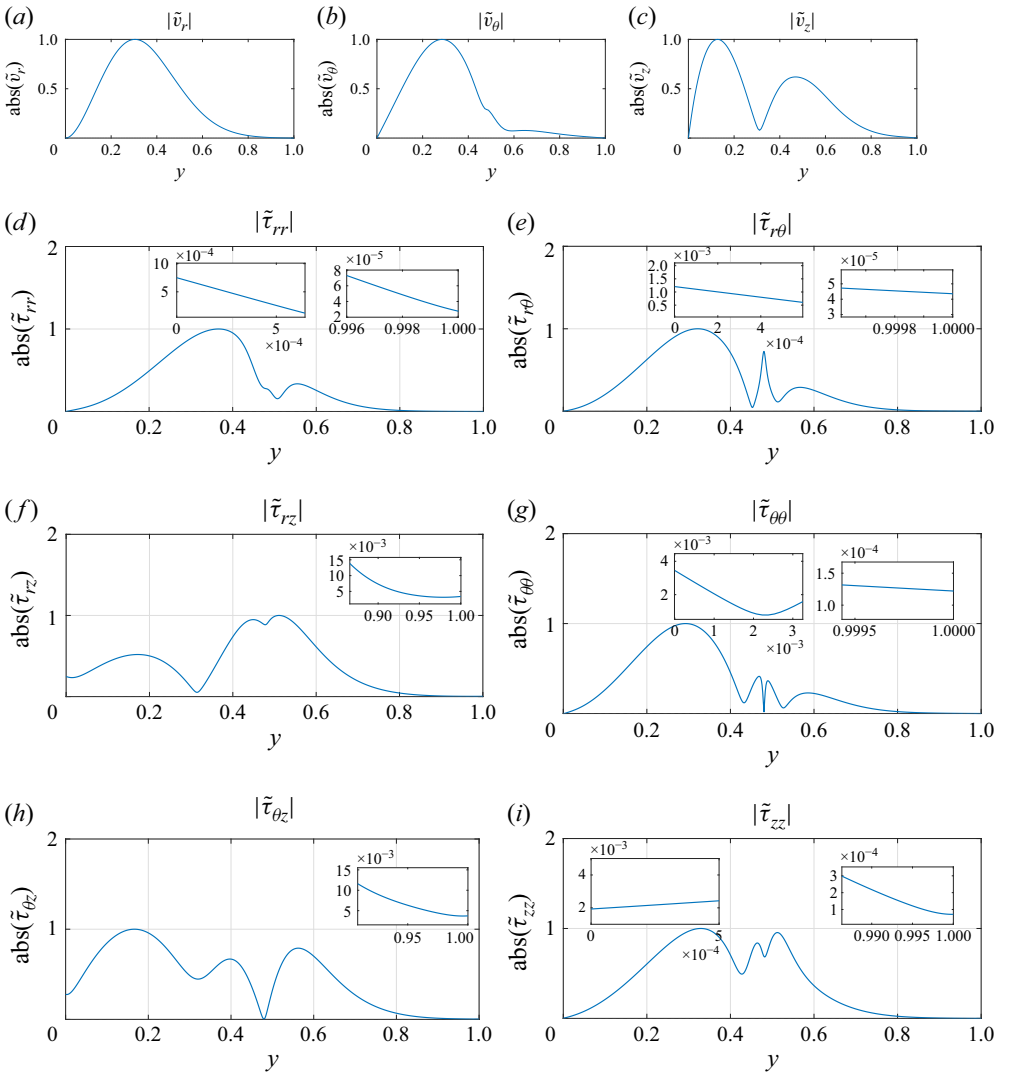


Figure 36. Amplitude of the hoop-stress-mode (HSM2) eigenfunctions in the r–θ plane for Dean flow of a FENE-P fluid; $\epsilon = 0.1$, $\beta = 0.98$, $L = 100$, $Wi = 400$, $n = 1$, $\alpha = 7$. All eigenfunctions are normalised by their respective maximum values. Unlike the centre mode, the HSM1 eigenfunction is concentrated near the inner wall where the base-state hoop stress $\bar{\tau}_{\theta\theta}$ is largest.

https://doi.org/10.1017/jfm.2026.12002 Published online by Cambridge University Press

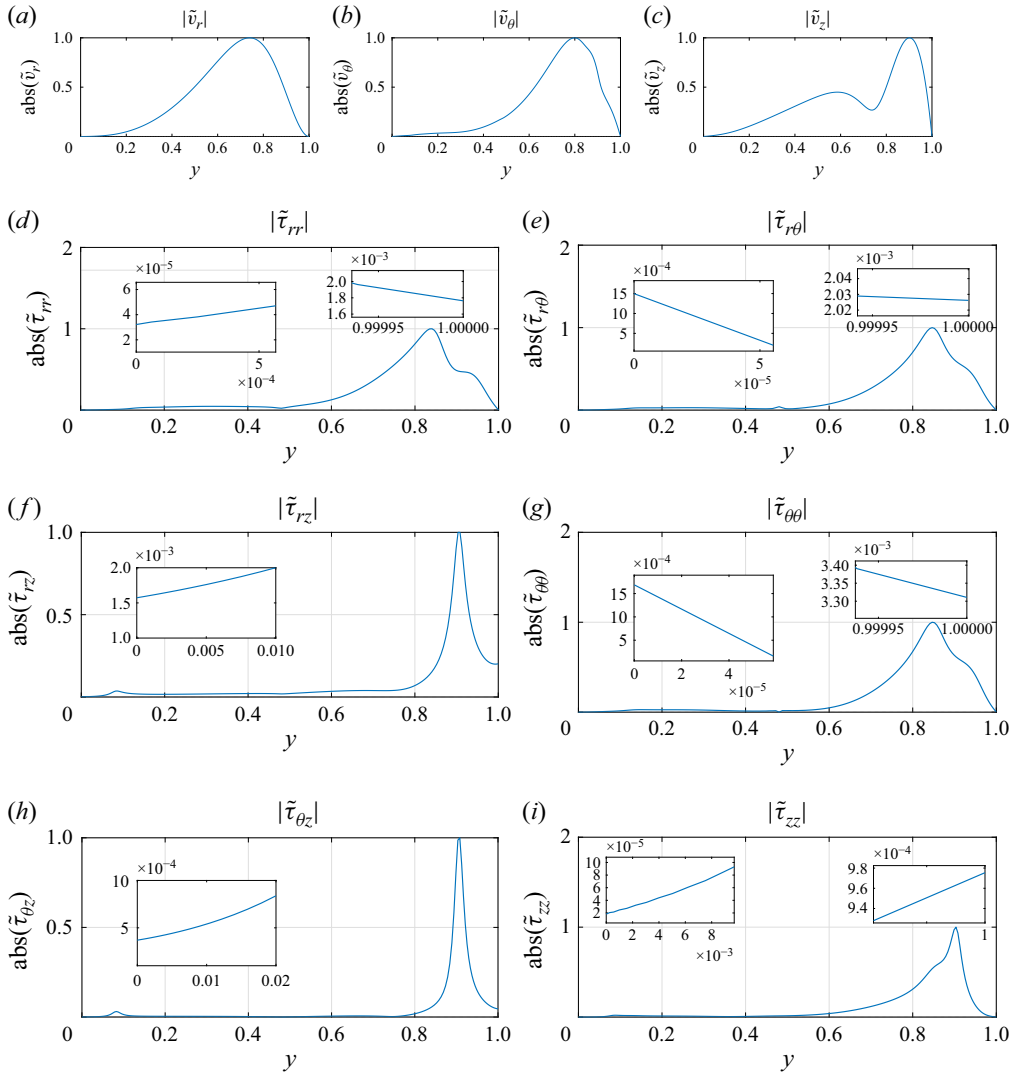


Figure 37. Amplitude of the hoop-stress-mode (HSM1) eigenfunctions in the r–θ plane for Dean flow of a FENE-P fluid; $\epsilon = 0.1$, $\beta = 0.98$, $L = 100$, $Wi = 400$, $n = 1$, $\alpha = 7$. All eigenfunctions are normalised by their respective maximum values. Unlike the centre mode, the HSM1 eigenfunction is concentrated near the inner wall where the base-state hoop stress $\bar{\tau}_{\theta\theta}$ is largest.

References

Avgousti, M. & Beris, A.N. 1993 Nonaxisymmetric modes in viscoelastic Taylor–Couette flow. *J. Non-Newtonian Fluid Mech.* **50** (2), 225–251.

Bai, J.-J., Zhang, X., Wei, X., Wang, Y., Du, C., Wang, Z.-J., Chen, M.-L. & Wang, J.-H. 2023 Dean-flow-coupled elasto-inertial focusing accelerates exosome purification to facilitate single vesicle profiling. *Anal. Chem.* **95** (4), 2523–2531.

Beneitez, M., Mrini, S. & Kerswell, R.R. 2025 Linear instability in planar viscoelastic Taylor–Couette flow with and without explicit polymer diffusion. *J. Non-Newtonian Fluid Mech.* **345**, 105459.

Beneitez, M., Page, J. & Kerswell, R.R. 2023 Polymer diffusive instability leading to elastic turbulence in plane Couette flow. *Phys. Rev. Fluids* **8**, L101901.

Benjamin, T.B. 1978 Bifurcation phenomena in steady flows of a viscous fluid. I. Theory. *Proc. R. Soc. Lond. A Math. Phys. Sci.* **359** (1696), 1–26.

https://doi.org/10.1017/jfm.2026.12002 Published online by Cambridge University Press

BERGER, S.A., TALBOT, L. & YAO, L.S. 1983 Flow in curved pipes. *Annu. Rev. Fluid Mech.* **15** (1983), 461–512.

BERTOLA, V., MEULENBROEK, B., WAGNER, C., STORM, C., MOROZOV, A., VAN SAARLOOS, W. & BONN, D. 2003 Experimental evidence for an intrinsic route to polymer melt fracture phenomena: a nonlinear instability of viscoelastic Poiseuille flow. *Phys. Rev. Lett.* **90**, 114502.

BIRD, R.B., DOTSON, P.J. & JOHNSON, N.L. 1980 Polymer solution rheology based on a finitely extensible bead—spring chain model. *J. Non-Newtonian Fluid Mech.* **7**, 213–235.

BISTAGNINO, A., BOFFETTA, G., CELANI, A., MAZZINO, A., PULIAFITO, A. & VERGASSOLA, M. 2007 Nonlinear dynamics of the viscoelastic Kolmogorov flow. *J. Fluid Mech.* **590**, 61–80.

BOFFETTA, G., CELANI, A., MAZZINO, A., PULIAFITO, A. & VERGASSOLA, M. 2005 The viscoelastic Kolmogorov flow: eddy viscosity and linear stability. *J. Fluid Mech.* **523**, 161–170.

BOWEN, P.J., DAVIES, A.R. & WALTERS, K. 1991 On viscoelastic effects in swirling flows. *J. Non-Newtonian Fluid Mech.* **38** (2), 113–126.

BUZA, G., BENEITEZ, M., PAGE, J. & KERSWELL, R.R. 2022*a* Finite-amplitude elastic waves in viscoelastic channel flow from large to zero Reynolds number. *J. Fluid Mech.* **951**, A3.

BUZA, G., PAGE, J. & KERSWELL, R.R. 2022*b* Weakly nonlinear analysis of the viscoelastic instability in channel flow for finite and vanishing Reynolds numbers. *J. Fluid Mech.* **940**, A11.

BYARS, J.A., OZTEKIN, A., BROWN, R.A. & MCKINLEY, G.H. 1994 Spiral instabilities in the flow of highly elastic fluids between rotating parallel disc. *J. Fluid Mech.* **271**, 173–218.

CASTILLO SÁNCHEZ, H.A., JOVANOVIĆ, M.R., KUMAR, S., MOROZOV, A., SHANKAR, V., SUBRAMANIAN, G. & WILSON, H.J. 2022 Understanding viscoelastic flow instabilities: Oldroyd-B and beyond. *J. Non-Newtonian Fluid Mech.* **302**, 104742.

CHANDRA, B., SHANKAR, V. & DAS, D. 2018 Onset of transition in the flow of polymer solutions through microtubes. *J. Fluid Mech.* **844**, 1052–1083.

CHAUDHARY, I., GARG, P., SUBRAMANIAN, G. & SHANKAR, V. 2021 Linear instability of viscoelastic pipe flow. *J. Fluid Mech.* **908**, A11.

CHEN, D., HUANG, Q., NI, Z. & XIANG, N. 2024 Elasto-inertial particle focusing in sinusoidal microfluidic channels. *Electrophoresis* **45**, 2191–2201.

CHOUEIRI, G.H., LOPEZ, J.M., VARSHNEY, A., SANKAR, S. & HOF, B. 2021 Experimental observation of the origin and structure of elastoinertial turbulence. *Proc. Natl Acad. Sci. USA* **118** (45), e2102350118.

COUCHMAN, M.M.P., BENEITEZ, M., PAGE, J. & KERSWELL, R.R. 2024 Inertial enhancement of the polymer diffusive instability. *J. Fluid Mech.* **981**, A2.

DATTA, S.S. *et al.* 2022 Perspectives on viscoelastic flow instabilities and elastic turbulence. *Phys. Rev. Fluids* **7**, 080701.

DEAN, W.R. & CHAPMAN, S. 1928 Fluid motion in a curved channel. *Proc. R. Soc. Lond. A* **121** (787), 402–420.

DIPRIMA, R.C. 1959 The stability of viscous flow between rotating concentric cylinders with a pressure gradient acting round the cylinders. *J. Fluid Mech.* **6** (3), 462–468.

DUTCHER, C.S. & MULLER, S.J. 2013 Effects of moderate elasticity on the stability of co- and counter-rotating Taylor–Couette flows. *J. Rheol.* **57** (3), 791–812.

FAN, Y., TANNER, R.I. & PHAN-THIEN, N. 2001 Fully developed viscous and viscoelastic flows in curved pipes. *J. Fluid Mech.* **440**, 327–357.

GROISMAN, A. & STEINBERG, V. 2001 Efficient mixing at low Reynolds numbers using polymer additives. *Nature* **410**, 905–908.

GROISMAN, A. & STEINBERG, V. 2004 Elastic turbulence in curvilinear flows of polymer solutions. *New J. Phys.* **6**, 29.

HAWARD, S.J., MCKINLEY, G.H. & SHEN, A.Q. 2016 Elastic instabilities in planar elongational flow of monodisperse polymer solutions. *Sci. Rep. UK* **6**, 33029.

HERRCHEN, M. & OTTINGER, H.C. 1997 A detailed comparison of various FENE dumbbell models. *J. Non-Newtonian Fluid Mech.* **68** (1), 17–42.

HO, T.C. & DENN, M.M. 1977 Stability of plane Poiseuille flow of a highly elastic liquid. *J. Non-Newtonian Fluid Mech.* **3** (2), 179–195.

JOO, Y.L. & SHAQFEH, E.S.G. 1991 Viscoelastic Poiseuille flow through a curved channel: a new elastic instability. *Phys. Fluids A: Fluid Dyn.* **3** (9), 2043–2046.

JOO, Y.L. & SHAQFEH, E.S.G. 1992 A purely elastic instability in Dean and Taylor–Dean flow. *Phys. Fluids A: Fluid Dyn.* **4** (3), 524–543.

JOO, Y.L. & SHAQFEH, E.S.G. 1994 Observations of purely elastic instabilities in the Taylor–Dean flow of a Boger fluid. *J. Fluid Mech.* **262**, 27–73.

https://doi.org/10.1017/jfm.2026.12002 Published online by Cambridge University Press

KERSWELL, R.R. & PAGE, J. 2024 Asymptotics of the centre-mode instability in viscoelastic channel flow: with and without inertia. *J. Fluid Mech.* **991**, A13.
KHALID, M., BADONI, A., DUTTA, D., NAIDU, P., SUBRAMANIAN, G. & SHANKAR, V. 2025 Role of finite extensibility on the centre-mode instability in viscoelastic channel flow. *J. Fluid Mech.* **1009**, A28.
KHALID, M., CHAUDHARY, I., GARG, P., SHANKAR, V. & SUBRAMANIAN, G. 2021*a* The centre-mode instability of viscoelastic plane Poiseuille flow. *J. Fluid Mech.* **915**, A43.
KHALID, M., SHANKAR, V. & SUBRAMANIAN, G. 2021*b* Continuous pathway between the elasto-inertial and elastic turbulent states in viscoelastic channel flow. *Phys. Rev. Lett.* **127**, 134502.
LACASSAGNE, T., CAGNEY, N. & BALABANI, S. 2021 Shear-thinning mediation of elasto-inertial Taylor–Couette flow. *J. Fluid Mech.* **915**, A91.
LARSON, R.G. 1988 *Constitutive Equations for Polymer Melts and Solutions*. Butterworths.
LARSON, R.G., SHAQFEH, E.S.G. & MULLER, S.J. 1990 A purely elastic instability in Taylor–Couette flow. *J. Fluid Mech.* **218**, 573–600.
LEWY, T. & KERSWELL, R. 2024 The polymer diffusive instability in highly concentrated polymeric fluids. *J. Non-Newtonian Fluid Mech.* **326**, 105212.
LEWY, T. & KERSWELL, R.R. 2025 Revisiting two-dimensional viscoelastic Kolmogorov flow: a centre-mode-driven transition. *J. Fluid Mech.* **1007**, A55.
LIKHTMAN, A.E. & GRAHAM, R.S. 2003 Simple constitutive equation for linear polymer melts derived from molecular theory: Rolie–Poly equation. *J. Non-Newtonian Fluid Mech.* **114**, 1–12.
LU, Z. & HOF, B. 2026 Multiple states of turbulence at vanishing inertia. arXiv: 2602.23498.
MCKINLEY, G.H., BYARS, J.A., BROWN, R.A. & ARMSTRONG, R.C. 1991 Observations on the elastic instability in cone-and-plate and parallel-plate flows of a polyisobutylene Boger fluid. *J. Non-Newtonian Fluid Mech.* **40** (2), 201–229.
MCKINLEY, G.H., OZTEKIN, A., BYARS, J.A. & BROWN, R.A. 1995 Self-similar spiral instabilities in elastic flows between a cone and a plate. *J. Fluid Mech.* **285**, 123–164.
MCKINLEY, G.H., PAKDEL, P. & OZTEKIN, A. 1996 Rheological and geometric scaling of purely elastic flow instabilities. *J. Non-Newtonian Fluid Mech.* **67**, 19–47.
MEULENBROEK, B., STORM, C., BERTOLA, V., WAGNER, C., BONN, D. & VAN SAARLOOS, W. 2003 Intrinsic route to melt fracture in polymer extrusion: a weakly nonlinear subcritical instability of viscoelastic Poiseuille flow. *Phys. Rev. Lett.* **90**, 024502.
MOHANTY, P.K., TEJ, P.S.D.S.P., SUBRAMANIAN, G. & SHANKAR, V. 2026 Nature of continuous spectra in wall-bounded shearing flows of FENE-P fluids. *Phys. Rev. Fluids* **11**, 053304.
MORE, R.V., PATTERSON, R., PASHKOVSKI, E. & MCKINLEY, G.H. 2024 Elasto-inertial instability in torsional flows of shear-thinning viscoelastic fluids. *J. Fluid Mech.* **985**, A37.
MOROZOV, A.N. & VAN SAARLOOS, W. 2005*a* Subcritical finite-amplitude solutions for plane Couette flow of viscoelastic fluids. *Phys. Rev. Lett.* **95**, 024501.
MOROZOV, A.N. & VAN SAARLOOS, W. 2005*b* Subcritical instabilities in plane Couette flow of visco-elastic fluids. In *IUTAM Symposium on Laminar-Turbulent Transition and Finite Amplitude Solutions* (ed. T. Mullin & R. Kerswell), Fluid Mechanics and its Applications, vol. 77, pp. 313–330. Springer Netherlands.
MOROZOV, A.N. & VAN SAARLOOS, W. 2007 An introductory essay on subcritical instabilities and the transition to turbulence in visco-elastic parallel shear flows. *Phys. Rep.* **447** (3), 112–143.
MOROZOV, A.N. & VAN SAARLOOS, W. 2019 Subcritical instabilities in plane Poiseuille flow of an Oldroyd-B fluid. *J. Stat. Phys.* **175**, 554–577.
NAGATA, M. 1990 Three-dimensional finite-amplitude solutions in plane Couette flow: bifurcation from infinity. *J. Fluid Mech.* **217**, 519–527.
NEELAMEGAM, R., SHANKAR, V. & DAS, D. 2013 Suppression of purely elastic instabilities in the torsional flow of viscoelastic fluid past a soft solid. *Phys. Fluids* **25** (12), 124102.
NIKDOOST, A. & REZAI, P. 2020 Dean flow velocity of viscoelastic fluids in curved microchannels. *AIP Adv.* **10** (8), 085015.
OZTEKIN, A., BROWN, R.A. & MCKINLEY, G.H. 1994 Quantitative prediction of the viscoelastic instability in cone-and-plate flow of a Boger fluid using a multi-mode Giesekus model. *J. Non-Newtonian Fluid Mech.* **54**, 351–377.
PAGE, J., DUBIEF, Y. & KERSWELL, R.R. 2020 Exact travelling wave solutions in viscoelastic channel flow. *Phys. Rev. Lett.* **125**, 154501.
PAKDEL, P. & MCKINLEY, G.H. 1996 Elastic instability and curved streamlines. *Phys. Rev. Lett.* **77**, 2459–2462.
PAN, L., MOROZOV, A., WAGNER, C. & ARRATIA, P.E. 2013 Nonlinear elastic instability in channel flows at low Reynolds numbers. *Phys. Rev. Lett.* **110**, 174502.

https://doi.org/10.1017/jfm.2026.12002 Published online by Cambridge University Press

PANDEY, S. & SHANKAR, V. 2025 Effect of anisotropic mobility on the diffusive instability in viscoelastic shear flows. *Phys. Rev. Fluids* **10**, 053301.
POOLE, R.J., LINDNER, A. & ALVES, M.A. 2013 Viscoelastic secondary flows in serpentine channels. *J. Non-Newtonian Fluid Mech.* **201**, 10–16.
PRIYADARSHI, M., SRITA, K.V., BHASKAR, V.V.K.N.S., KHALID, M., SUBRAMANIAN, G. & SHANKAR, V. 2023 A new elastic instability in gravity-driven viscoelastic film flow. *Phys. Fluids* **35**, 073104.
RAMANAN, V.V., KUMAR, K.A. & GRAHAM, M.D. 1999 Stability of viscoelastic shear flows subjected to steady or oscillatory transverse flow. *J. Fluid Mech.* **379**, 255–277.
ROTHSTEIN, J.P. & MCKINLEY, G.H. 2001 The axisymmetric contraction–expansion: the role of extensional rheology on vortex growth dynamics and the enhanced pressure drop. *J. Non-Newtonian Fluid Mech.* **98** (1), 33–63.
ROY, A., GARG, P., REDDY, J.S. & SUBRAMANIAN, G. 2022 Inertio–elastic instability of a vortex column. *J. Fluid Mech.* **937**, A27.
RUBINSTEIN, M. & COLBY, R.H. 2014 *Polymer Physics*. Oxford University Press.
SAMANTA, D., DUBIEF, Y., HOLZNER, M., SCHÄFER, C., MOROZOV, A.N., WAGNER, C. & HOF, B. 2013 Elasto-inertial turbulence. *Proc. Natl Acad. Sci. USA* **110** (26), 10557–10562.
SCHAEFER, C., MOROZOV, A. & WAGNER, C. 2018 Geometric scaling of elastic instabilities in the Taylor–Couette geometry: a theoretical, experimental and numerical study. *J. Non-Newtonian Fluid Mech.* **259**, 78–90.
SCHMID, P.J. & HENNINGSON, D.S. 2001 *Stability and Transition in Shear Flows, Applied Mathematical Sciences*, vol. 142. Springer.
SHAKERI, P., JUNG, M. & SEEMANN, R. 2021 Effect of elastic instability on mobilization of capillary entrapments. *Phys. Fluids* **33** (11), 113102.
SHAQFEH, E.S.G. & KHOMAMI, B. 2021 The Oldroyd-B fluid in elastic instabilities, turbulence and particle suspensions. *J. Non-Newtonian Fluid Mech.* **298**, 104672.
SHAQFEH, E.S.G. 1996 Purely elastic instabilities in viscometric flows. *Annu. Rev. Fluid Mech.* **28**, 129–185.
SHEKAR, A., MCMULLEN, R.M., MCKEON, B.J. & GRAHAM, M.D. 2020 Self-sustained elastoinertial Tollmien–Schlichting waves. *J. Fluid Mech.* **897**, A3.
SHEKAR, A., MCMULLEN, R.M., MCKEON, B.J. & GRAHAM, M.D. 2021 Tollmien–Schlichting route to elastoinertial turbulence in channel flow. *Phys. Rev. Fluids* **6**, 093301.
SHEKAR, A., MCMULLEN, R.M., WANG, S., MCKEON, B.J. & GRAHAM, M.D. 2019 Critical-layer structures and mechanisms in elastoinertial turbulence. *Phys. Rev. Lett.* **122**, 124503.
STEINBERG, V. 2021 Elastic turbulence: an experimental view on inertialess random flow. *Annu. Rev. Fluid Mech.* **53** (1), 27–58.
TEJ, P.S.D.S.P., MOHANTY, P.K. & SHANKAR, V. 2024 Master curves for unidirectional flows of FENE-P fluids in rectilinear and curvilinear geometries. *J. Non-Newtonian Fluid Mech.* **334**, 105332.
TREFETHEN, L.N. 2000 *Spectral Methods in MATLAB*. SIAM.
VARSHNEY, A. & STEINBERG, V. 2018 Drag enhancement and drag reduction in viscoelastic flow. *Phys. Rev. Fluids* **3**, 103302.
WEIDEMAN, J.A. & REDDY, S.C. 2000 A MATLAB differentiation matrix suite. *ACM Trans. Math. Softw.* **26**, 465–519.
WHITE, J.M. & MULLER, S.J. 2000 Viscous heating and the stability of Newtonian and viscoelastic Taylor–Couette flows. *Phys. Rev. Lett.* **84**, 5130–5133.
WILSON, H.J., RENARDY, M. & RENARDY, Y.Y. 1999 Structure of the spectrum in zero Reynolds number shear flow of the UCM and Oldroyd-B liquids. *J. Non-Newtonian Fluid Mech.* **80** (2–3), 251–268.
YADAV, S.K., SUBRAMANIAN, G. & SHANKAR, V. 2024 Elastic instability in a family of rectilinear viscoelastic channel flows devoid of centerline symmetry. *Phys. Rev. Fluids* **9**, 013301.
YAMANI, S. & MCKINLEY, G.H. 2023 Master curves for FENE-P fluids in steady shear flow. *J. Non-Newtonian Fluid Mech.* **313**, 104944.
ZHANG, Y.-B., LI, L., FAN, Y., SU, J., XI, H.-D. & SUN, C. 2025 Experimental evidence for the continuous transition between elastic and elastoinertial turbulence. *Proc. Natl Acad. Sci. USA* **122** (38), e2505007122.

https://doi.org/10.1017/jfm.2026.12002 Published online by Cambridge University Press